

Electronic Theses and Dissertations, 2004-2019

2012

Optical Fluid-based Photonic And Display Devices

Su Xu

University of Central Florida

 Part of the [Electromagnetics and Photonics Commons](#), and the [Optics Commons](#)
Find similar works at: <https://stars.library.ucf.edu/etd>
University of Central Florida Libraries <http://library.ucf.edu>

This Doctoral Dissertation (Open Access) is brought to you for free and open access by STARS. It has been accepted for inclusion in Electronic Theses and Dissertations, 2004-2019 by an authorized administrator of STARS. For more information, please contact STARS@ucf.edu.

STARS Citation

Xu, Su, "Optical Fluid-based Photonic And Display Devices" (2012). *Electronic Theses and Dissertations, 2004-2019*. 2434.

<https://stars.library.ucf.edu/etd/2434>

OPTICAL FLUID-BASED PHOTONIC AND DISPLAY DEVICES

by

SU XU

B.S. Zhejiang University, China, 2004

M.S. Zhejiang University, China, 2006

A dissertation submitted in partial fulfillment of the requirements
for the degree of Doctor of Philosophy
in CREOL, The College of Optics & Photonics
at the University of Central Florida
Orlando, Florida

Fall Term
2012

Major Professor: Shin-Tson Wu

© 2012 Su Xu

ABSTRACT

Conventional solid-state photonic devices exhibit an ultra-high optical performance and durability, but minimal adaptability. Recently, optical fluid-based photonic and display devices are emerging. By dynamically manipulating the optical interface formed by liquids, the optical output can be reconfigured or adaptively tuned in real time. Such devices exhibit some unique characteristics that are not achievable in conventional solid-state photonic devices. Therefore, they open a gateway for new applications, such as image and signal processing, optical communication, sensing, and lab-on-a-chip, etc. Different operation principles of optical fluid-based photonic devices have been proposed, for instance fluidic pressure, electrochemistry, thermal effect, environmentally adaptive hydrogel, electro-wetting and dielectrophoresis.

In this dissertation, several novel optical fluid-based photonic and display devices are demonstrated. Their working principles are described and electro-optic properties investigated.

The first part involves photonic devices based on fluidic pressure. Here, we present a membrane-encapsulated liquid lens actuated by a photo-activated polymer. This approach paves a way to achieve non-mechanical driving and easy integration with other photonic devices. Next, we develop a mechanical-wetting lens for visible and short-wavelength infrared applications. Such a device concept can be extended to longer wavelength if proper liquids are employed.

In the second part, we reveal some new photonic and display devices based on dielectrophoretic effects. We conceive a dielectric liquid microlens with well-shaped electrode for fixing the droplet position and lowering the operating voltage. To widen the dynamic range, we demonstrate an approach to enable focus tuning from negative to positive or vice versa in a single dielectric lens without any moving part. The possibility of fabricating microlens arrays

with different aperture and density using a simple method is also proposed. Furthermore, the fundamental electro-optic characteristics of dielectric liquid droplets are studied from the aspects of operating voltage, frequency and droplet size. In addition to dielectric liquid lenses, we also demonstrate some new optical switches based on dielectrophoretic effect, e.g., optical switch based on voltage-stretchable liquid crystal droplet, variable aperture or position-shifting droplet. These devices work well in the visible and near infrared spectral ranges. We also extend this approach to display and show a polarizer-free and color filter-free display. Simple fabrication, low power consumption, polarization independence, relatively low operating voltage as well as reasonably fast switching time are their key features.

Dedication.

ACKNOWLEDGMENTS

I would like to express my sincere appreciation to those who have made contributions to this work and who have offered supports during my Ph. D study at University of Central Florida.

First of all, I would like to thank my advisor Prof. Shin-Tson Wu for his great supervision, encouragement and support during my Ph. D study. To me, Prof. Wu is more than a good advisor. He enriches my mind, broadens my view and kindles the light for my life.

I am also grateful to all of my committee members Prof. Glenn D. Boreman, Prof. James E. Harvey, Prof. Guifang Li, Prof. M. G. Moharam and Prof. Thomas X. Wu for their great support and valuable comments throughout this work.

And I especially want to thank Prof. Hongwen Ren from Chonbuk National University (Republic of South Korea), for his intelligent discussion, guidance and hands-on training in my experimental work.

In addition, I would also like to thank all my colleagues in the Photonics and Display Group at CREOL, for their valuable discussions, inspirations and priceless help. I treasure the opportunity of working in such a friendly and productive group, and gaining life experience besides the academic achievement.

Moreover, I would like to thank the financial support from Air Force Office of Scientific Research (AFOSR), Areté Associates and Industrial Technology Research Institute (ITRI) (Taiwan).

Finally, this work is dedicated to my dear parents and friends, for their love and encouragement throughout my life.

TABLE OF CONTENTS

LIST OF FIGURES	ix
LIST OF TABLES	xvi
LIST OF NOMENCLATURE.....	xvii
CHAPTER 1 INTRODUCTION TO OPTICAL FLUID-BASED PHOTONIC AND DISPLAY DEVICES	1
1.1 Background.....	1
1.2 Literature Review of Optical Fluid-based Photonic and Display Devices	2
CHAPTER 2 ADAPTIVE LIQUID LENSES BASED ON FLUIDIC PRESSURE.....	23
2.1 Membrane-encapsulated Liquid Lens Actuated by Photo-controlled Polymer	23
2.2 Adaptive Mechanical-wetting Lens for Visible and Near Infrared Imaging	31
2.3 Summary.....	40
CHAPTER 3 DIELECTRIC LIQUID LENSES.....	42
3.1 Dielectric Liquid Microlens with Well-shaped Electrode.....	42
3.2 Dielectric Liquid Microlens with Switchable Negative and Positive Optical Power	49
3.3 Electro-optical Properties of Dielectric Liquid Microlens	56
3.4 Summary.....	62
CHAPTER 4 DISPLAYS AND OPTICAL SWITCHES BASED ON DIELECTROPHORETIC EFFECT	64
4.1 Color Display Based on Dielectric-Effect Induced Light Channel.....	64
4.2 Color Display and Variable Optical Attenuator Based on Voltage-Stretchable Liquid Crystal Droplet.....	72

4.2.1 Color Display Based on Voltage-Stretchable Liquid Crystal Droplet.....	72
4.2.2 Variable Optical Attenuator Based on Dielectrically Stretched Liquid Crystal Droplet	81
4.3 Optical Switch Based on Variable Aperture.....	88
4.4 Optical Switch at 1550nm Based on Position-shifting Liquid Droplet.....	95
4.5 Summary.....	105
CHAPTER 5 SUMMARY	108
LIST OF REFERENCES	113
LIST OF PUBLICATIONS.....	110

LIST OF FIGURES

Figure 1.1: Membrane-encapsulated liquid lens based on fluidic pressure.	4
Figure 1.2: Structure of the lens: (a) Top substrate, (b) Bottom substrate, and the (c) Non-focusing state and (d) Focusing state.	5
Figure 1.3: (a) The prototype of a <i>Dynamorph Lens</i> and (b)-(d) The cross-section views of the lens and its focusing mechanism.....	6
Figure 1.4: Adaptive-focus lens based on stimuli-responsive hydrogel. (a) Lens structure, (b) Variable focus mechanism, (c)-(e) The shape of the liquid lens varies with temperatures.	7
Figure 1.5: A pH-sensitive liquid microlens using AA hydrogel. (a) Lens structure, (b)-(c) The volume of the hydrogel ring expands at basic solution, (d)-(e) Focal length and lens shape change with the pH value.	8
Figure 1.6: (a) Optical microscope image of a PPLN sample with a square array of reversed domains, the period of the structures is $\sim 200 \mu\text{m}$, (b) Charge redistribution at heating (top) and cooling (bottom) process , (c) The oil coated sample under heating and (d) cooling process, and image observed through (e) the region outside the lens and (f) the up-right microlens.	9
Figure 1.7: (a) Schematic of the liquid lens showing the electrode embedded at each contact circle, (b) $t=0$, $V= -1.3\text{volts}$ is applied to the top capillary surface of the lens, (c) $t=3\text{min}$, light is focused, and at $t=5\text{min}$, $V= 1.3\text{volts}$ is applied to the top capillary surface of the lens and (d) $t=8\text{min}$, light is defocused.	10
Figure 1.8: Electro-wetting lens (a) Lens structure at V off, (b) Lens shape change at V on, (c)-(e) Tuning states of the lens at different operating voltages.....	12
Figure 1.9: (a) The structure of the channel for EMPs, and (b)-(e) EMPs at various voltages.....	13

Figure 1.10: Elctrowetting driven optical switch based on variable aperture at (a) V-off state and (b) V-on state.	14
Figure 1.11: Elctrowetting display of (a) colored voltage-off state, and (b) transparent voltage-on state.	14
Figure 1.12: (a) The lens structure at V off (solid line) and V on (dashed line), and (b) Images captured through the lens at V=0 and V=75V _{rms}	18
Figure 1.13: (a) Side-view structure of the lens cell, (b) Definition of the involved parameters and imaging properties of two liquid lenses at (c) V=0, (d) V=60 V _{rms} , and (e) Refocused state.	19
Figure 1.14: (a) Side-view of the (a) device structure, (b) the beam steering by the tilted liquid-liquid interface, and (c) experimental results of the He-Ne laser beam steering angle at various voltages.....	20
Figure 1.15: Dielectric liquid iris at (a) V-off state , (b) V-on state and (c) measured and fitted aperture [A(V)] of the dielectric liquid iris at various voltages.....	21
Figure 2.1: Schematic of experimental geometry and the effect of laser-induced LC reorientation: (a) Bending away from the laser beam when $E \perp n$, and (b) Bending towards when $E \parallel n$	25
Figure 2.2: Structure of a tunable lens actuated by photo-polymer (a) Top glass slab, (b) Bottom glass slab, side view of the lens cell in (c) non-focusing and (d) focusing states.	25
Figure 2.3: (a) Deformation of the photo-polymer under blue laser irradiation and (b) Experimental set-up for the actuation of the membrane-encapsulated liquid lens.	27
Figure 2.4: Liquid lens at (a) non-focusing state, (b) focusing state, and (c) Measured focal length of the lens at different power densities.	28
Figure 2.5: (a) Tunable liquid lens system, (b) Voltage-on state and -off state of a TN LC cell.	30

Figure 2.6: Device structure of a mechanical-wetting lens: (a) Assembled system, (b) Side-view of the reservoir body, and (c) Cap with a bump inside.	32
Figure 2.7: Side view of a mechanical-wetting lens structure in (a) Initial state, (b) Further positive state, and (c) Negative state.....	33
Figure 2.8: Transmission spectra of SL-5267 and Glycerol measured from 400 nm to 2000 nm.	33
Figure 2.9: Images taken through the lens in (a) Initial state, (b) Further positive state, (c) Negative state, and (d) Len’s resolution at the initial state.	37
Figure 2.10: (a) BFD measurement of the positive lens, (b) BFD measurement of the negative lens, and (c) Measured BFD vs. traveling distance of the bottom cap.....	38
Figure 2.11: (a) Experimental set-up for lens testing under $\lambda=1310\text{nm}$ laser illumination, Light spots taken in (b) initial state, (c) less positive state, and (d) negative state.	38
Figure 3.1: Side-view structure of the lens cell: (a) Voltage off, and (b) Voltage on.	43
Figure 3.2: Side view of the device fabrication procedure: (a) Making lens cell and UV exposure, (b) Peeling off the stamper, (c) Coating Au +Pd electrode, and (d) Dropping liquids and sealing the cell.	44
Figure 3.3: Simulation results of the electric field of the two structures at $V=100V_{\text{rms}}$ (a) Common planar-electrodes, and (b) Top planar-electrode and bottom well-shaped electrode.....	44
Figure 3.4: (a) The image of the lens cell at the position of surface focus, (b) At the position of the smallest spot size, (c) Image at focus, (d) Resolution test, (e) Tunable state of the lens at $V=0$, (f) $V=40 V_{\text{rms}}$, and (g) $V=88 V_{\text{rms}}$	46
Figure 3.5: (a) Measured focal length of the microlens at different driving voltages, and (b) Lens structure and parameters for ZEMAX simulation.	48

Figure 3.6: (a) Imaging properties of the microlens array, and (b) Microlens array at $V=0$ (c) Tunable state of the lens driven at $88V_{\text{rms}}$.	49
Figure 3.7: Side-view structure of the lens cell at (a) voltage-off state, and (b) voltage-on state.	50
Figure 3.8: The device fabrication procedure: (a) UV exposure, (b) Peeling off the stamper, (c) Aligning the polymer bases under microscope, then coating Au + Pd electrode, and (d) Dropping liquids and sealing the cell.	51
Figure 3.9: (a) Top view of the device, and the image observed through the microscope at $L=3\text{mm}$ (b) without any liquid lens (c)-(g) with the dielectric liquid microlens driven at different voltages, and at $L=7\text{mm}$ (h) $V=0$, and (i) $V=90V_{\text{rms}}$.	52
Figure 3.10: (a) Experimental set-up for measuring the focal length, (b) Focusing on the top glass substrate, (c) Focusing on the image of the target, and (d) Measured focal length at various driving voltages.	54
Figure 3.11: Lens structure and parameters for ZEMAX simulation.	55
Figure 3.12: Experimental set-up for measuring the response time.	55
Figure 3.13: (a) Side-view of the dielectric liquid lens cell and (b) Experimental set-up for measuring the electro-optical properties of liquid droplets.	56
Figure 3.14: Images observed through an optical microscope by focusing on (a) droplet surface, (b) Defocus state at $V=0$, and (c) Focus state at $V=60 V_{\text{rms}}$.	59
Figure 3.15: Voltage-dependent intensity change of (a) a $210\text{-}\mu\text{m}$ -aperture droplet at $f=300\text{Hz}$ at forward and backward scans, and (b) at $f=300\text{ Hz}$ and 10 kHz frequencies.	60
Figure 3.16: Measured response time of (a) a $210\text{-}\mu\text{m}$ -aperture droplet at different voltages (solid circles: rise time, open circles: decay time), and (b) different-sized droplets under a square burst driving.	61

Figure 4.1: (a) Side-view structure of the cell at $V=0$ (b) Droplet dome touching the top substrate under a voltage, and (c) Enlarged touching area when the voltage is increased.	65
Figure 4.2: Force analysis (dielectric force and interfacial tensions) for the system balance.	66
Figure 4.3: A droplet cell for black/white switch driven at (a) $V=0$, (b) $25 V_{\text{rms}}$, and (c) $40 V_{\text{rms}}$	68
Figure 4.4: A droplet cell for black/red switch driven at (a) $V=0$, (b) $V= 35 V_{\text{rms}}$, (c) $V=42 V_{\text{rms}}$, (d) $V=50 V_{\text{rms}}$	69
Figure 4.5: Measurement set-up for electro-optical properties.	70
Figure 4.6: A droplet cell for blue/white switch driven at (a) $V=0$, (b) $V= 25 V_{\text{rms}}$, (c) $V=30 V_{\text{rms}}$, (d) $V=44 V_{\text{rms}}$	71
Figure 4.7: Two approaches for obtaining a wide-view and high transmittance display thru edge-lit backlight.	71
Figure 4.8: (a) Side-view of the cell structure at V -off, (b) black state at V -on, and (c) layout of the bottom substrate. The dimension of the hole and ITO stripes are not drawn by scale.	73
Figure 4.9: Droplet deformation (black pixel switch) at various voltages.	75
Figure 4.10: Dielectric force, interfacial tension and viscosity friction analysis.	77
Figure 4.11: Measurement of the switching time.	78
Figure 4.12: Droplet deformation (blue and red pixels) at various voltages.	79
Figure 4.13: 1×6 droplet array switching	80
Figure 4.14: (a) Side-view structure of the VOA at $V=0$, (b) $V>0$, and (c) the layout of the interdigitated ITO electrode and Teflon layer on the bottom substrate (The size of the hole and the width of electrode strips are not drawn by scale.)	82
Figure 4.15: Experimental set-up for characterizing the VOA sample.	83

Figure 4.16: Measured attenuation and PDL vs. operating voltages ($\lambda=1550\text{nm}$).	84
Figure 4.17 . Droplet surface stretching and beam deflection with increased voltage.	85
Figure 4.18: Measured VOA broadband operation at (a) $V=25V_{\text{rms}}$ (~5dB attenuation setting), (b) $V=30V_{\text{rms}}$ (~20dB attenuation setting) and (c) $V=35V_{\text{rms}}$ (~30dB attenuation setting) for C-Band operations with OSA resolution of 10 dB/Div, and (d) measured high resolution VOA broadband response at $V=20V_{\text{rms}}$ (~3dB attenuation setting) with OSA resolution of 2 dB/Div.	86
Figure 4.19: Measured switching time at $V=40V_{\text{rms}}$ ($\lambda=1550\text{nm}$).	87
Figure 4.20: Device structure and the surface stretching of a ring-shaped liquid droplet at various voltages.....	89
Figure 4.21: Fabrication procedure of an optical switch with bracelet-like liquid on the polymer wall surface of each pixel hole	90
Figure 4.22: The aperture of a pixel changed with different voltages.	92
Figure 4.23: Hole array at (a) $V=0$ (left sub-figure) and $V=80 V_{\text{rms}}$ with or without surface defects (right sub-figure), and (b) $V=0$ (left sub-figure) and $V=80 V_{\text{rms}}$ with normally filled or excessively filled LC (right sub-figure, the holes in middle column are excessively filled).	93
Figure 4.24: Aperture change of a pixel filled with black LC. (a) $V=0$, (b) $V=80 V_{\text{rms}}$, and (c) time dependent transmitted light intensity.	94
Figure 4.25: Schematic structure of the cell and its operation mechanism. (a) The droplet pinned down on the hole surface at $V=0$, (b) the droplet moved to the right side at $V=V_1$, and (c) the top view showing the position of the droplet at $V=0$ and $V=V_1$. The droplet size and electrode dimensions are not drawn by scale	97

Figure 4.26: Simulated electric field distribution: (a) along x-axis and (b) along z-axis. The ITO electrode width is 100 μm , electrode gap is 20 μm , and the distance along z-axis to the electrode surface is 50 μm . The device structure is not drawn by scale.99

Figure 4.27: Measured transmission spectra of Glycerol and optical fluids (SL-5267) from 500 nm to 2000 nm. The thickness of each liquid is ~ 4 mm 101

Figure 4.28: The position change of glycerol droplet at different voltages: (a) $V=0$, (b) $V=45 V_{\text{rms}}$, and (c) $V=60 V_{\text{rms}}$. The diameter of the droplet is ~ 4.5 mm..... 102

Figure 4.29: Electro-optical characteristics of the IR switch at $\lambda=1.55 \mu\text{m}$. (a) A simple set-up, (b) intensity change vs. voltage, and (c) intensity change vs. time. 103

LIST OF TABLES

Table 2.1: Properties of liquid-1 (L1: SantoLight™ Optical Fluids SL-5267, Santovac® Fluids) and liquid-2 (L2: Glycerol, Sigma-Aldrich).....	34
Table 3.1: Properties of liquid-1 (L1: Glycerol, Sigma-Aldrich), liquid-2 (L2: SantoLight™ Optical Fluids SL-5267, Santovac® Fluids) and polymer wall (NOA81).....	43
Table 4.1: Properties of liquid-1 (L1: Glycerol, Sigma-Aldrich), liquid-2 (L2: ZLI-2585, Merck)	67
Table 4.2: Properties of liquid-1 (L1: ZLI-4389, Merck), liquid-2 (L2: Silicone Oil, Sigma-Aldrich)	74
Table 4.3: Properties of liquid-1 (L1: Glycerol, Sigma-Aldrich) and liquid-2 (L2: SantoLight™ Optical Fluids SL-5267, Santovac® Fluids).	100

LIST OF NOMENCLATURE

IR	Infrared
LC	Liquid Crystal
PDMS	Polydimethylsiloxane
EMP	Electrowetting Microprisms
ITO	Indium Tin Oxide
LCD	Liquid Crystal Display
FTMA	Redox Surfactant
RMS	Root-Mean-Square
AA	Acrylic Acid
NIPAAm	N-isopropylacrylamide
LN	Lithium Niobate
PPLN	Periodically Poled Lithium Niobate
EWOD	Electrowetting on Dielectric
DEP	Dielectrophoresis, Dielectrophoretic
PMMA	Polymethylmethacrylate
2D	Two Dimensional
3D	Three Dimensional
TN	Twisted Nematic
LD	Laser Diode
CCD	Charge-coupled Device
NOA	Norland Optical Adhesive

USAF	U.S. Air Force
BFD	Back Focal Distance
LED	Light Emitting Diode
VOA	Variable Optical Attenuator
VFOA	Variable Fiber Optical Attenuator
SMF	Single Mode Fiber
AR	Anti-Reflection
LED	Light Emitting Diode
PDLC	Polymer-dispersed Liquid Crystal
PNLC	Polymer-network Liquid Crystal
PDL	Polarization Dependent Loss
GRIN	Gradient Index
PI	Polyimide

CHAPTER 1 INTRODUCTION TO OPTICAL FLUID-BASED PHOTONIC AND DISPLAY DEVICES

1.1 Background

Conventional solid-state photonic devices have ultra-high optical performance and durability, but minimal adaptability. Recently, there has been intense interest in photonic devices based on optical fluids, including adaptive-focus lenses, beam steers, tunable irises, optical switches and displays. With optical interfaces formed by liquids, such devices exhibit unique properties, which are not achievable in conventional solid-state photonic devices. By manipulating the optical interface dynamically, the optical output can be reconfigured or adaptively tuned in real time. In addition, liquid surface (or liquid-liquid interface) is intrinsically smooth because of the minimum interfacial energy, and thus polishing is not required. Compared to photonic devices with an optical surface formed by one liquid, those with a liquid-liquid optical interface have additional advantages. They are insensitive to vibrations if the two liquids are matched in density. Moreover, they are easy for packing and integration with solid-state photonic devices, microanalysis and lab-on-a-chip systems. Since the employed liquids are usually isotropic, these optical fluid-based photonic and display devices are polarization insensitive and broadband.

Different operation principles of optical fluid-based photonic devices have been proposed, e.g., fluidic pressure [1-10], electrochemistry [11], thermal effect [12,13], environmentally adaptive hydrogel [14-16], electro-wetting [17-24] and dielectrophoresis (DEP) [25-38].

The main limitation of the optical fluid-based photonic devices is the choice of liquids. The highest refractive index of liquid is ~1.75, which is much lower than that of solids. Besides, they have limited transparency in the infrared (IR) range, especially in the 3-5 μm and 8-12 μm , therefore, they are mostly used in the visible region. To optimize the device performances from material aspects, there are some criteria to choose the fluids, especially when two liquids are employed in the devices. For example, these two fluids should be immiscible with each other, non-toxic, stable and optically transparent for imaging applications. Other properties, such as refractive index, relative permittivity (dielectric constant) and surface tension, should also be taken into account for different operation principles.

1.2 Literature Review of Optical Fluid-based Photonic and Display Devices

A conventional lens is made of glass, polymer or other solid material and has a fixed focus due to the rigid surface profile. In order to change focal length, at least two solid lenses should be integrated into a system with adjustable distance along the optical axis between two lenses. Such a zoom lens system has high resolution and small aberration but is usually bulky and heavy. Therefore, a single lens with adaptive focal length is highly desirable for applications such as zoom lens, image processing, and portable electronic devices [3,7,21,26,39-44]. Several adaptive lenses have been developed, and can be roughly categorized into two groups: liquid crystal (LC) lenses [45-53] and liquid lenses [4,8,11,14-16,26,28,32,36,39,51,54-57].

The concept of LC lens was first proposed in 1977 [45]. Nematic liquid crystals are rod-like molecules. When aligned in a homogeneous cell, their long axes are approximately parallel to each other. This averaged alignment direction is called LC director. Due to dielectric and

optical anisotropies, the LC directors can be reoriented by an external electric field, which induces phase retardation or phase change of the incident light. Gradient phase change induced by an inhomogeneous electric field forms the foundation for the adaptive LC lenses. Several approaches to fabricate LC lenses have been demonstrated, such as surface relief LC layer [46], modal addressing [47], line- or hole-patterned electrodes [48], polymer-stabilized LC networks [49], curved and flat electrodes [50-53]. The focal length of an LC lens is related to lens radius (r), refractive index difference between center and boarder of the lens (δn), and LC layer thickness (d) as $f \sim r^2/(2d \cdot \delta n)$ [50]. To obtain a short focal length, we could increase $d \cdot \delta n$ or reduce the lens aperture. Most of high birefringence LCs have $\Delta n \sim 0.4$ [58]. Scientists present some ultra-high $\Delta n (>0.6)$ LCs, but the large viscosity will lead to a slow response time [59]. On the other hand, increasing the LC layer thickness will also induce such effect. Moreover, the phase profile of a simple LC lens is not so spherical that its resolution and image quality are limited. Therefore, LC lens is more suitable for applications of small aperture lenses. Most LC lenses are polarization dependent, which can be solved by stacking two devices in orthogonal directions.

Adaptive-focus liquid lenses are based on physical adjustment of the lens shape. Compared to an LC lens, the adaptive-focus liquid lens exhibits some attractive features, such as polarization independence, large aperture size, and strong focusing power.

In a typical membrane-encapsulated liquid lens activated by fluidic pressure, as Figure 1.1 shows, one surface of the lens is made of elastic membrane, which acts as a deformable surface; its focal length is tuned by pumping liquid in or out of the lens chamber which, in turn, changes the surface profile of the liquid lens. The focal length ranges from several hundreds of

microns to infinity in both positive and negative focal length [2]. For such type of lenses, the operation mechanism is simple but a fluid pumping system is needed [1-3,5-7], which is not so convenient for portable devices. In 2007, Ren et al proposed a revised lens structure for a liquid lens without a pumping system [4]. The device structure is shown in Figure 1.2. A liquid of a fixed volume is sandwiched between two slabs which are sealed with glue. Each slab has a hole and the two holes are sealed with Polydimethylsiloxane (PDMS) membranes. Without an external force, the membrane of the lens cell is in a flat and non-focusing state. When an external pressure is applied to deform the outer elastic membrane, the liquid in the chamber is redistributed, causing the inner elastic membrane to swell outward and forming a plano-convex lens. However, membrane-encapsulated liquid lens experiences the gravity effect in vertical placement, which may cause an asymmetric shape and degrade the image performances. Besides, making high quality PDMS membrane and uniformly installing it on the lens frame are also challenging. All these factors limit their optical performances.

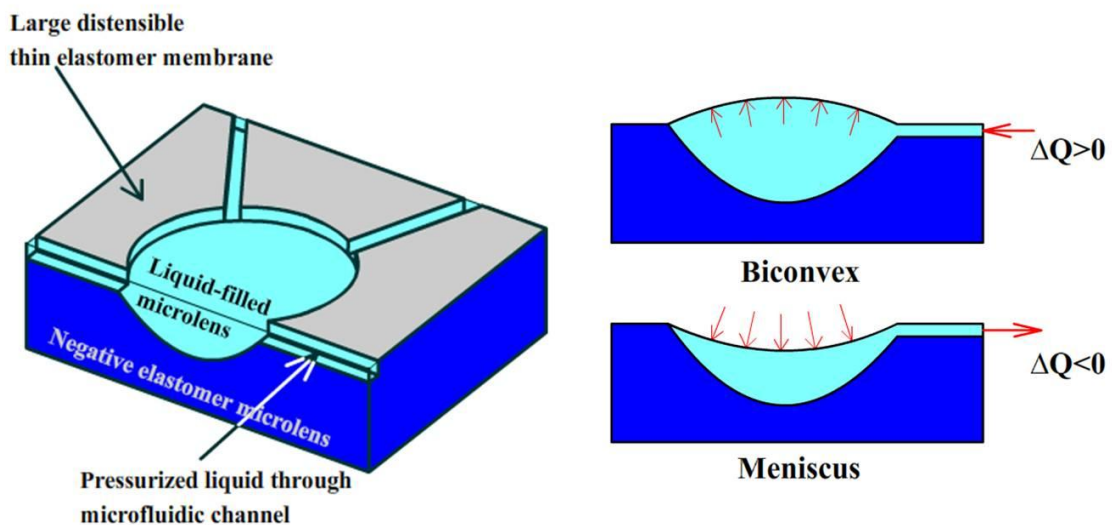


Figure 1.1: Membrane-encapsulated liquid lens based on fluidic pressure.

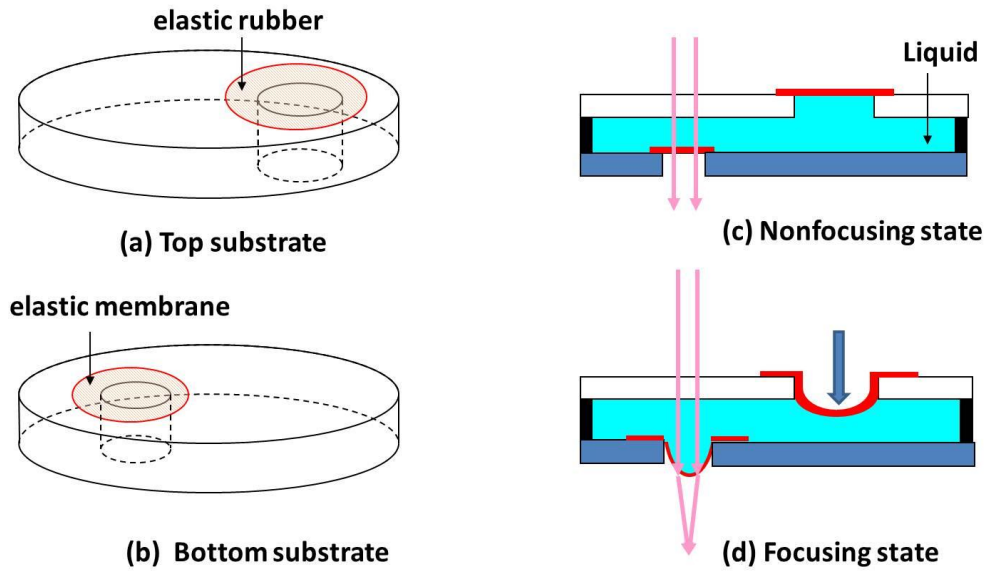


Figure 1.2: Structure of the lens: (a) Top substrate, (b) Bottom substrate, and the (c) Non-focusing state and (d) Focusing state.

In 2009, Oku et al demonstrated a *Dynamorph Lens* using a liquid-liquid interface between two immiscible liquids with a pinned contact line as a variable refractive surface [54]. The curvature of the interface is changed by liquid pressure through a piezostack actuator via a built-in hydraulic amplifier, as shown in Figure 1.3(a). The lower chamber is equipped with a deformable membrane that a piezostack actuator thrusts to change the chamber volume. When the piezostack actuator extends, the lower chamber volume decreases, and the surplus liquid volume presses the interface to change from a convex shape to a concave shape, as shown in Figure 1.3(b)-(d). Such a liquid lens is reported to have a step response time of 2 ms, a refractive power range of 52 D, and a root-mean-square (rms) wavefront error of 80.3 nm.

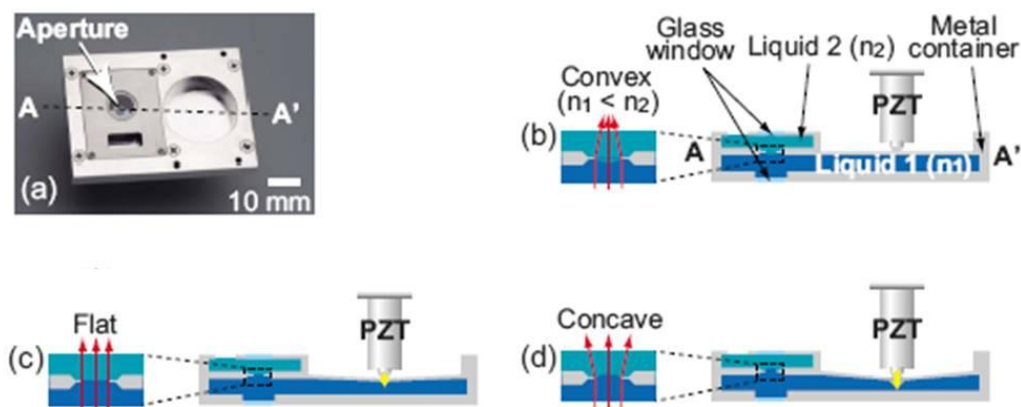


Figure 1.3: (a) The prototype of a *Dynamorph Lens* and (b)-(d) The cross-section views of the lens and its focusing mechanism.

In 2006, Dong et al demonstrated a liquid lens based on environmentally adaptive hydrogel, which can be stimulated by temperature or pH value change [14]. The lens consists of a stimuli-responsive hydrogel ring placed within a microfluidic channel system, and sandwiched between a glass plate and an aperture slip, as Figure 1.4(a) shows. The core part of this design is the temperature-sensitive N-isopropylacrylamide (NIPAAm) hydrogel that expands at low temperatures and contracts at high temperatures, with a volume transition temperature of approximately 32 °C. At low temperatures, the liquid meniscus grows, because the physical volume increase of the hydrogel upon expansion is larger than the volume of water absorbed by the hydrogel ring; at high temperatures, the liquid meniscus retreats because the water released by hydrogel is unable to compensate for the decrease in physical volume of the hydrogel ring. The net volume change causes a change in the pressure difference across the water-oil interface, which directly determines the geometry of the liquid meniscus, as shown in Figure 1.4(b) - Figure 1.4(f). Its focal length changes from several millimeters to infinity in both positive and negative regimes as the temperature varies, and the response time is ~ 20-25 seconds. If the ring is made by pH-sensitive acrylic acid (AA) hydrogel, then the lens will be stimulated by pH value

change, as shown in Figure 1.5(a). The AA hydrogel expands in basic solutions and contracts in acidic solutions with a volume transition point at pH 5.5. The volume of the hydrogel ring is regulated by exposing its outside periphery to various pH buffers flowing through the microchannel (Figure 1.5(b) and (c)). As the buffer solution's pH value increases, the hydrogel expands, the meniscus bulges upward, and the focal length of the microlens decreases (Figure 1.5(d) and (e)). The response time is ~12 seconds.

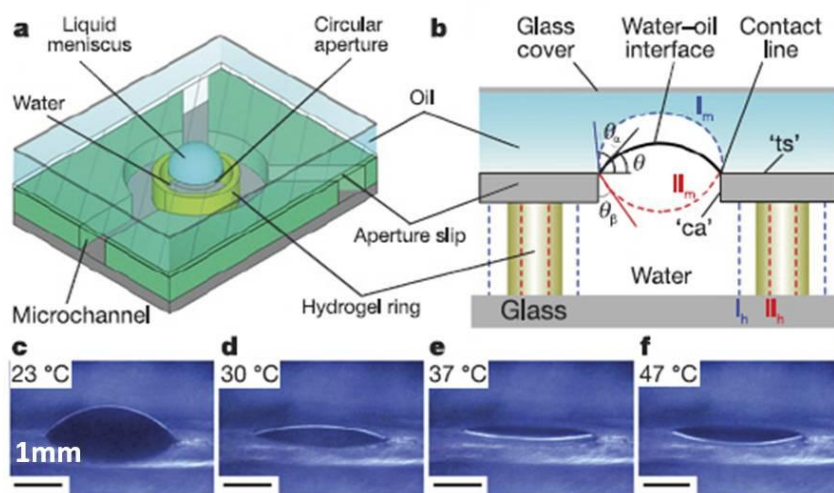


Figure 1.4: Adaptive-focus lens based on stimuli-responsive hydrogel. (a) Lens structure, (b) Variable focus mechanism, (c)-(e) The shape of the liquid lens varies with temperatures.

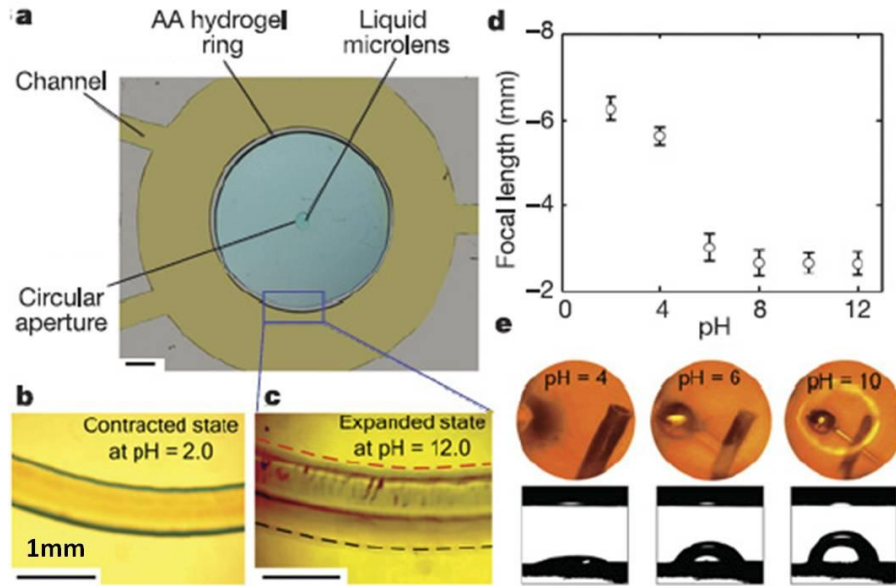


Figure 1.5: A pH-sensitive liquid microlens using AA hydrogel. (a) Lens structure, (b)-(c) The volume of the hydrogel ring expands at basic solution, (d)-(e) Focal length and lens shape change with the pH value.

In 2008, Grilli et al demonstrated a liquid microlens array based on the electric field activation of periodically poled lithium niobate (PPLN) by the pyroelectric effect [13]. The PPLN sample is fabricated by electric field poling process [60,61], as Figure 1.6(a) shows. A thin liquid film ($\sim 200\mu\text{m}$ thick) is spread on a PPLN crystal substrate. The lack of inversion symmetry in lithium niobate (LN) induces the pyroelectricity. The change of the polarization occurring with temperature variation causes a lack or excess of surface screening charge, as Figure 1.6(b) shows. Consequently, an electrostatic state appears and generates a high electric field at the crystal surface [62]. The lens-like array topography exhibited by the oil film results from the equilibrium condition between surface tensions and electric forces related to the charge redistribution on the PPLN substrate. Therefore, the topography variation builds up a liquid microlens array activated by the temperature gradients on the LN surface [63]. Figure 1.6(c) and (d) depict the optical microscope image of the oil coated sample during heating and cooling

process, and Figure 1.6(e) and (f) show the focusing capability of the microlenses. Such a lens has an electrode-less and circuit-less configuration, which enables higher degree of integration compared to conventional devices equipped with metal electrodes. But the gravity effect and the sealing method are still a technical challenge.

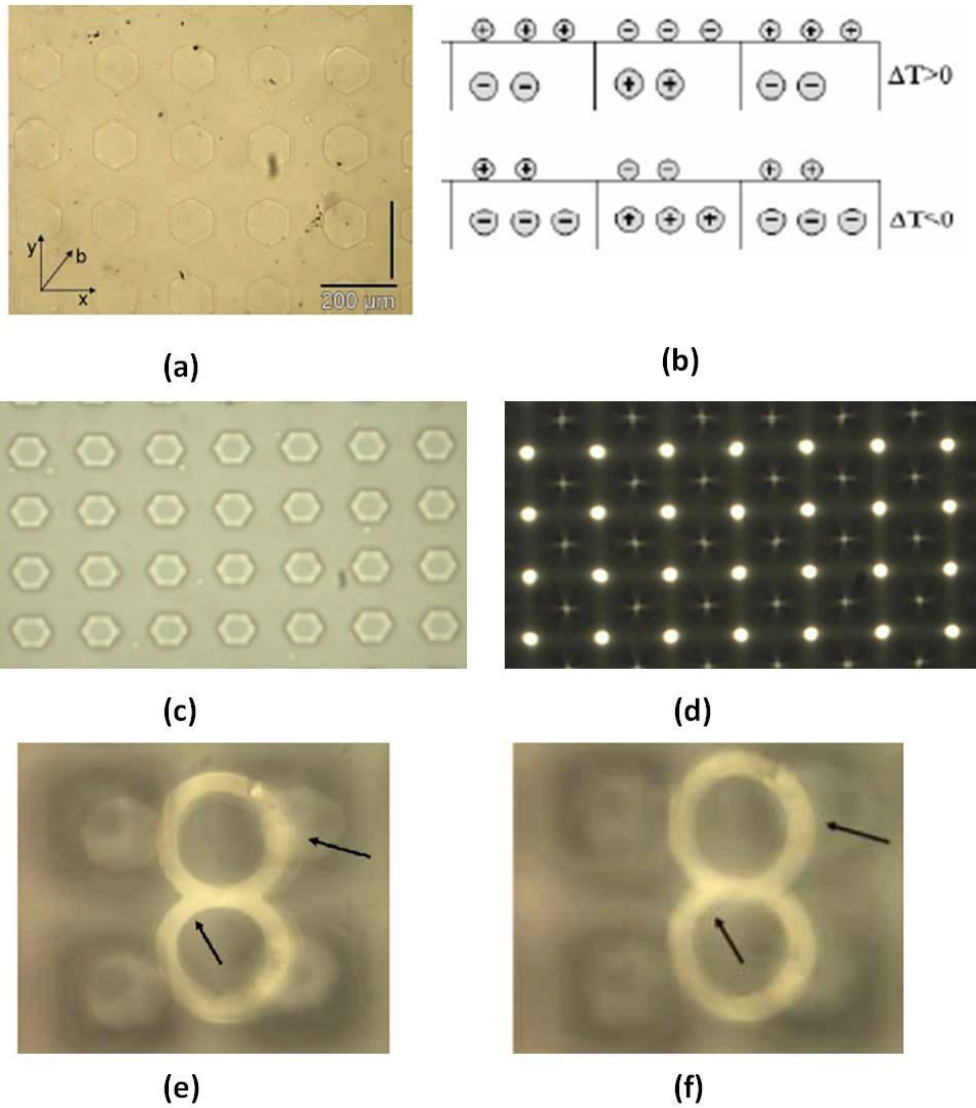


Figure 1.6: (a) Optical microscope image of a PPLN sample with a square array of reversed domains, the period of the structures is $\sim 200 \mu\text{m}$, (b) Charge redistribution at heating (top) and cooling (bottom) process, (c) The oil coated sample under heating and (d) cooling process, and image observed through (e) the region outside the lens and (f) the up-right microlens.

In 2005, Lopez et al demonstrated an electrochemically activated adaptive liquid lens utilizing a redox surfactant (FTMA) solution as the lens medium [11]. The adaptive liquid lens consists of two capillary surfaces, as shown in Figure 1.7(a). Applying a voltage difference across the lens produces a reversible reduction-oxidation process that modifies the surface activity of the surfactant, which increases during oxidation occurs and decreases during reduction, with a magnitude of $\sim 8\text{dyn/cm}$. Therefore, the surface tension change on one capillary surface relative to the other will induce a curvature change in the capillary surfaces, leading to a liquid redistribution and a focal length change, as shown in Figure 1.7(b) And Figure 1.7(c), such a process is reversible, as shown in Figure 1.7(d). In this millimeter-scale lens, the focal length could be tuned between 0.5 mm and infinity depending on the volume. The operating voltage is low, but the switching takes several minutes to finish one cycle (defocusing to focusing to defocusing again).

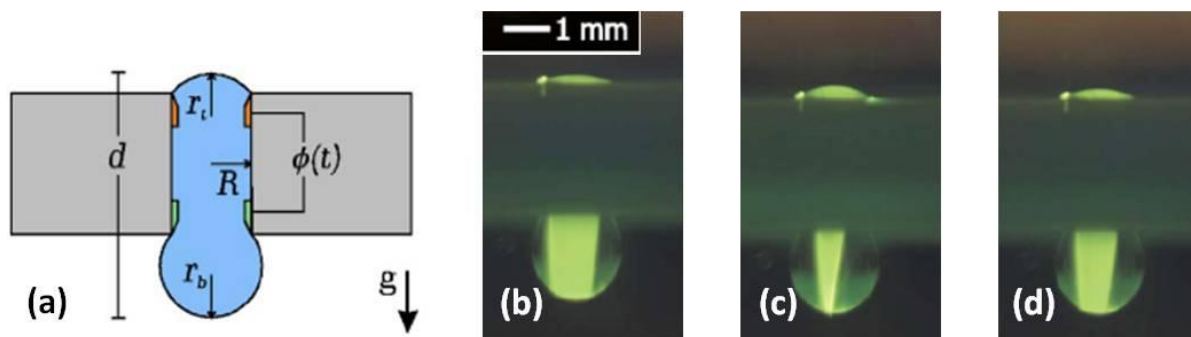


Figure 1.7: (a) Schematic of the liquid lens showing the electrode embedded at each contact circle, (b) $t=0$, $V= -1.3\text{volts}$ is applied to the top capillary surface of the lens, (c) $t=3\text{min}$, light is focused, and at $t=5\text{min}$, $V= 1.3\text{volts}$ is applied to the top capillary surface of the lens and (d) $t=8\text{min}$, light is defocused.

When an electrically conductive liquid drop falls on a solid surface and has a contact angle on the surface, the contact angle (or the wetting effect) can be tuned if a suitable voltage is applied across the liquid and a counter-electrode underneath the solid surface. Such

electrowetting phenomenon was first studied by Lippmann [64] and Frumkin [65]. In early 1990s, Berge introduced a thin insulating layer to separate the conductive liquid from the metallic electrode in order to eliminate the electrolysis problem [18]. This concept is known as electrowetting on dielectric (EWOD), which has become a popular mechanism for manipulating liquid surface. Applications range from adaptive-focus lenses to prisms, optical attenuators, and electronic displays.

Figure 1.8(a) depicts the side-view of an electrowetting lens [39]. A conductive liquid forms a droplet on the bottom surface of the cylinder and an insulating liquid fills in the surrounding area. The inside of the cylinder is coated with a hydrophobic insulator. The initial contact angle θ_0 of the droplet on the insulator is determined by the interfacial surface tension among the liquids and wall, as expressed by Eq. (1.1):

$$\cos \theta_0 = \frac{\gamma_{wi} - \gamma_{wc}}{\gamma_{ci}} \quad (1.1)$$

where γ_{wi} is the interfacial tension between the wall and the insulating liquid, γ_{wc} between the wall and the conducting liquid, and γ_{ci} between the two liquids. When a voltage is applied, the dielectric layer functions as a charged capacitor (Figure 1.8(b)), the effective interfacial tension between the conductive droplet and insulator decreases, leading to a decreased contact angle θ_v , as expressed by Eq.(1.2):

$$\cos \theta_v = \cos \theta_0 + \frac{\epsilon}{2\gamma_{ci}d_f} V^2 \quad (1.2)$$

where ϵ and d_f is the dielectric constant and insulating layer thickness, respectively, and V is the applied voltage. Therefore, the focal length can be varied by the voltage (Figure 1.8(c)-(e)).

Removing the voltage discharges this insulator layer and the droplet returns to its original state.

For a 3-mm-diameter lens, the focal length can be tuned from 20mm to -10mm.

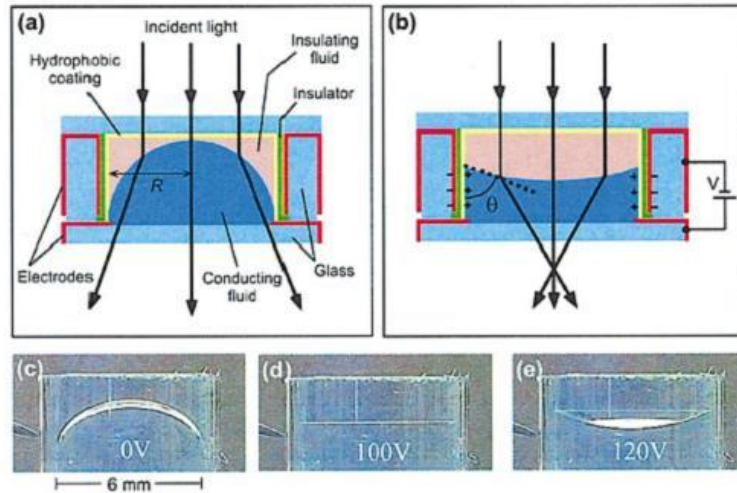


Figure 1.8: Electro-wetting lens (a) Lens structure at V off, (b) Lens shape change at V on, (c)-(e) Tuning states of the lens at different operating voltages.

Since the contact angle between the droplet and sidewalls (insulator layer) changes with voltage, if each sidewall has an independent voltage source, then the contact angle on the sidewall can be individually modulated. Based on this idea, electro-wetting micropisms (EMPs) have been demonstrated [21]. The device structure is shown in Figure 1.9(a); each Si sidewall is equipped with an independent DC voltage source, and an electrically grounded Ni-Ti wire is inserted in the channel liquid. When the contact angles on the left (θ_{VL}) and right (θ_{VR}) sidewalls satisfy $\theta_{VR} + \theta_{VL} = 180^\circ$, a straight-line meniscus from sidewall to sidewall can be obtained. Figure 1.9(b)-(e) show the steering angle change of the EMPs at various voltages. Continuous beam steering through an angle of $14^\circ (\pm 7^\circ)$ has been demonstrated with a liquid index of $n=1.359$.

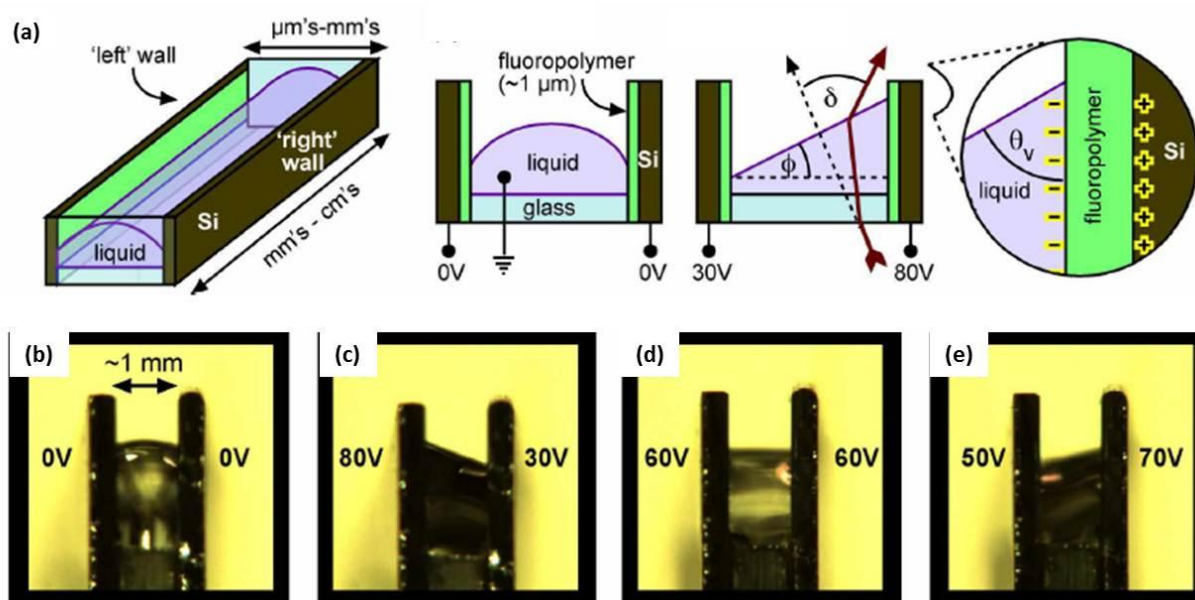


Figure 1.9: (a) The structure of the channel for EMPs, and (b)-(e) EMPs at various voltages.

The liquids in the electrowetting lens and microprism are transparent and work as a refractive optical surface. Electrowetting devices adopting a transparent liquid and a non-transparent liquid, e.g., optical switch and electronic display have also been demonstrated. Figure 1.10 shows the side-view structure of an electrowetting-driven optical switch with tunable aperture. At $V=0$, light is absorbed by the non-transparent oil film (dye-doped oil film), as shown in Figure 1.10(a). Under an electric field, the liquid-liquid interface is bent downwards due to the contact angle change. When it touches the bottom substrate, the dye-doped oil film is replaced by a water drop, opening an aperture for the beam to pass through (Figure 1.10(b)). Its diameter can be tuned between 0.2 and 1.2 mm by varying the driving voltage or frequency. At $50V_{\text{rms}}$, the rise and decay time is measured to be ~ 2 and 120 ms, respectively.

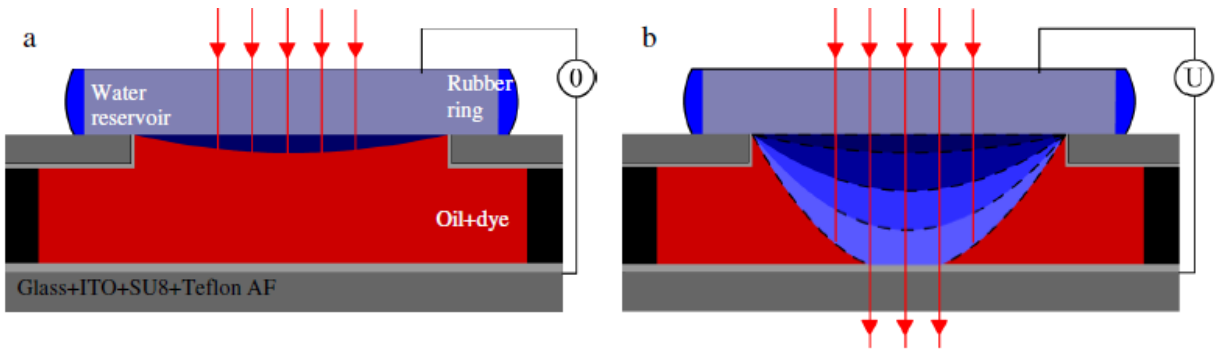


Figure 1.10: Electrowetting driven optical switch based on variable aperture at (a) V-off state and (b) V-on state.

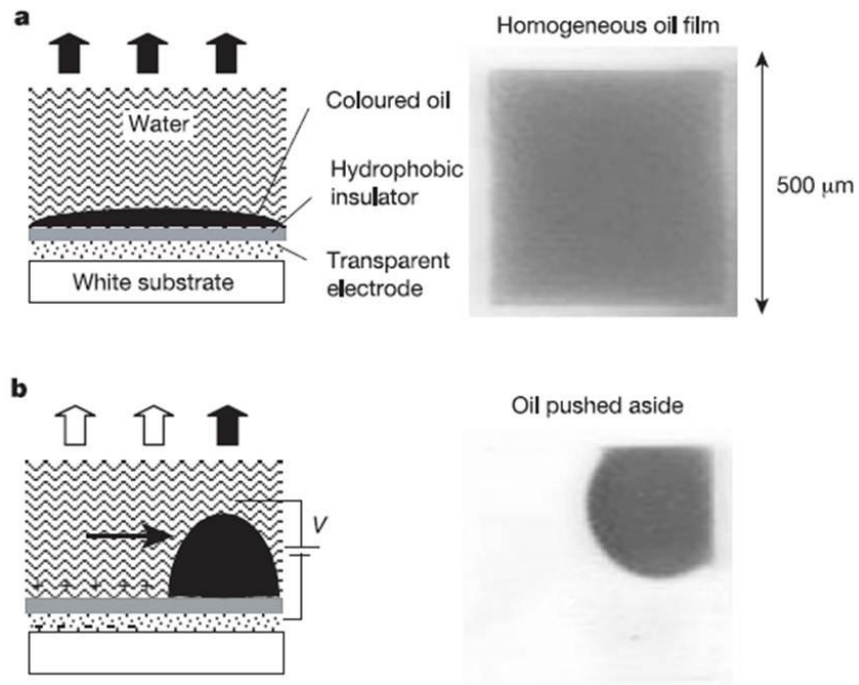


Figure 1.11: Electrowetting display of (a) colored voltage-off state, and (b) transparent voltage-on state.

A video-speed electronic paper based on electrowetting has been demonstrated by Hayes et al in 2003. Figure 1.11 shows the structure and working principle [19]. At voltage-off state, the colored oil film is spread continuously on the insulator layer, due to the dominance of interfacial over gravitational forces in small systems (2mm). When a voltage is applied between

the substrate electrode and the water, to rebalance the interfacial energies the water moves into contact with the insulator and the colored oil is displaced, leading to a transparent state. At 20V, ~70% of the white substrate was exposed, and the reflectivity was measured to be ~35% and contrast ratio 15:1. Its reflectivity R and contrast ratio are comparable to that of electrophoretic displays (R <40% and contrast ratio ~11:1), and are approaching to those of paper (R < 60% and contrast ratio ~15:1). The on and off response time are close to 10ms.

Several electrowetting devices have been commercialized or close to commercial realizations. Nevertheless, there are several technical challenges that still need to be addressed before most electrowetting devices can be translated from laboratory prototypes to commercial products. An important limitation is the contact angle saturation at high voltages [66]; which is still not well understood at this stage. Electrolysis, Joule heating and microbubbles are often generated in the electrowetting devices, which are due to the transportation of the free electric charges and the alternating electric fields [39]. These can be minimized by introducing an insulating layer on the electrodes, but the operating voltage will be increased [67]. Furthermore, high saturated vapor pressure of the conductive liquid (e.g., salty water) requires expensive hermetic packaging (i.e., metal-glass packing) for long term operation [25].

Dielectrophoresis (DEP) is defined as the translational motion of neutral matter caused by polarization effects in a nonuniform electric field [68]. The force resulting from the polarization of the dielectric material is called dielectric force or Kelvin polarization. For a single particle, if treated as an individual dipole, the force can be approximated as [69]:

$$\vec{F}_d = \vec{p} \cdot \Delta \vec{E} \quad (1.3)$$

where p is the dipole moment. For a bulky object, the Kelvin polarization force can be calculated by means of the polarization bulk force. From a microscopic view, the infinitesimal dipoles in an

electric field experience a force that they pass on to the bulky object as a whole. Given the macroscopic polarization P , the Kelvin polarization force density is obtained [70]

$$\vec{f}_{KP} = \vec{P} \cdot \Delta \vec{E} \quad (1.4)$$

Given the polarization of a linear dielectric material with a susceptibility χ_e

$$\vec{P} = \varepsilon_0 \chi_e \vec{E} = \varepsilon_0 (\varepsilon_r - 1) \vec{E} \quad (1.5)$$

the Kelvin polarization force density can be rewritten as:

$$\vec{f}_{KP} = \frac{1}{2} \varepsilon_0 (\varepsilon_r - 1) \nabla (\vec{E} \cdot \vec{E}) \quad (1.6)$$

If a dielectric object with a dielectric constant ε_d is surrounded by a dielectric medium with ε_m , Eq.(1.5) can be replaced by the excess polarization per unit volume

$$\vec{P} = \varepsilon_0 (\varepsilon_d - \varepsilon_m) \vec{E} \quad (1.7)$$

Thus the Kelvin polarization force density is

$$\vec{f}_{KP} = \frac{1}{2} \varepsilon_0 (\varepsilon_d - \varepsilon_m) \nabla (\vec{E} \cdot \vec{E}) \quad (1.8)$$

And the Kelvin polarization force exerted on a dielectric object with a volume V is

$$\vec{F}_{KP} = \int_V \frac{1}{2} \varepsilon_0 (\varepsilon_d - \varepsilon_m) \nabla (\vec{E} \cdot \vec{E}) dV \quad (1.9)$$

From Eq.(1.9), the difference between ε_d and ε_m and the gradient of the electric field play key roles on the dielectric force. Generally speaking, the medium with a larger (smaller) dielectric constant will move to the range with higher (lower) electric field under the influence of DEP.

The dielectric force has been widely used in the manipulations of biomolecules [71], DNA [72], nanowires [73] and nanotubes [74], the operation of droplet-based lab-on-a-chip [75], electrohydrodynamic continuous flow micropumps [76] as well as dielectric micromotors [77].

Recently, the applications have been extended to optical fluid-based photonic and display devices. With a liquid-liquid interface manipulated by the dielectric force, adaptive liquid lenses [26-28,32,36], beam steers [29], tunable irises [33], and optical attenuators [34,35,78,79] based on DEP effect have been demonstrated by researchers. Since the two employed liquids in DEP devices are non-conductive, they can bear a high operating voltage while keeping low power consumption. At the same time, electrolysis, Joule heating and microbubbles which always arise in electrowetting devices [18] can be suppressed.

Dielectric liquid lenses [26-28,32,36], beam steers [29], tunable irises [33], and optical attenuators [34,35,78,79] based on DEP effect have been demonstrated by researchers.

Figure 1.12(a) shows the structure of a dielectric liquid lens demonstrated by Cheng et al in 2007 [26]. The lens consists of a droplet and a surrounding liquid with low and high dielectric constants, respectively. Two indium tin oxide (ITO) glass substrates sandwich the two liquids. A 1- μm -thick Teflon layer was coated on the bottom electrode to reduce friction between the droplet and the glass substrate. The bottom concentric ITO electrodes introduce an inhomogeneous electric field under an operating voltage. The generated dielectric force causes the liquid with a smaller dielectric constant to shrink towards the region with a lower electric field. Due to the interface deformation between the two liquids, the focal length becomes tunable. Figure 1.12(b) shows the images of the word “Green” captured through the liquid lens at $V=0$ and $V=75V_{\text{rms}}$. The focal length of a lens with 3-mm aperture can be tuned from 34mm to 12mm in the range of 0-200 V_{rms} . Rise and fall times are 650ms and 300ms, respectively.

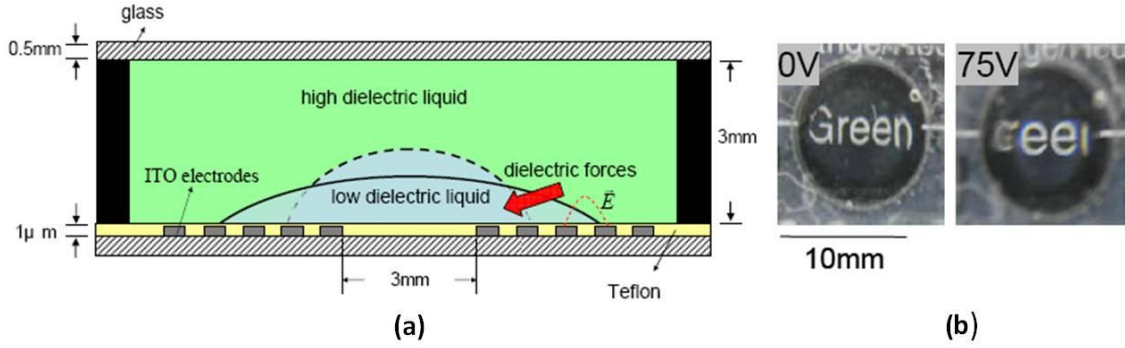


Figure 1.12: (a) The lens structure at V off (solid line) and V on (dashed line), and (b) Images captured through the lens at $V=0$ and $V=75V_{\text{rms}}$

To drive a dielectric lens, the applied electric field should be inhomogeneous in order to generate dielectric force. So the electrode is always etched with holes or rings [26,27]. To simplify the fabrication process, an adaptive dielectric lens using continuous flat electrodes was demonstrated by Ren et al in 2008 [28]. Figure 1.13(a) shows the side-view structure of the lens cell. The structure is similar to Cheng's dielectric liquid lens [26], except that the ITO electrodes on the top and bottom substrates are continuous. Under an applied voltage, the electric field exerted on the droplet can be expressed as:

$$E_t = \frac{V/\varepsilon_2}{\frac{t}{\varepsilon_2} + \frac{d-t}{\varepsilon_1} + \frac{d_p}{\varepsilon_p}} \quad (1.10)$$

where ε_1 , ε_2 , and ε_p stand for the dielectric constant of liquid-1, liquid-2, and polymer layer, respectively; d is the cell gap, d_p is the thickness of polymer layer, and t is the height of liquid-2 from the polymer surface to the curved surface of the droplet along vertical direction. Some parameters are shown in Figure 1.13(b). In Eq. (1.10), the influence of d_p/ε_p to E_t is negligible if the polymer layer is very thin ($d_p \rightarrow 0$). In this case, the electric field E_t near the droplet border can be expressed as Eq.(1.11)

$$E_{t \rightarrow 0} = \frac{V\varepsilon_1}{d\varepsilon_2} \quad (1.11)$$

If the apex distance of the droplet is approaching the cell gap ($t \rightarrow d$), then the electric field E_t at the apex position of the droplet can be expressed as:

$$E_{t \rightarrow d} = \frac{V}{d} \quad (1.12)$$

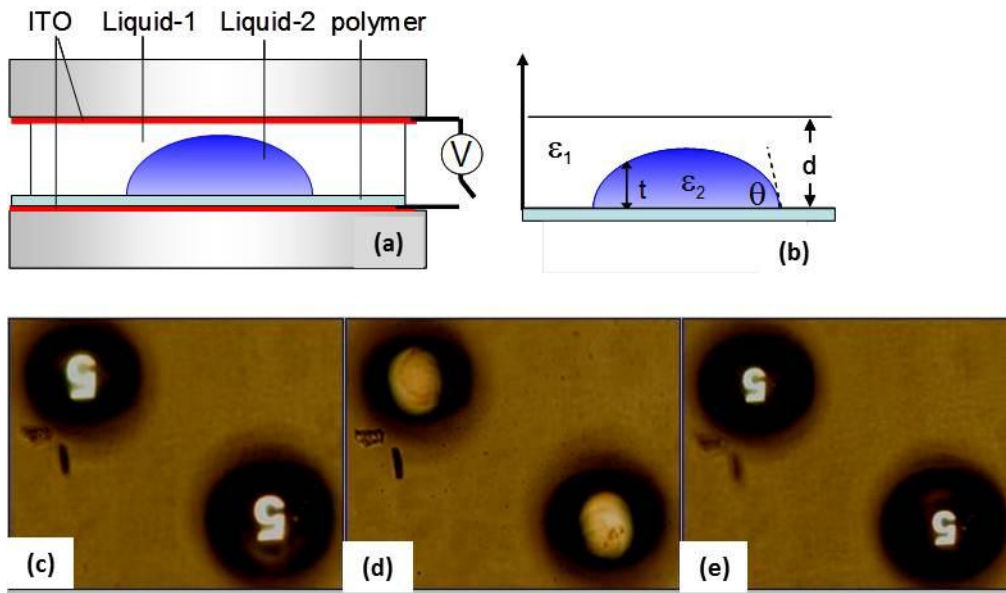


Figure 1.13: (a) Side-view structure of the lens cell, (b) Definition of the involved parameters and imaging properties of two liquid lenses at (c) $V=0$, (d) $V=60 \text{ V}_{\text{rms}}$, and (e) Refocused state.

From Eq. (1.11) and Eq.(1.12), the electric field at the border is $\varepsilon_1/\varepsilon_2$ times stronger than that at the apex position. Because the surface of the droplet changes continuously, the electric field has a gradient distribution. Therefore, the surface profile of the droplet can be reshaped by the generated dielectric force and the focal length can be tuned accordingly. A small letter “5” typed on a transparent film as an object was placed under the lens cell. By adjusting the cell position, a clear image of an inverted “5” in the voltage-off state was observed, as shown in

Figure 1.13(c). When the lens was actuated at $V = 60 V_{\text{rms}}$, the image became blurry instantly due to the defocusing effect, as shown in Figure 1.13(d). The image of a reduced size after refocusing is shown in Figure 1.13(e). The focal length of a lens with a 230- μm aperture diameter changes from $\sim 620 \mu\text{m}$ to $\sim 500 \mu\text{m}$ when the voltage increases to $90 V_{\text{rms}}$. The switching time (both contracting and relaxing) of the lens is $\sim 200 \text{ ms}$.

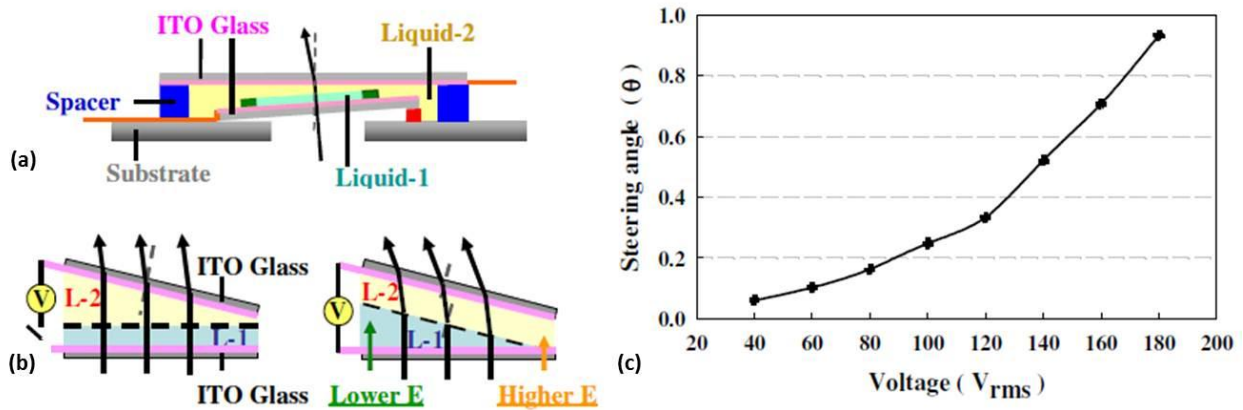


Figure 1.14: (a) Side-view of the (a) device structure, (b) the beam steering by the tilted liquid-liquid interface, and (c) experimental results of the He-Ne laser beam steering angle at various voltages.

The inhomogeneous electric fields can also be induced by two non-parallel ITO glasses. A broadband and polarization-independent beam steering has been demonstrated by Lin et al in 2009 [29]. The top ITO substrate is set slanted with an angle of 5° to the bottom ITO substrate to generate the nonuniform electric fields (Figure 1.14(a)). At $V=0$, the liquid-liquid interface is horizontal and the beam propagates straightly. When the voltage is high enough, L-2 with a larger dielectric constant moves toward the region with a higher electric field intensity and squeezes L-1 to the right (Figure 1.14(b)). As a result, the liquid-liquid interface becomes slanted and the beam is deflected. The measured steering angle of a He-Ne laser beam at various angle are shown in Figure 1.14(c). The maximum steering angle is $\sim 0.89^\circ$ at $V=160V_{\text{rms}}$. Two dimensional (2D) beam steering can also be achieved by stacking two devices in orthogonal

positions. Two technical challenges remain to be overcome: to keep a flat liquid-liquid interface at high operating voltages, and to reduce the operating voltage.

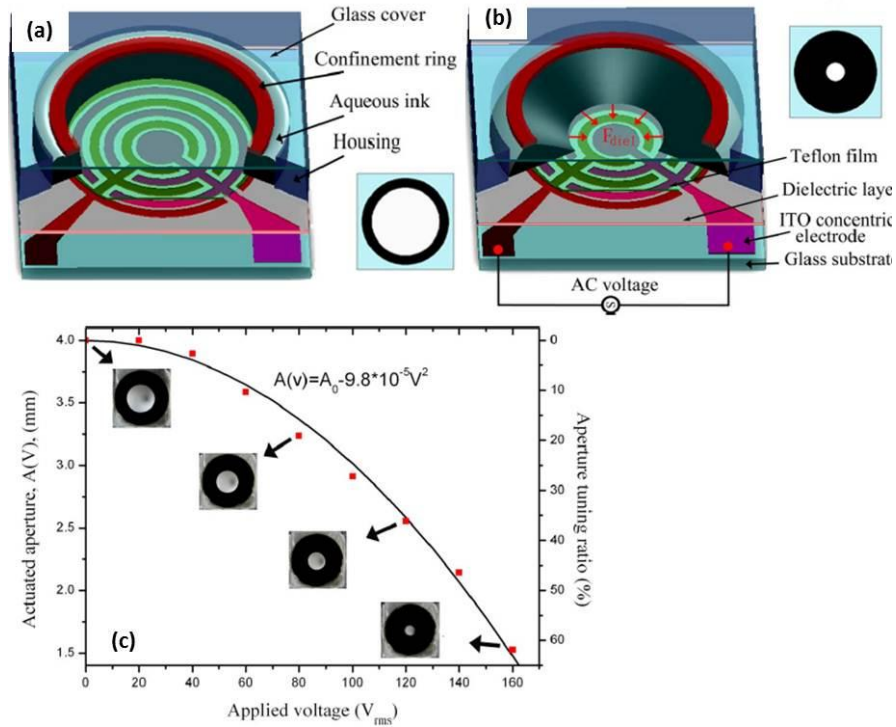


Figure 1.15: Dielectric liquid iris at (a) V-off state, (b) V-on state and (c) measured and fitted aperture $[A(V)]$ of the dielectric liquid iris at various voltages.

In 2010, Tsai et al. demonstrated a liquid iris diaphragm based on DEP effect [33]. As Figure 1.15(a) shows, it comprises four parts, including two immiscible liquids (a transparent oil and an opaque ink), an ITO electrode substrate, a glass cover, and a polymethylmethacrylate (PMMA) housing with a confinement ring. The liquids experience an angularly symmetric electric field induced by concentric annular electrodes, and the liquid-liquid interface suffers a dielectric force pointing to the center, pulling the opaque ink inward, as shown in Figure 1.15(b). Such a state is stable when the dielectric force and the interfacial tensions reach a balance. Hence, the aperture size can be electrically tuned. It varies from 4 mm at the rest state to 1.5 mm

at $160 V_{\text{rms}}$, as shown in Figure 1.15(c), and the corresponding aperture ratio is ~62%. However, the operating voltage is quite high, and the aperture at the limited state (1.5 mm at $160 V_{\text{rms}}$) is still quite large compared to traditional mechanical irises.

In this dissertation, several optical fluid-based photonic and display devices using the operation principles of fluidic pressure or DEP effect are demonstrated, and their electro-optic properties are studied. In the photonic devices based on fluidic pressure part, we propose a non-mechanical approach to actuate the membrane-encapsulated liquid lens, and demonstrate a novel mechanical-wetting lens for near IR applications as well as a concept which can extend the lens working range to mid and long IR. In the photonic devices based on DEP effect, we propose approaches to lower the operating voltage and widen the dynamic range of the dielectric liquid lenses by introducing various polymer bases to the bottom glass substrates. By either reconfiguring the shape of a dielectric liquid droplet or shifting its position, optical switches for visible and near IR spectral region are demonstrated. Besides lenses and optical switches, polarizer-free and color filter-free displays for mobile applications are also developed. These devices have the key features of simple fabrication, low power consumption, polarization independence, relatively low operating voltage as well as reasonably fast switching time, which make them promising for various applications. This dissertation has further extended the applications of DEP effect in photonic devices.

CHAPTER 2 ADAPTIVE LIQUID LENSES BASED ON FLUIDIC PRESSURE

In an adaptive lens based on fluidic pressure, the focal length is controlled by pumping liquid in and out of the lens chamber, which changes the curvature of the liquid profile. The operation mechanism is simple but a fluid pumping system is always needed [1-3,5-7], which brings a lot of inconvenience to portable devices. For the revised liquid lens [4], electromagnetic and piezoelectric actuator, servo motor actuator or artificial muscle can be used to squeeze the outer elastic membrane [51,80-82]. However, there remains a challenge to integrate the lens and the actuator into a compact system due to the bulky size of the actuator. Voice coil motor and shape memory alloys actuators have also been proposed for a compact lens system [55,83,84]. However, in some biological and medical applications, electrical controls or fluid circulation should be avoided and innovative mechanism to actuate membrane-encapsulated liquid lens is needed [85]. A tunable liquid microlens actuated by IR light is demonstrated in 2008, which makes it possible to integrate the microlens with fiber optics based systems such as fiber endoscopes [15]. This driving method is more favorable for micro-sized liquid lens.

2.1 Membrane-encapsulated Liquid Lens Actuated by Photo-controlled Polymer

In this chapter, we present a tunable liquid lens actuated by a photo-controlled polymer. The lens structure consists of a top glass substrate and a bottom plastic slab with two apertures. One aperture is called as reservoir hole and the other as lens hole, and both are sealed with elastic membranes. A photo-sensitive polymer is attached to the membrane of the reservoir hole and it will push the membrane inward once it is actuated by a blue laser beam. The bending

angle of the polymer, controlled by the power density of the blue light, regulates the curvature of the membrane on the lens hole which, in turn, changes the focal length of the plano-convex lens. The fabrication procedure is simple and the resultant liquid lens shows good stability. This actuation method can be adopted in a micro-sized, millimeter-sized or even larger size liquid lens. Compared with traditional methods, our lens offers a possibility to achieve a compact system, non-mechanical actuation, and easy integration with other optical components.

Polymer networks containing azobenzene liquid crystalline (azo LC) moieties are able to change their macroscopic shape when influenced by light. Several photo-polymers based on this mechanism have been reported [86-88]. The polymer film used in our experiment is made from 4, 4'-Di(6-acryloxyalkyloxy) azobenzene and LC monomer 4-(6-acryloxy)hexyloxy-4'-ethoxy-azobenzene [89]. The azo LC moieties need to be aligned before thermal polymerization, and this alignment is considered as the film alignment. Figure 2.1 shows the reorientation of azo LC molecules at different polarized incident light. The polymer film will bend away from the incident laser beam when the film alignment (\mathbf{n} , red arrow in Figure 2.1(a)) is *orthogonal* to the beam polarization (black cross in Figure 2.1(a)), and bow towards when the alignment (red arrow in Figure 2.1(b)) is *parallel* to the beam polarization (black arrow in Figure 2.1(b)). Because molecular reorientation shrinks (or expands) the polymer's volume locally along (or perpendicular) the polarization direction, the generated compression force is acting along the polarization direction. The film will maintain optically-induced shape when the incident beam is turned off. The bending angle increases with the laser power density once it is above a threshold. This reversible bi-directional bending of the polymer film can be controlled by switching the polarization of the actuation beam in orthogonal directions. Large bending angle ($-70^{\circ} \sim 70^{\circ}$) and fast bending speed (170 %/s) could be obtained by a fairly low power density ($\sim 0.1 \text{ W/cm}^2$) at

$\lambda=514 \text{ nm}$) [89]. These characteristics enable the photo-polymer to actuate the membrane-encapsulated liquid lens.

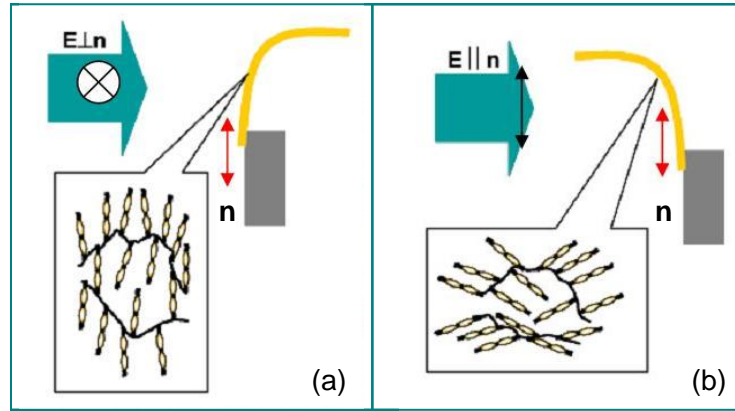


Figure 2.1: Schematic of experimental geometry and the effect of laser-induced LC reorientation: (a) Bending away from the laser beam when $E \perp n$, and (b) Bending towards when $E \parallel n$.

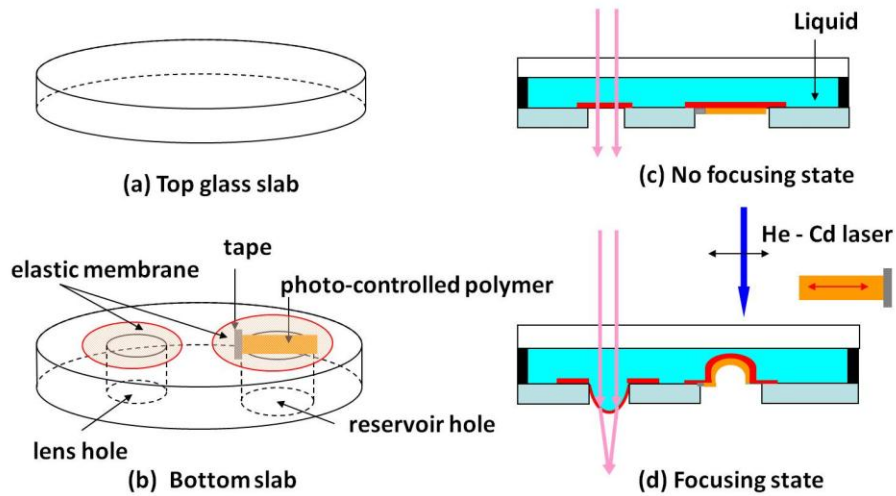


Figure 2.2: Structure of a tunable lens actuated by photo-polymer (a) Top glass slab, (b) Bottom glass slab, side view of the lens cell in (c) non-focusing and (d) focusing states.

Figure 2.2 shows the fabrication process of the liquid lens actuated by a photo-polymer. A top glass substrate and a bottom plastic slab with two holes are used as lens frames, as shown in Figure 2.2(a) and Figure 2.2(b). The right aperture is called as reservoir hole and left one as

lens hole. The two apertures are both sealed with elastic membranes. A piece of photo-polymer is fixed on the elastic membrane of the reservoir hole. The two slabs are sandwiched together and form a flat cell, and the periphery is sealed with epoxy glue except for a hole. A liquid is injected into the lens chamber through the hole, and after that, the hole is sealed with glue. Figure 2.2(c) shows the cross-sectional view of the lens cell in the non-focusing state. When the beam is polarized parallel to the film alignment direction with the power density above the threshold, the polymer film will bend towards the incident light and push the adhering elastic membrane on the reservoir hole inward. Because the volume of the liquid is not constrictive, the liquid in the lens chamber is redistributed, causing the elastic membrane on the lens hole to swell outward, as shown in Figure 2.2(d). A plano-convex lens is obtained and the incident light is focused. The focal length can be tuned by the power density of the actuation beam because the bending angle increases with power density. This tuning process is reversible, only if the beam polarization direction is rotated by 90° , which can be achieved by switching a twisted nematic (TN) LC cell [90].

To fabricate a liquid lens as shown in Figure 2.2(c), two holes were drilled on the bottom plastic slab, and both were sealed with PDMS membranes from inside. PDMS is a well-studied hydrophobic membrane and is transparent in ultraviolet-visible regions. Its super elastic and soft nature makes it easy for reversible deformations in fluid manipulations [91]. The diameters of the reservoir hole and the lens hole are 6 mm and 4 mm, respectively, and the thickness of the PDMS membrane is 60 μm . A piece of photo-polymer (2 mm x 4 mm x 20 μm) was one-end fixed on the outer surface of the PDMS membrane on the reservoir hole by tape, and the position of the polymer film is adjusted to make its alignment direction (red arrow in Figure 2.2(d)) parallel to the beam polarization direction (black arrow in Figure 2.2(d)). The two slabs were

sandwiched together to form a flat cell, and pure water ($n=1.33$) was injected into the cell. The thickness of the top slab and bottom slab is 3 cm and 1 cm, respectively.

To activate the liquid lens, a CW He-Cd laser ($\lambda=442$ nm) was employed as the actuation beam. Upon the incidence of this actuation beam, the film bends towards the incident laser beam because its alignment direction is parallel to the laser's polarization direction, as shown in Figure 2.3(a). The experimental set-up for the lens actuation is shown in Figure 2.3(b). Two solid lenses placed on the optical bench were used to focus the laser beam on the polymer film. The focal point of the two-lens system can be adjusted by changing the distance between the lenses. The liquid lens cell was placed out of the initial focus of the two lenses system and was adjusted to let the laser beam go through the polymer. Shortening the distance between the two solid lenses by moving lens 2, the focus of the two lenses system moved towards the polymer, accordingly the irradiance exposed on the polymer increased. Once the power density exceeded the threshold, the polymer began to bow towards the incident laser beam and the liquid lens began to focus.

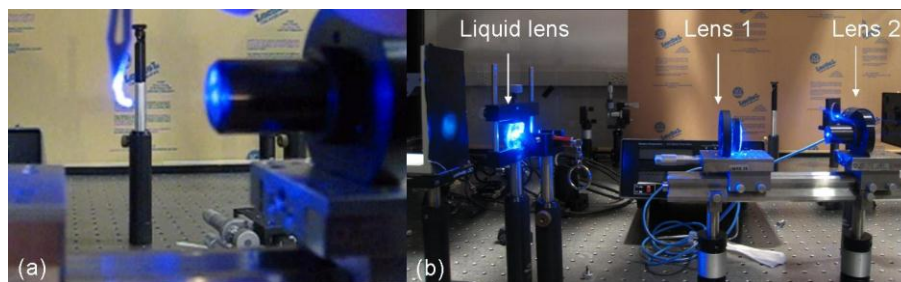


Figure 2.3: (a) Deformation of the photo-polymer under blue laser irradiation and (b) Experimental set-up for the actuation of the membrane-encapsulated liquid lens.

To evaluate the lens performance during the focus change, the image of an object through the liquid lens under the white light illumination was recorded. A picture, printed with two letters “do” was set at ~ 0.2 cm behind the lens, and a charge-coupled device (CCD) camera was used to record the images. The distance between the liquid lens and lens 1 is fixed at 19 cm. Figure 2.4

shows the photos taken at 2 different focusing states. Firstly, the laser was off and the liquid lens was in a non-focusing state so that the observed image had the same size as the object, as Figure 2.4(a) shows. An enlarged image is shown in the lower-left corner. Then we turned on the laser and focused it on the polymer film gradually. The initial separation between lens 1 and lens 2 was 14.5 cm. The power density was increased to 0.47 W/cm^2 when the separation between lens 2 and lens 1 was shortened to 12 cm. The focal length of the resultant plano-convex lens was decreased to 21.2 mm in ~ 10 seconds and the observed picture is shown in Figure 2.4(b). Since the distance between the object and the liquid lens is shorter than the focal length, the observed image is upright, virtual, and magnified.

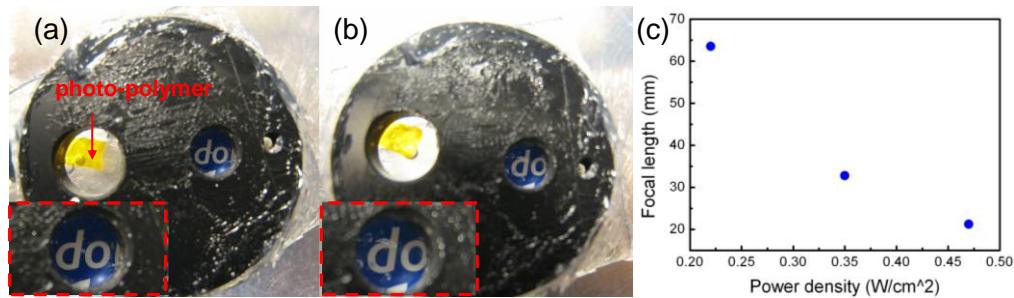


Figure 2.4: Liquid lens at (a) non-focusing state, (b) focusing state, and (c) Measured focal length of the lens at different power densities.

Figure 2.4(c) is a plot of the irradiance dependent focal length of the liquid lens shown in Figure 2.4(a). The focal length is determined by the smallest focused point of a collimated input light beam along the optical axis. In our experiment, a collimated white light was used as the probing light source. At the rest state, the lens cell is in flat state and its focus is at infinity. The focal length decreases with increasing power density for the polarization parallel to the alignment of the polymer film. As the power density increases, the polymer film deforms further

so that the PDMS membrane swells outward further and the radius of the curvature is reduced. The focal length is decreased to 21.2 mm when the power density reaches $\sim 0.47 \text{ W/cm}^2$.

From Figure 2.4, we can see that the photo-polymer can be used to actuate a membrane-encapsulated liquid lens. However, the detected focus change is not very large. Qualitatively speaking, to enhance the mechanical robustness of the liquid lens, we could take the following steps: 1) Using a larger and thicker polymer film, thus the bending force induced by the polymer deformation can be enhanced. 2) Applying an actuation beam with a high power density, hence a large bending angle can be obtained because the bending angle increases with the power density of the laser beam. 3) Selecting the wavelength of the actuation beam which can induce the largest deformation under the same irradiation. 4) Optimizing the lens structure and finding the best position for the polymer so that it can work more efficiently. The typical thickness of the photo-polymer is 10~50 μm [89], the sample used in our experiment is 20 μm thick. If the polymer thickness is increased to 50 μm and its size is large enough to cover the whole reservoir aperture, and meanwhile if the actuation beam with a sufficient power density can also cover the whole reservoir, then the mechanical robustness, the dynamic range, and the response time of the lens could be improved substantially.

To make a compact optical system for practical applications, the employed He-Cd laser can be replaced by a laser diode (LD), as shown in Figure 2.5(a). Because the bending direction of the photo-polymer is polarization sensitive, we use a 90° TN cell to switch the polarization of the laser beam. Let us assume the alignment direction of the polymer film (red arrow in Figure 2.5(a)) is along z axis, the polarization direction of the laser beam and the rubbing direction of the bottom glass substrate of the TN cell (Figure 2.5(b)) are parallel to each other, both along y axis. In the voltage-off state, the TN cell rotates the polarization of the incident laser beam by

90°, thus the polarization direction of the laser beam after passing through the TN cell becomes parallel to the film alignment. The polymer bows towards the laser beam and a plano-convex lens is obtained. The focal length decreases with increasing power density of the laser beam. In the voltage-on state, the polarization rotation effect of the TN cell vanishes, and the polarization of the laser beam stays along z axis. Therefore, the polymer bends away from the incident laser beam and the focusing power of the lens decreases. The focal length increases with increasing power density of the laser beam. The switching time of the TN cell depends on the LC cell gap and the material employed. For a typical 5- μm E7 TN cell, the response time is ~ 25 ms [92]. This switching time is much faster than that of photo-polymer (~ 170 %s) [89]. As a result, it has almost no influence on the response time of the liquid lens system. The deformation direction can be selected by the TN cell, and the deformation magnitude can be controlled by the laser power density, thus, both forward and backward actuations of the membrane-encapsulated liquid lens can be achieved.

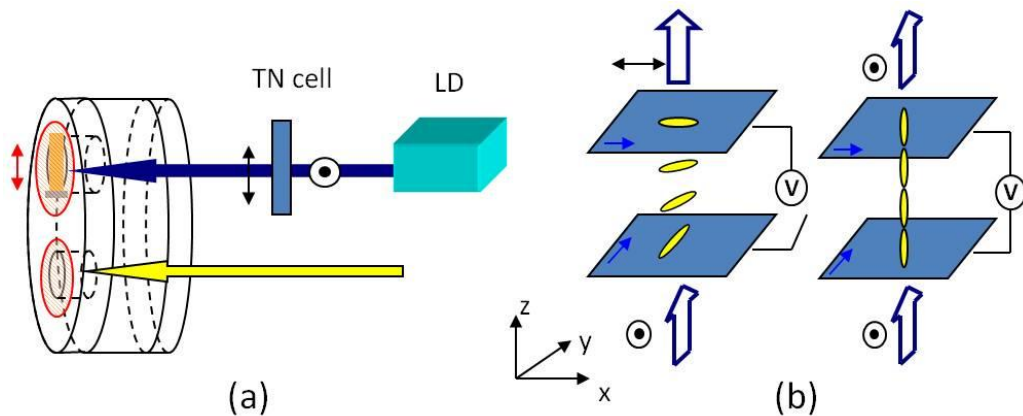


Figure 2.5: (a) Tunable liquid lens system, (b) Voltage-on state and -off state of a TN LC cell.

2.2 Adaptive Mechanical-wetting Lens for Visible and Near Infrared Imaging

In a typical membrane-encapsulated liquid lens based on fluidic pressure, PDMS membrane is commonly employed because of its super elasticity and good transmittance in visible and near IR region [93]. As we discussed in Chapter 1.2, the gravity effect may cause an asymmetric shape and degrade the image performances when the lens is vertically placed. Furthermore, neither the fabrication of a thin, strong, and uniform membrane nor the uniformly installing on the lens frame is a trivial.

Electro-wetting lens overcomes the abovementioned problems of a membrane-encapsulated liquid lens. It adopts an interface between two immiscible liquids as a reflective surface, which is very smooth (nanoscale) because of the surface tension. The two liquids are chosen to be density matched to minimize the density effect. Therefore, electro-wetting lens is insensitive to shocks and vibrations [18]. However, electrolysis, Joule heating, and microbubbles often occur in electro-wetting lenses due to the transportation of the free electric charges and the alternating electric fields [26].

We demonstrate an adaptive mechanical-wetting lens to keep the advantages of smooth liquid-liquid interface and minimum gravity effect while overcoming the shortcomings of an electric-wetting lens. Our lens uses liquid pressure to change the interface between two immiscible liquids, which in turn changes the focal length of the resultant liquid lens. We call this device as mechanical-wetting lens because it involves two liquids in a lens cell, similar to that in an electro-wetting lens, while the liquid-liquid interface is changed by a mechanical force. In comparison with the design whose reservoir is on one side of the lens area [54], our new design pumps liquid uniformly through the entire periphery of the lens area because of the

concentric reservoir. It eliminates the gradient effect in liquid pressure and stabilizes the optical performance during the transition process. Furthermore, since no PDMS is employed, our lens can expand its working range to IR. To prove concept, we show the performance of our lens at $\lambda=1310$ nm.

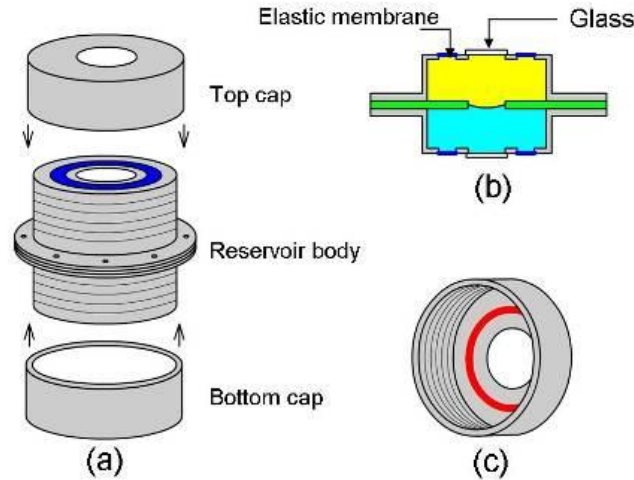


Figure 2.6: Device structure of a mechanical-wetting lens: (a) Assembled system, (b) Side-view of the reservoir body, and (c) Cap with a bump inside.

Figure 2.6 shows the device structure of the mechanical-wetting lens. From top to bottom, the lens frames consist of a top cap, a reservoir body, and a bottom cap, as shown in Figure 2.6(a). There are two holes in the reservoir body. An observation hole covered by glass is in the center of the reservoir body, and a ring-shaped hole covered by elastic membrane (marked in blue) is concentric with the observation hole, they are connected with each other through tiny linkages. Two immiscible liquids interface at an aperture hole in the middle circular slab (marked in green), as shown in Figure 2.6(b). The top and bottom caps are the driving devices to press the membrane. Each cap is a cylindrical shell with one end open and the other end closed, as shown in Figure 2.6(c), and a hole is drilled in the closed end for observation. The screw

threads on the inside wall of each cap match those on the outside wall of the reservoir body. Thus when the cap is screwed toward the reservoir body, the bump in the cover (marked in red) will press the elastic membrane, causing the liquid-liquid interface to bend.

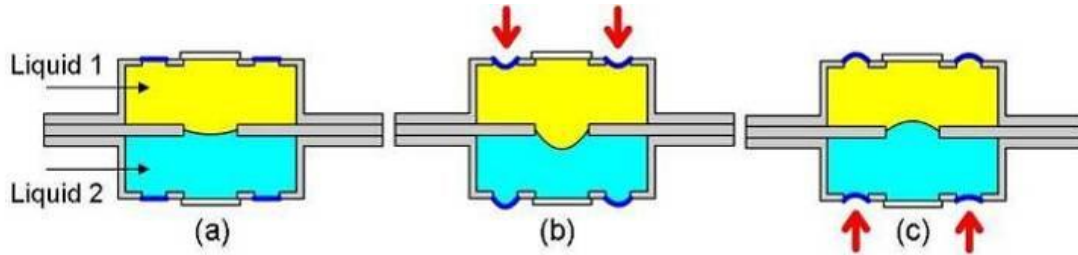


Figure 2.7: Side view of a mechanical-wetting lens structure in (a) Initial state, (b) Further positive state, and (c) Negative state.

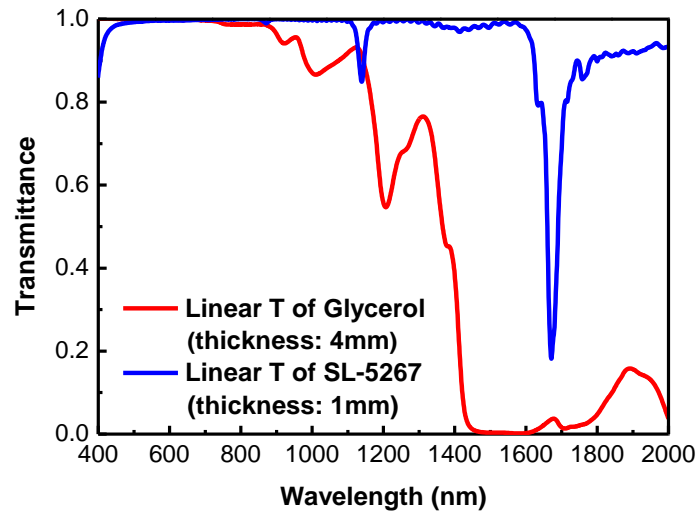


Figure 2.8: Transmission spectra of SL-5267 and Glycerol measured from 400 nm to 2000 nm.

Figure 2.7 shows the cross-sectional view of the reservoir body in different driving states. At the initial state, assuming the top and bottom elastic membranes are both flat, liquid-2 forms a concave shape at the aperture hole in the middle layer because of the surface tension, as Figure 2.7(a) shows. The liquid lens behaves as a positive lens if the refractive index of liquid-1 is larger than that of liquid-2. When an external pressure is applied to the top elastic membrane,

because the volume of the liquids are not constricting, liquid-1 in the lens chamber is redistributed, pressing the interface to change its shape to further concave, as shown in Figure 2.7(b), and the optical power of the resultant lens goes further positive. If an external pressure is applied to the bottom elastic membrane, liquid-2 in the lens chamber is redistributed, pressing the interface to change its shape from concave to convex with an increasing external pressure, as shown in Figure 2.7(c), accordingly the optical power of the resultant lens changes from positive to negative.

The two liquid employed in Ref.[54] are ultrapure water ($n_1=1.33$) and PDMS gel ($n_2=1.40$), the refractive indices difference is small and the water is easy to evaporate, causing a short device lifetime. To overcome these drawbacks, Glycerol and SantoLight™ Optical Fluids SL-5267 are used, and their properties are shown in Table 2.1. These two immiscible liquids have similar density to minimize the gravity effect and a large refractive index difference. They also show good transmittance in both visible and near IR regions, which enables our lens to work in near IR. Figure 2.8 shows the measured transmission spectra of these two liquids. The dramatic drop in the transmission spectra of SL-5267 near 1650nm is due to the overtone (second harmonic) of CH/CH₂/CH₃ stretching bands, which occurs at 3.3-3.6 μm . Thus, its second harmonic occurs at $\sim 1.7 \mu\text{m}$ [94].

Table 2.1: Properties of liquid-1 (L1: SantoLight™ Optical Fluids SL-5267, Santovac® Fluids) and liquid-2 (L2: Glycerol, Sigma-Aldrich).

Material	Surface tension (mN/m, @20 °C)	Refractive index	Density (g/cm ³)	Color
L1	50	1.670@550nm 1.635@1310nm	1.25	Clear
L2	64	1.47@550nm 1.460@1293nm	1.26	Clear

While making a lens described in Ref. [54] using Optical Fluids SL-5267 and Glycerol, we found this design could keep a uniform liquid-liquid interface only if the transition time was slow (a few tens of seconds). If the transition time was reduced to a few seconds, then the liquid interface change was no longer uniform and a severe image aberration appeared during the transition process. The aberration became even worse as the aperture increased. The reason is explained as follows: when actuated in high speed, the pressure increases quickly so that a pressure gradient builds up from the reservoir area to the lens area. As a result, the liquid interface first bends on the high pressure end (near the reservoir) and then propagates to the other end. This gradient effect not only induces image aberration during the transition process, but also creates high stress on one end of the interface, resulting an interface movement and device instability. This problem originates from the high viscosity of Glycerol. Our solution is to make a lens with a concentric reservoir, as depicted in Figure 2.6. Thus, the pressure gradient will be significantly suppressed, because the pressure along the entire periphery of the liquid-liquid interface is almost the same.

The lens frames were made of aluminum. The two chambers in the reservoir body and the middle slab were connected with each other by screws and sealed by silicon glue to prevent fluid leakage. Then, two liquids were filled into each chamber, the upper chamber was filled by Optical Fluids, and the lower was Glycerol. The amount of each filled liquid was well controlled so that their interface stayed at the aperture hole of the middle layer. Some lubricate was added to the outer surface of the elastic membranes in order to reduce the friction when the caps were pressing the membranes. Coaxial design is desired in order to maintain optical functions of a liquid lens [31]. When the parts are machined on the lathe, they are all aligned to the same axis. Six screws holes are drilled in the reservoir body and the central layer respectively, and screws

are applied to connect and align these parts precisely. The diameter of the observation hole and aperture hole is 5 mm and 4 mm, respectively. The inner and outer diameter of the ring-shaped hole covered by elastic membrane is 20 mm and 28 mm, respectively. The middle slab is ~1 mm thick, the rubber bump is ~2 mm thick and each liquid layer is ~ 4 mm thick. The total thickness of the whole device is ~15 mm, and it can be further reduced if thinner frames are used. The screw pitch is 1/32 inch, which means the bump goes towards the reservoir body 1/32 inch when the cap is rotated in one full circle. The lens was tested in the visible region and near IR region.

To evaluate the lens performances during transition process, we recorded the image of an object through the liquid lens under white light. A picture, printed “5” was set very close to the lens, and a CCD camera was used to record the image change. Figure 2.9 shows the images taken through the lens at three different focusing states corresponding to those in Figure 2.7. Firstly, the lens was in the initial state with a positive optical power and the observed image was upright, virtual, and magnified, as shown in Figure 2.9(a), because the distance between the object and the lens cell was shorter than the focal length. When the top cap was screwed towards the reservoir body, the rubber bump touched the elastic membrane on the top chamber and pushed it to go deeper with an increasing traveling distance, and consequently the resultant lens became further positive and the image size was further magnified, as shown in Figure 2.9(b). The resultant liquid lens began to exhibit less positive and then negative optical power when the bottom cap was screwed toward the reservoir body with an increasing traveling distance, and the observed image was reduced, as shown in Figure 2.9(c). The image changed continuously and uniformly during the top cap’s traveling, and no obvious aberration was observed. A tiny image aberration was observed at the border of the aperture, because the aperture was not perfectly circular, and the defects in the circumference of the aperture hole introduced the image

aberration. If the middle slab and the aperture hole can be made in high precision, e.g., fabricated by photolithography, a much smaller wavefront error will arise in the lens border [54]. The lens' resolution was also measured by the microscope. Figure 2.9(d) shows the image of a 1951 U.S. Air Force (USAF) resolution target taken in the transmission mode of the microscope under green illumination. The highest resolution of the device is ~ 203 lp/mm as the patterns of group 7 number 5 are still resolvable.

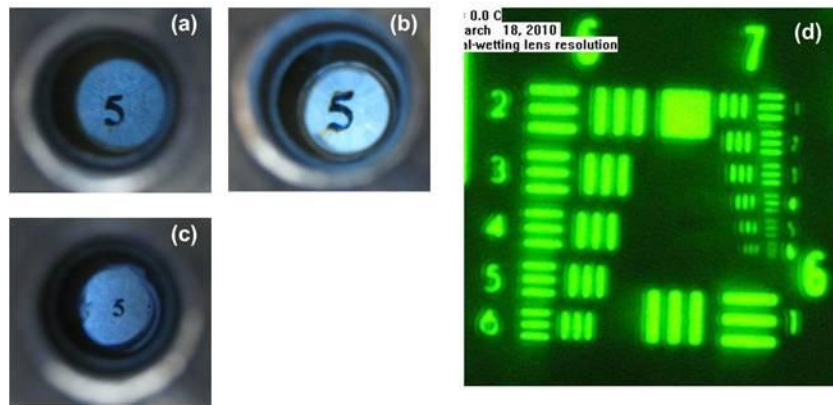


Figure 2.9: Images taken through the lens in (a) Initial state, (b) Further positive state, (c) Negative state, and (d) Len's resolution at the initial state.

To measure the back focal distance (BFD) of the liquid lens, we expanded and collimated a He-Ne laser beam ($\lambda=633$ nm) to ~ 10 mm in diameter and let it normally pass through the liquid lens. For the positive lens, the focal point was determined by the smallest focused point (a quite circular point with a diameter of ~ 1 mm) of the collimated input beam along the optic axis, as shown in Figure 2.10(a). For the negative lens, BFD was determined by a geometrical imaging method, as Figure 2.10(b) shows. Every measurement was repeated three times and the results were averaged. When the bottom cap is moving towards the reservoir body, the traveling distance dependent BFD is depicted in Figure 2.10(c), here P (1/32 inch) stands for the screw pitch.

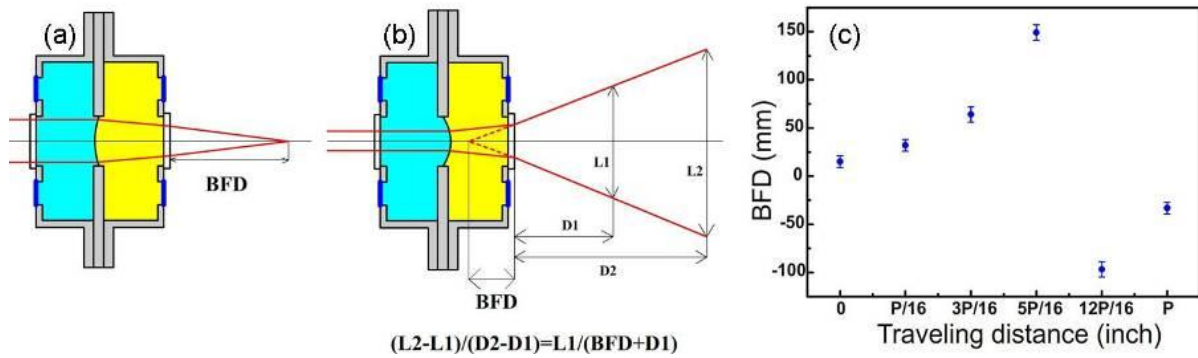


Figure 2.10: (a) BFD measurement of the positive lens, (b) BFD measurement of the negative lens, and (c) Measured BFD vs. traveling distance of the bottom cap.

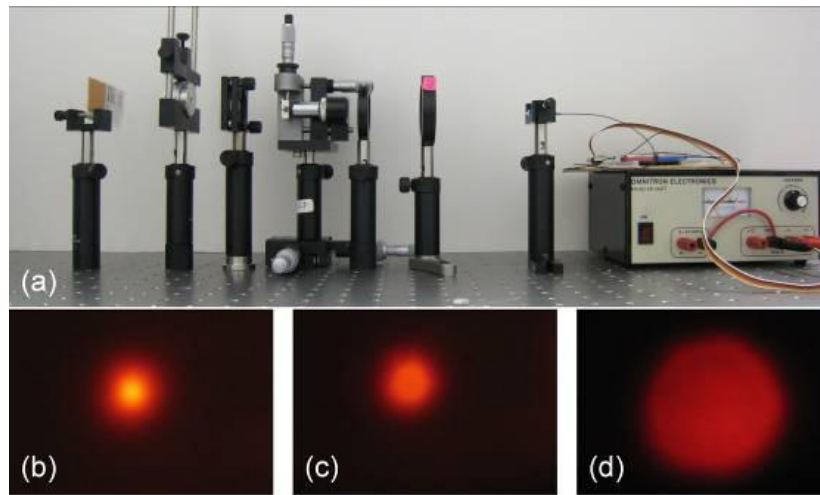


Figure 2.11: (a) Experimental set-up for lens testing under $\lambda=1310\text{nm}$ laser illumination, Light spots taken in (b) initial state, (c) less positive state, and (d) negative state.

The lens' ability and performance for near IR imaging are also evaluated. The experimental set-up is shown in Figure 2.11(a). An IR fiber laser ($\lambda=1300\text{ nm}$) was collimated and then illuminated the mechanical-wetting lens. A fluorescent card was used as a screen for observation. The lens was set vertically and some light spot images were recorded. The screen was set at the focus of the testing lens in the initial state, at first, a tiny and bright spot was observed due to the lens' initial positive optical power, as shown in Figure 2.11(b), when the

bottom cap was screwed toward the reservoir body, the lens first went less positive, then flat and finally negative. Thus the light spot was gradually increased, as shown in Figure 2.11(c)-(d). The spot is quite circular, and the light is highly centrally focused without any obvious noise when observed in the dark background. Due to absorption of Glycerol, the total lens transmittance is estimated to be ~60% under 1310 nm illumination.

Our simple mechanical-wetting lens is working well in visible and near IR regions. It paves a way to fabricate an adaptive liquid lens for mid-IR, long-IR or even UV imaging, by choosing proper liquids with good transmittance in the desired spectral region. Besides, some other criteria should be taken into consideration, e.g., density matching, large refractive indices difference, immiscibility, non-volatility, and stability. A matched density helps to minimize the gravity effect and realize highly axis-symmetric liquid droplet, especially for large aperture lenses. Large refractive index difference could enhance the optical power, while the non-volatility and good stability are crucial for lengthening the device lifetime. Furthermore, surface treatment can be applied to the middle slab, e.g., hydrophobic-hydrophilic bond, helps to confine the position of the liquids interface on the aperture hole [16], and other surface treatment may help to control the shape of the interface. If a parabolic shape could be obtained, the lens' spherical aberration could be reduced [95]. The tuning step is determined by the screw pitch on the outside wall of the reservoir body and inside wall of the caps. Thus, a smaller screw pitch would be favored for finer tuning. The present structure is favorable for self-adjustment in vision applications; for those applications in need of automatic driving and fast response, a mechanical motor can be adopted.

2.3 Summary

In this chapter, we have demonstrated a membrane-encapsulated liquid lens actuated by a photo-controlled polymer. Benefiting from the photo-induced deformation, the bending direction and bending angle of the polymer, and the resultant liquid lens can be tuned by a laser beam. The focal length can be tuned from infinity to 21.2 mm in seconds under blue light irradiation. This approach paves a way to achieve non-mechanical driving, easy integration with other optical components and compactness. The mechanical robustness, dynamic range, and response time of the liquid lens can be enhanced using a larger and thicker polymer film and an actuation beam with a higher power density.

To minimize the gravity effect of a membrane-encapsulated liquid lens and extend the working range to IR, we have demonstrated an adaptive mechanical-wetting lens with high optical performance. Due to the concentric reservoir structure and smooth liquid-liquid interface, the lens' transition process is smooth, and the optical performance is quite good and stable. When the bottom cap is traveling in one full circle, the back focal distance can be changed from infinity to ~15 mm and from -33.3 mm to infinity under 633 nm illumination, both positive and negative optical power can be obtained. Under 1310 nm illumination, the lens shows a ~60% transmittance and tunable light spots with circular shape could be observed. Fine processing and surface treatment could further improve the lens' performances. The same device concept can be extended to mid-IR and long-IR, provided that proper transparent liquids are employed. Moreover, our group has demonstrated a mechanical-wetting lens driven by ferrofluids [96]. The ferrofluids functions like a piston with much smaller friction than traditional ones. It pumps

liquids in and out from the lens chamber, reshapes the lens curvature and changes the focal length. Fast response (~ 2.5 ms) and automate driving have been achieved.

CHAPTER 3 DIELECTRIC LIQUID LENSES

3.1 Dielectric Liquid Microlens with Well-shaped Electrode

In a dielectric lens, under an inhomogeneous electric field, the generated dielectric force deforms the liquid-liquid interface, which in turn changes the focal length. However, a patterned-electrode is always required to generate such an inhomogeneous electric field, which adds complexity to the fabrication process [26,27]. A non-mechanical method to form uniform liquid droplet arrays was demonstrated, but the droplets could drift in the lens cell, which degrades the lens' stability [27]. Such a problem also exists in dielectric lens with continuous electrodes [28]. For a dielectric lens with a 230 μm aperture and 110 μm cell gap (two liquids with $\epsilon_1 \sim 47$ and $\epsilon_2 \sim 5$), the focal length changes from $\sim 620 \mu\text{m}$ to $\sim 500 \mu\text{m}$ when the driving voltage increases from 0 to 90 V_{rms} . The optical zoom ratio is ~ 1.24 [28]. We demonstrated an adaptive-focus dielectric microlens with a top planar electrode and a bottom well-shaped electrode to overcome these problems.

Figure 3.1 shows the side-view structure of the microlens cell with well-shaped electrode. From top to bottom, it consists of a planar glass substrate with ITO electrode, liquid-1(L1), liquid-2(L2), and a well-shaped polymer base Norland Optical Adhesive 81 (NOA81) with gold and palladium electrode and a planar glass substrate. L2 (SL-5267) with a low dielectric constant forms a bi-convex droplet on the well-shaped polymer base, while L1 (Glycerol) with a high dielectric constant fills the surrounding space. We choose these two immiscible liquids with similar density in order to minimize the gravity effect. The properties of the two liquids and the polymer well are listed in Table 3.1.

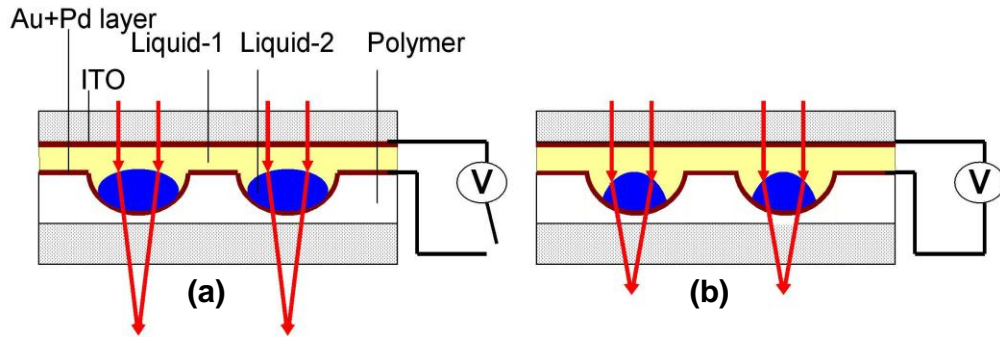


Figure 3.1: Side-view structure of the lens cell: (a) Voltage off, and (b) Voltage on.

Table 3.1: Properties of liquid-1 (L1: Glycerol, Sigma-Aldrich), liquid-2 (L2: SantoLight™ Optical Fluids SL-5267, Santovac® Fluids) and polymer wall (NOA81).

Material	Dielectric constant	Refractive index	Density (g/cm ³)	Color
L1	47	1.47	1.26	Clear
L2	5	1.67	1.25	Clear
Polymer wall	4	1.56	1.2	Clear

Figure 3.2 shows the device fabrication procedure. NOA 81 was injected into a glass cell, which was composed of a bottom glass substrate and a glass-based plano-convex microlens array stamper ($R=1$ mm, $\varnothing=0.75$ mm, 6×6 , from ISUZU GLASS) (Figure 3.2(a)). After UV exposure, the stamper was peeled off and the solidified concave microlens pattern was left on the bottom glass substrate (Figure 3.2(b)). A conducting layer consisting of a mixture of gold and palladium was deposited on the concave microlens as the bottom electrode using a sputter coater (Figure 3.2(c)). Finally, after dropping liquid-2 and liquid-1, a planar glass with ITO was used as top substrate to seal the cell (Figure 3.2(d)). The cell gap is ~ 270 μm . The total transmission of the lens is $\sim 50\%$ at $\lambda=550$ nm. Most of this loss originates from absorption of the metal electrode

and from interface reflections. This can be improved by optimizing the materials and thickness of the bottom electrode and by depositing substrates with anti-reflection coatings.

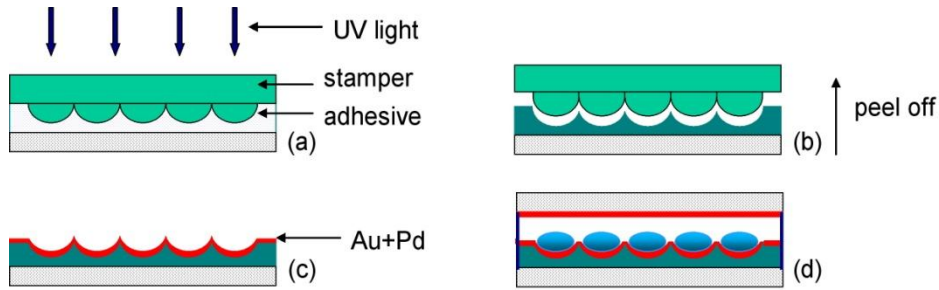


Figure 3.2: Side view of the device fabrication procedure: (a) Making lens cell and UV exposure, (b) Peeling off the stamper, (c) Coating Au +Pd electrode, and (d) Dropping liquids and sealing the cell.

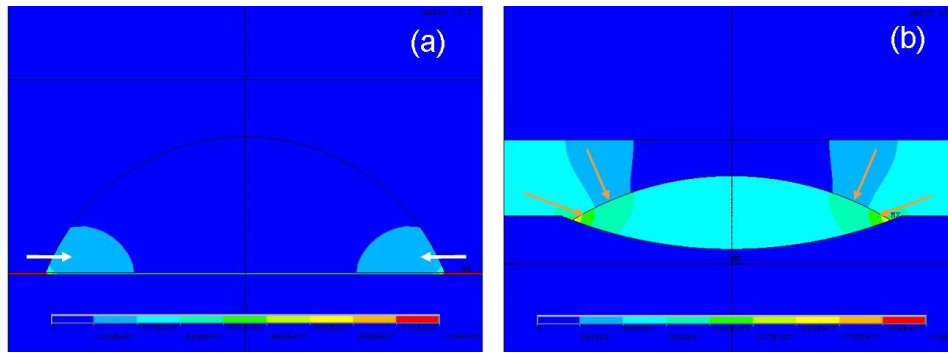


Figure 3.3: Simulation results of the electric field of the two structures at $V=100V_{\text{rms}}$ (a) Common planar-electrodes, and (b) Top planar-electrode and bottom well-shaped electrode.

In the relaxed state, the curvature of the droplet is minimal. In a voltage-on state, the bi-convex liquid droplet will induce an inhomogeneous electric field. According to Kelvin theory, the dielectric force exerted on the droplet can be expressed as Eq.(3.1) [70]

$$\vec{F} = \frac{\epsilon_0}{2} (\epsilon_1 - \epsilon_2) \nabla (E \cdot E) \quad (3.1)$$

where ϵ_0 , ϵ_1 and ϵ_2 donate the permittivity of free space, liquid-1, and liquid-2, respectively, and E denotes the electric field on the curved droplet surface. From Eq. (3.1), the difference between ϵ_1 and ϵ_2 and the gradient of the electric field play key roles on the dielectric force. When the

dielectric force is strong enough, L1 and L2 will move toward the region with strong and weak electric fields, respectively. The droplet tends to contract and the surface profile of the droplet is reshaped. As a result, the focal length becomes shorter, as shown in Figure 3.1(b).

In a common planar-electrode structure, the dielectric force is induced only from the shape of the droplet. By contrast, the well-shaped electrode structure introduces non-uniform electric fields from both the non-planar electrodes and the bi-convex shape of the droplet, resulting in an enhanced electric field gradient. The gap between the two electrodes is also reduced because the bottom electrode is deposited on the well surface not on the glass substrate. Computer simulations are also conducted to investigate and compare the dielectrophoresis in these two structures with an operating voltage of $100 V_{\text{rms}}$, and the results are shown in Figure 3.3, where the colors represent the electric field strength. According to Eq. (3.1), a larger electric field gradient induces a larger dielectric force. In a common planar-electrode structure shown in Figure 3.3(a), both liquids experience a similar electric field as indicated by the dark blue color. The electric field gradient could only be found along the interface between two liquids near the bottom planar electrode, which only represents $\sim 1/4$ of the arc of droplet. The white arrows denote the dielectric force acting on the droplet. However, in a well-shaped electrode structure shown in Figure 3.3(b), the color difference along the entire interface between the two liquids indicates that an electric field gradient exists in more than $1/3$ of the arc. A much larger surface is thus affected by the dielectrophoresis, and the generated electric force is indicated by the orange arrows in Figure 3.3(b). The downward force acting at the apex of the droplet would weaken the droplet deformation, but it is relatively small. Because of the enhanced non-uniform electric field gradient, the stronger electric fields originating from the closer electrode gap, and the larger affected surface, the operating voltage of the lens with well-shaped electrode will be

lower than that of the lens with common planar-electrodes having the same aperture and cell gap dimensions.

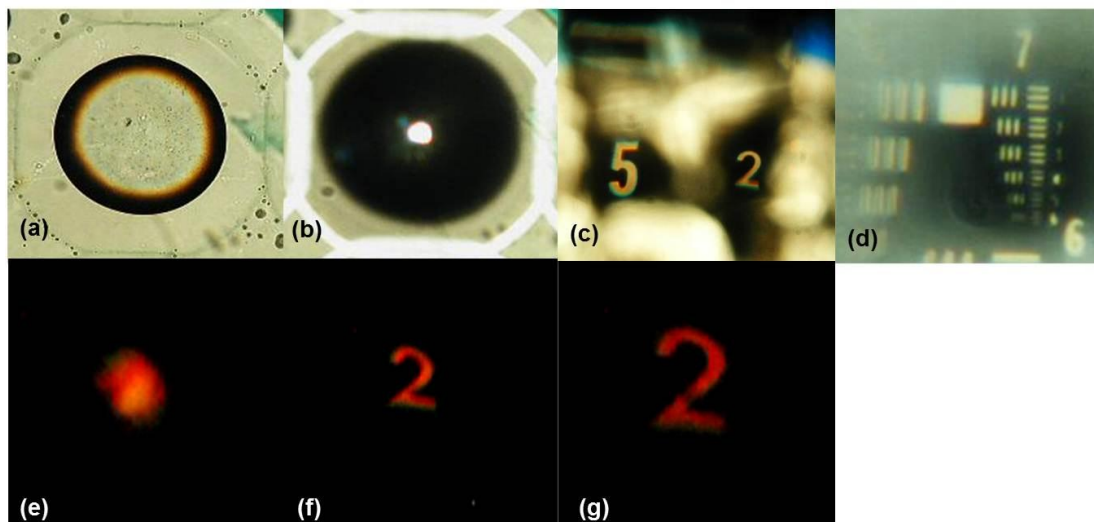


Figure 3.4: (a) The image of the lens cell at the position of surface focus, (b) At the position of the smallest spot size, (c) Image at focus, (d) Resolution test, (e) Tunable state of the lens at $V=0$, (f) $V=40$ V_{rms} , and (g) $V=88$ V_{rms} .

The performance of the microlens is also evaluated through an optical microscope. At $V=0$, the droplet's surface (diameter ~ 700 μm) is focused and the image is shown in Figure 3.4(a). The position of the lens cell is adjusted to achieve the minimum focus spot, shown in Figure 3.4(b). An image of the number "2" was captured as shown in Figure 3.4(c). Minor scattering is observed, though, due to slight nonuniformity of the well-shaped electrode, which is induced by the relatively slow stage rotation speed of the sputter coater. The optic axis of the liquid lens could be slightly deviated from its normal because of the nonuniform surface of the bottom well-shaped electrode, which induces a non-spherical profile in a voltage-on state. Figure 3.4(d) shows the image of a 1951 USAF resolution target taken in the transmission mode by the microscope. The highest resolution of the device is ~ 181 lp/mm as the patterns of group 7

number 4 are still resolvable. To visually observe the tunable state with different operating voltages, three pictures for tuning the above microlens were taken, as shown in Figure 3.4(e-g). A small number “2” on the USAF resolution target chosen as an object was placed under the lens cell. At $V=0$, the droplet was in a defocused state and the image was very blurry (Figure 3.4(e)). When the lens was actuated at $40V_{\text{rms}}$ a small inverted image “2” began to appear (Figure 3.4(f)). The image kept zooming in as we gradually increased the driving voltage to $V_{\text{max}}=88V_{\text{rms}}$ (Figure 3.4(g)). This indicates that the focal length of the droplet is electrically tunable.

The voltage dependent focal length of the dielectric lens shown in Figure 3.4(a) is plotted in Figure 3.5(a) as blue dots. At $V=0$, the initial focal length of the microlens is ~ 2.50 mm. As the voltage increases, the focal length gradually decreases. At $V=88 V_{\text{rms}}$, it is decreased to ~ 1.39 mm. Compared to the previous dielectric lens, the present dielectric lens with well-shaped electrode achieves a 1.8X optical zoom under the same voltage, with a $\sim 3X$ larger aperture and cell gap. The operating voltage can be dramatically reduced if the aperture and cell gap of the lens become smaller. Because the lens aperture is small and its shape is nearly spherical, we use ZEMAX to calculate the theoretical focal length. Only the well-shaped polymer base, liquid-1 and liquid-2 are considered. The lens structure and parameters used for the ZEMAX simulation are shown in Figure 3.5(b), where n_1 , n_2 , and n_p donate the refractive index of liquid-1, liquid-2, and well-shaped polymer base, respectively, D is the initial diameter of the lens, d is the cell gap of lens cell, and t_p is the apex distance of the polymer base. R_1 is the curvature radius of the well-shaped base, which is equal to that of the plano-convex microlens array stamper, because this base is replicated from the stamper. R_2 is the curvature radius of the top lens surface, t is the apex distance of the lens. Both R_2 and t vary with the operating voltage. In the relaxed state, we measured the apex distance $t \sim 0.163$ mm, so the calculated focal length is ~ 2.45 mm, which is in

good agreement with the measured focal length (2.50 mm). Meanwhile, the largest apex distance t is ~ 0.237 mm since the measured $t_p \sim 0.032$ mm and $d \sim 0.270$ mm. The sum of t and t_p should be smaller than d . Otherwise the droplet will touch the top glass substrate. The calculated focal length at this limiting state is ~ 1.25 mm, which is slightly shorter than the measured data (~ 1.39 mm) at $V = 88 V_{\text{rms}}$. This small difference could result from the fact that the microlens is not driven to its limiting state in our experiment.

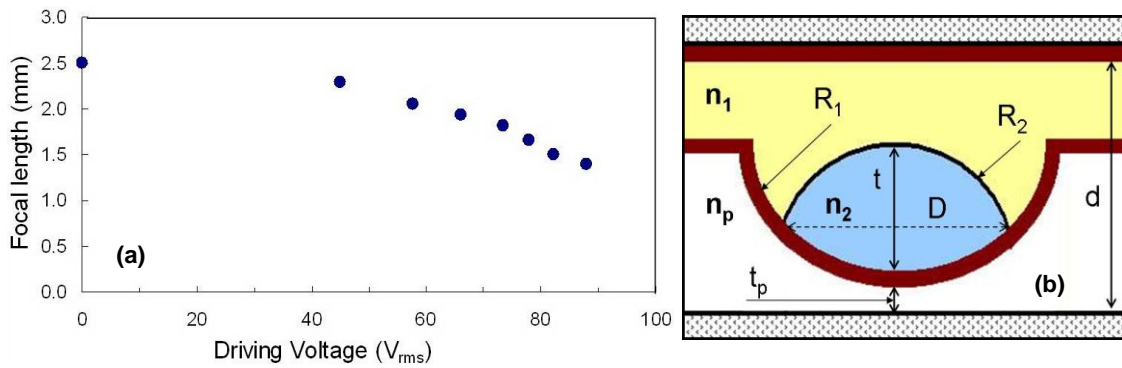


Figure 3.5: (a) Measured focal length of the microlens at different driving voltages, and (b) Lens structure and parameters for ZEMAX simulation.

A 3×3 microlens array is also demonstrated. The imaging properties of the microlens array are shown in Figure 3.6(a). Due to differences in the shape and diameter of the microlenses in the array, they are slightly different in focal length. The uniformity of the microlens array will be greatly improved if the liquid droplets are prepared by machine rather than by hand. Two pictures for tuning the array at $V=0$ and $V=88V_{\text{rms}}$ were taken, shown in Figure 3.6(b-c). The contracting speed of the microlens array is fast, but the relaxing speed is a bit slow as it depends on the viscosity of the liquids and the interfacial tensions [28]. The viscosity of the surrounding liquid-1 is ~ 1.5 Pas, introducing a large hysteresis when the voltage is switched off. The relaxing time can be shortened if we use some low viscosity liquids.

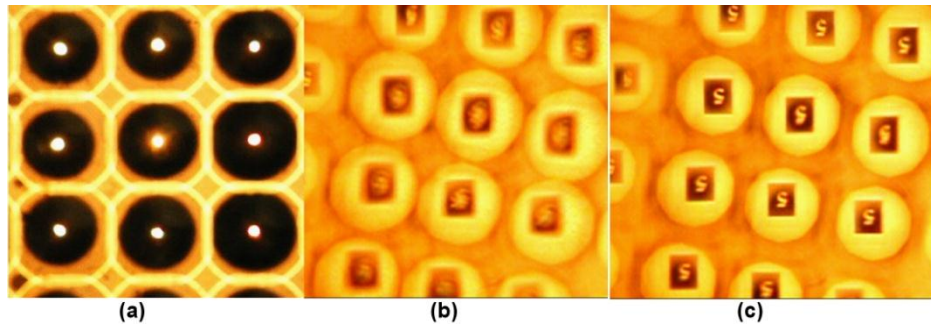


Figure 3.6: (a) Imaging properties of the microlens array, and (b) Microlens array at $V=0$ (c) Tunable state of the lens driven at $88V_{\text{rms}}$.

3.2 Dielectric Liquid Microlens with Switchable Negative and Positive Optical Power

The previously demonstrated dielectric lenses only shows pure positive or negative optical power [26-28,32]. It would be highly desirable to have a dielectric liquid lens which can be tuned from positive to negative or vice versa. Such an adaptive lens can be integrated into a zoom lens system for obtaining a large magnification or in a 2D-3D switchable display [97]. In 2009, we demonstrated a dielectric liquid microlens with a bi-concave polymer base. The negative optical power induced by the bi-concave polymer base balances out the positive optical power of the liquid droplet to some extent, according to different operating voltage. Hence, our lens can be continuously tuned among negative, zero and positive optical power states. Besides, the bi-concave polymer base helps to fix the position of the liquid droplet and reduce the operating voltage.

Figure 3.7 shows the side-view structure of the proposed microlens cell. From top to bottom, it consists of a planar glass substrate with ITO electrode, liquid-1 (Glycerol), liquid-2 (SL-5267), a bi-concave polymer base (NOA81) with gold and palladium electrode on the top surface, and a bottom glass substrate. The properties of the two employed liquids and polymer

base are listed in Table 3.1. The structure is very similar to that of the dielectric liquid microlens with well-shaped electrode in Chapter 3.1; the only difference is the shape of the polymer base.

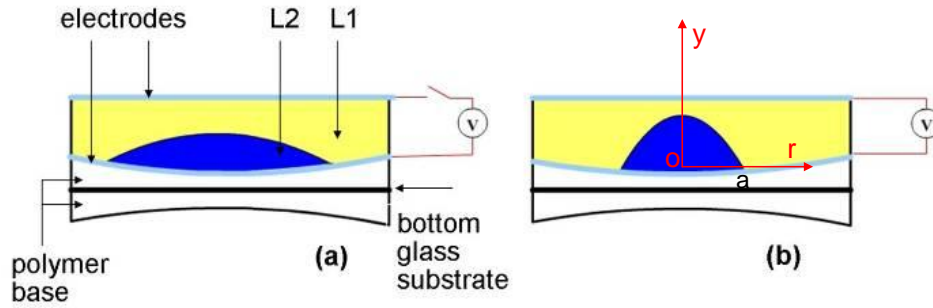


Figure 3.7: Side-view structure of the lens cell at (a) voltage-off state, and (b) voltage-on state.

Because of the surface tension force of the droplet liquid, the shape of the droplet is curved and its surface is very smooth. Like a deformed elastic membrane [98], if we consider the surface of the droplet as a very thin elastic membrane, then the shape of the droplet can be expressed as Eq. (3.2)

$$y = \frac{1}{2}(P/2S)(a^2 - r^2) + \frac{1}{16}(P/2S)^3(a^4 - r^4) + \dots \quad (3.2)$$

Here y is vertical axis and r is the horizontal axis passing through the droplet center, as shown in Figure 3.7(b). At $y=0$, $r=a$ (the radius of droplet aperture). The droplet experiences a surface tension force S and a pressure force P . When the droplet radius is small, we can neglect the higher order terms in Eq. (3.2) and only keep the first item, which implies that the droplet presents a parabolic shape. When the droplet is activated, the external voltage causes the pressure force P to increase, which in turn changes the droplet's shape. However, the droplet still keeps a parabolic shape.

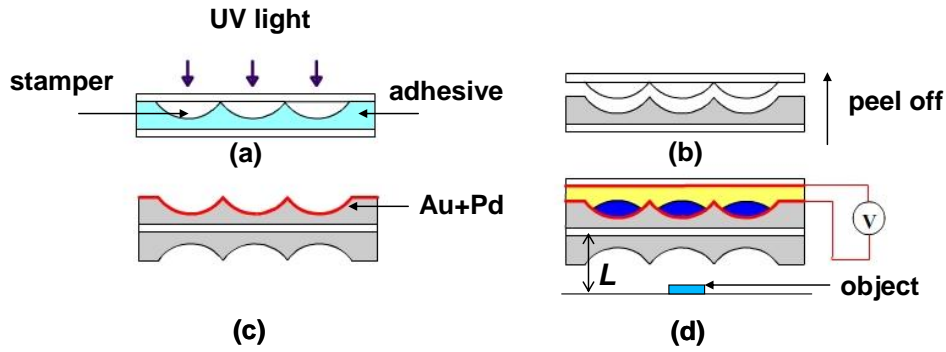


Figure 3.8: The device fabrication procedure: (a) UV exposure, (b) Peeling off the stamper, (c) Aligning the polymer bases under microscope, then coating Au + Pd electrode, and (d) Dropping liquids and sealing the cell.

Figure 3.8 shows the device fabrication procedures, which are similar to the dielectric liquid lens with well-shaped electrode [32]. The only difference is: after fabricating two sets of microlens pattern (Figure 3.8(a) and (b)), we carefully align them under the microscope to form a bi-concave polymer base. To prove concept, we deposited a conducting layer (alloy of gold and palladium) by using a sputter coater (from EMITECH) on the top surface of the base as the bottom electrode, as shown in Figure 3.8(c). The cell gap is $\sim 270 \mu\text{m}$. A top view of the lens cell is shown in Figure 3.9(a).

The performance of the dielectric liquid microlens with

in a bi-concave polymer base was evaluated through an optical microscope. A small number “2” as an object was placed under the microscope. Firstly, the distance between the object and the bottom glass substrate L , as shown in Figure 3.8(d) was set at 3 mm. Figure 3.9(b) shows the image observed through the microscope without any dielectric liquid microlens. Then we inserted the liquid lens in the optical path, refocused the microscope, and observed the images again. A virtual erect and diminished image was observed at $V=0$ (Figure 3.9(c)), which indicated that our lens showed a negative optical power. The image began to grow when actuated

at $15V_{\text{rms}}$, and kept growing as the voltage was further increased. This is because the droplet of liquid-2 gradually contracts as the driving voltage increases, leading to a reshaped droplet profile. As a result, the optical power of the top sub-lens (the positive liquid lens consisting of L1 and L2) is enhanced, while that of the lower sub-lens (the bi-concave polymer base) keeps constant negative, thus the optical power of the entire liquid lens goes less negative, and the virtual erect image is magnified gradually, as shown in Figure 3.9(d) and Figure 3.9(e). At $V=39V_{\text{rms}}$, the image size (Figure 3.9(f)) was almost the same as that of the original image (Figure 3.9(b)). This implies that the optical power of the top and the lower sub-lenses are cancelled with each other, and the whole lens shows no optical power. At $V=90V_{\text{rms}}$, the image (Figure 3.9(g)) is still erect but the size is larger than that of the original image. Further contraction in the droplet eventually turns the whole lens into a positive optical power.

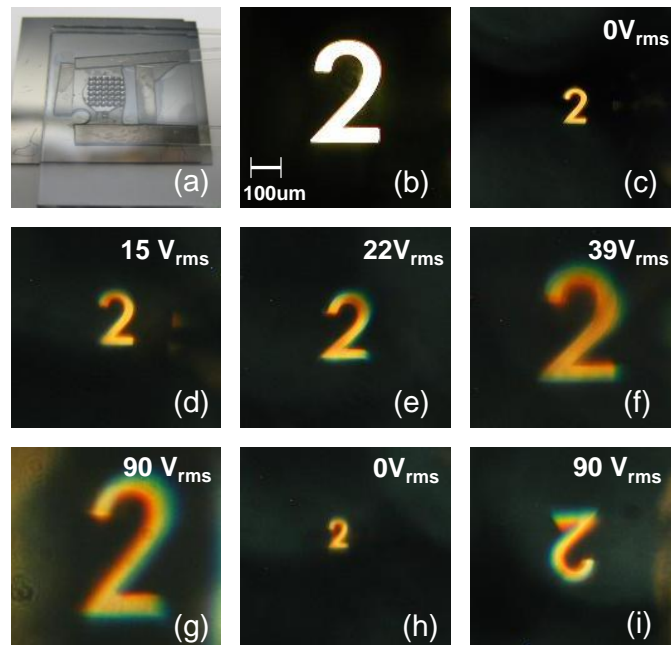


Figure 3.9: (a) Top view of the device, and the image observed through the microscope at $L=3\text{mm}$ (b) without any liquid lens (c)-(g) with the dielectric liquid microlens driven at different voltages, and at $L=7\text{mm}$ (h) $V=0$, and (i) $V=90V_{\text{rms}}$.

In another experiment, we increased the distance between the target and the bottom glass substrate L to 7 mm. At $V=0$, the size of the erect image (Figure 3.9(h)) was further reduced as compared to that in Figure 3.9(c), because the distance between the object and the liquid lens was increased. At $V=90V_{\text{rms}}$, an upside down and diminished image (Figure 3.9(i)) was observed. These indicate that the focal length of our liquid lens is electrically tunable and its optical power can be continuously tuned between negative and positive. Chromatic aberration is observed in the images due to the material dispersion. The Abbe number of L2 is relatively small ~ 22 . Meanwhile, the curvature of the droplet increases with the operating voltage. As a result, the chromatic aberration is severe in the high voltage state [99]. To reduce chromatic aberration, we need to choose proper liquids with a large Abbe number.

A small scattering is also observed due to slight nonuniformity of the well-shaped electrode, which originates from the slow stage rotation speed of the sputter coater. Coaxial design is important in order to maintain good optical functions of a liquid lens [31]. The optic axis of our liquid lens is slightly deviated from its normal because of the minor misalignment in the bi-concave polymer base and the nonuniformity of the bottom well-shaped electrode. The transmittance of our lens is $\sim 50\%$ at $\lambda=550$ nm. Most of the loss originates from absorption of the metal electrode (Au-Pd alloy) and from interface reflections. These drawbacks can be overcome by coating ITO electrode on a commercial bi-concave microlens and applying specific liquid confinement structures [31].

The BFD of the dielectric microlens shown above was measured through a microscope. Figure 3.10 shows the experimental set-up for the measurement. A resolution target placed directly above the lamp was used as an object for imaging, and the lens sample was placed on the stage of the microscope. A “red cross” was marked on the top glass substrate for focusing. At

first, we adjusted the stage until seeing a clear image of the “red cross”, and the position of the stage was marked as position A, as shown in Figure 3.10(b). Then we adjusted the stage to get a clear image of the target bar, and the position of the stage was marked as position B (Figure 3.10(c)). Comparing the focal length with the object distance, the position of the object can be assumed as infinity. Thus the distance from position A to B is considered as BFD of the dielectric liquid microlens. The voltage dependent focal length is plotted in Figure 3.10(d) as blue dots. At $V=0$, the inherent focal length of the microlens is ~ -7.56 mm. As the voltage increases, the focal length firstly goes to negative infinity at $V\sim 39V_{\text{rms}}$, and then comes in from positive infinity. At $V=90V_{\text{rms}}$, it is decreased to ~ 3.22 mm.

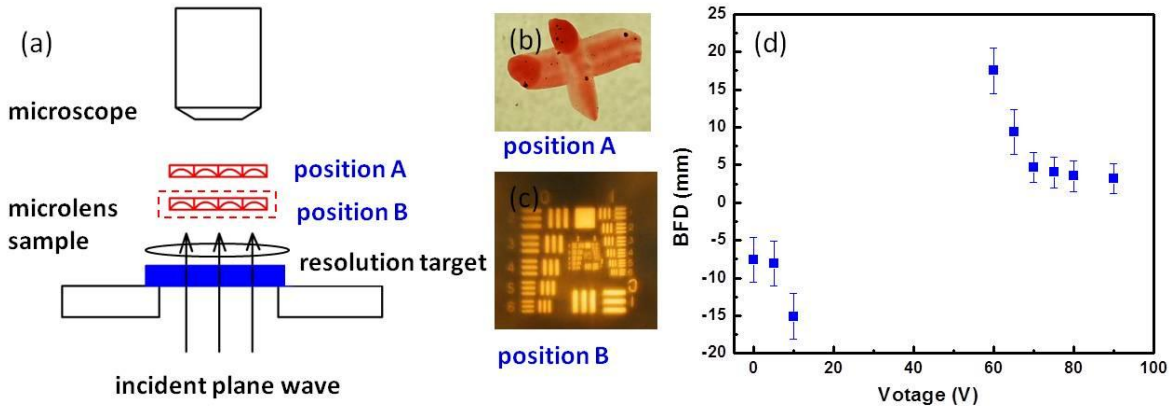


Figure 3.10: (a) Experimental set-up for measuring the focal length, (b) Focusing on the top glass substrate, (c) Focusing on the image of the target, and (d) Measured focal length at various driving voltages.

We also calculate the theoretical BFD in Zemax. The lens structure and parameters used for ZEMAX simulation are shown in Figure 3.11. The top surface of the droplet is considered as parabolic shape in the Zemax simulation. In the relaxed state, the measured apex distance is $t_d\sim 0.147$ mm, and the calculated BFD is ~ 9.0 mm, while the measured BFD is ~ 7.56 mm. At

$V=90V_{\text{rms}}$, the measured D and t_d are ~ 0.606 mm and ~ 0.167 mm, respectively. The calculated BFD is ~ 2.49 mm, which is slightly shorter than the measured data (~ 3.22 mm) at $V=90V_{\text{rms}}$. These minor differences are attributed to the assumption of infinity object and the measurement error of lens dimension because it is difficult to precisely measure the dimension of such a small liquid droplet through an optical microscope.

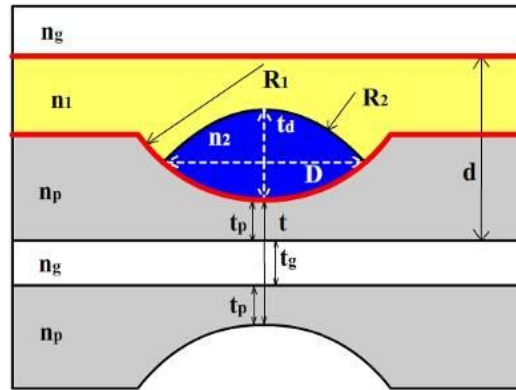


Figure 3.11: Lens structure and parameters for ZEMAX simulation.

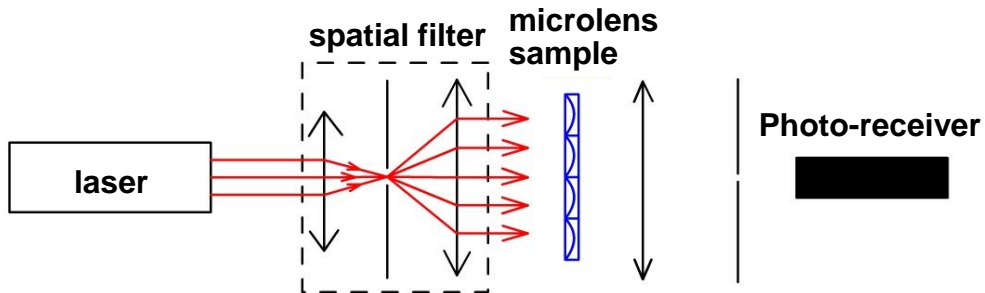


Figure 3.12: Experimental set-up for measuring the response time.

Response time is another important issue for adaptive liquid lenses. In a dielectric liquid lens, the contracting speed of the droplet mainly depends on the dielectric force and the relaxing speed depends on the viscosity of the liquids and the related interfacial tensions [28]. Since the deformation of a liquid droplet profile is related to the balance of electric energy, surface energy,

adhesion energy, and gravitational energy [26], it is very difficult to theoretically calculate the response time. Thus, we measured the lens response time using the set-up shown in Figure 3.12. The lens sample was mounted on a linear metric stage. A He-Ne ($\lambda \sim 633$ nm) laser beam was collimated and expanded to illuminate the sample. A large area visible photo-receiver (Model 2031, New Focus) connected to an oscilloscope (TDS 3032B, Tektronix) was used to measure the intensity variation induced by the dielectric liquid microlens. We applied a square voltage of $90 \text{ V}_{\text{rms}}$ ($f \sim 300$ Hz) to the lens cell. The contracting and the relaxing speed were measured to be ~ 13 ms and ~ 18 ms, respectively.

3.3 Electro-optical Properties of Dielectric Liquid Microlens

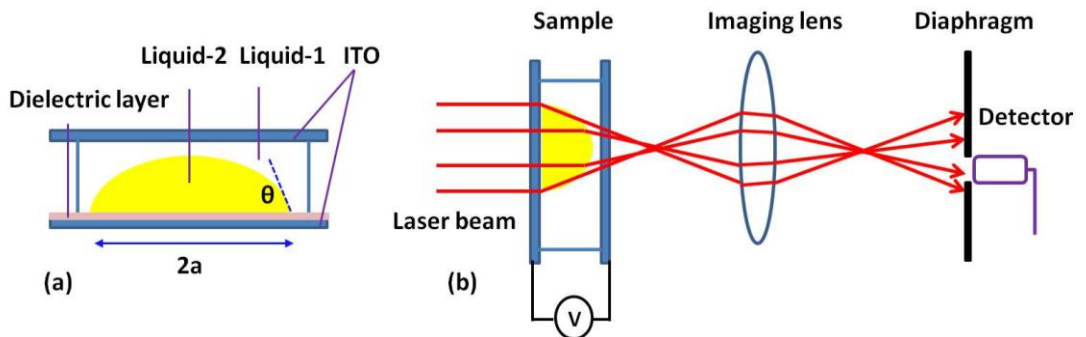


Figure 3.13: (a) Side-view of the dielectric liquid lens cell and (b) Experimental set-up for measuring the electro-optical properties of liquid droplets.

Figure 3.13(a) shows the side-view structure of a dielectric liquid lens cell. In the voltage-off state, the droplet is relaxed and has a spherical shape due to the balanced interfacial tension between droplet (liquid-2, L2)/dielectric layer, droplet (liquid-2)/surrounding liquid (liquid-1), and surrounding liquid (liquid-1, L1)/dielectric layer. The aperture of the droplet is $2a$ and the contact angle on the bottom dielectric layer is θ . When an AC voltage is applied to the

cell, the droplet experiences a nonuniform electric field. The dielectric particles on the droplet surface become electrically polarized as a result of partial charge separation, which leads to an induced dipole moment. The effective dipole moment is expressed as Eq.(3.3) [68]

$$P = 4\pi\epsilon_1 \left[\frac{\epsilon_2 - \epsilon_1}{\epsilon_2 + 2\epsilon_1} \right] r^3 \vec{E} \quad (3.3)$$

where r is the radius of the droplet curvature, ϵ_1 and ϵ_2 are the dielectric constants of the surrounding liquid (L1) and the droplet (L2), respectively, and E denotes the electric field. Usually electric polarization responds to an electric field by shifting charge particles (electrons) around, which means it always some time for the charge particles to be accelerated and de-accelerated. Therefore, the response to the field is dependent on the frequency of electric field. If the frequency is very high, the dielectric constants of ϵ_1 and ϵ_2 will approach to 1. In such a case, P equals 0 or is very small. Due to the dipole moment, the droplet surface bears a dielectric force:

$$F_{DEP} = \frac{1}{2} \text{Re}(P \bullet \nabla) E \quad (3.4)$$

From Eqs. (3.3) and (3.4), we can get Eq.(3.5)

$$F_{DEP} = 2\pi r^3 \epsilon_1 \text{Re} \left(\frac{\epsilon_1 - \epsilon_2}{\epsilon_1 + 2\epsilon_2} \right) \nabla E^2 \quad (3.5)$$

Because of the curved droplet surface, the electric field exerting on the droplet has a gradient. According to our previous analysis [28], the strongest F_{DEP} is at the border of droplet aperture. When the dielectric force is sufficiently strong, the liquid particles inside the droplet are forced to shift and the droplet surface is reshaped in order to reach a new force balance. According to Knollman's theory [98], if the interfacial surface tension of the droplet is

considered as that of the elastic membrane in a membrane-encapsulated lens, then the surface configuration of the droplet can be deduced in a cylindrical coordinate system (z, r) as expressed in Eq.(3.6):

$$z = \frac{P}{4T}(a^2 - r^2) \quad (3.6)$$

where P is the Laplace pressure of the droplet interface, T the interfacial tension of the droplet, and a the aperture of the droplet. According to Eq. (3.6), the surface configuration of the droplet exhibits a parabolic shape, and the shape of the droplet is dependent on the surface tension and the pressure P . Thus if the tension T is large and the aperture a is small, its parabolic shape can be approximated by a spherical shape. The error for such an approximation is negligible. Furthermore, usually T is constant, so the droplet shape is mainly governed by the change of P . From Eq. (3.5), F_{DEP} can change the radius of the droplet, thus the pressure P is varied accordingly.

A dielectric liquid microlens with the structure in Figure 3.13(a) was prepared by using SL-5267 and glycerol as L2 and L1, respectively. Their properties are listed in Table 3.1. The cell gap was $\sim 100 \mu\text{m}$. To characterize the electro-optical properties of the droplets, we used a simple set-up as Figure 3.13(b) depicts. A collimated He-Ne laser beam was used to probe the cell at normal incidence. The transmitted beam was expanded by an imaging lens and received by a photodiode detector. A diaphragm was placed right before the detector. At $V=0$, we adjusted the diaphragm aperture so that only part of the beam was received by the detector. When a sufficiently high voltage was applied to the sample, the focal length of the droplet became shorter, resulting in a decreased effective focal length of the system. Hence, the laser beam was expanded and the intensity received by the detector was decreased.

To study the electro-optical properties of the droplets, several liquid droplets with different aperture sizes were prepared and their surface profiles were observed using an optical microscope. We first selected a droplet with 210- μm -aperture (diameter) for investigation. Figure 3.14(a) shows the surface profile of the droplet. Its aperture is indeed quite circular. To analyze the focusing performance of the droplet, we used a CCD camera to capture the transmitted light spots. At $V=0$, a large light spot was observed (Figure 3.14 (b)), while at 60 V_{rms} , the transmitted light was tightly focused and a small spot was obtained (Figure 3.14 (c)). This is because the droplet surface was reshaped and the focal length of the droplet was changed accordingly. Figure 3.15(a) shows the voltage-dependent light intensity measured through the droplet, during forward and backward scan, respectively. As the applied voltage increases from 0 to 80 V_{rms} ($f\sim 300$ Hz), the intensity decreases gradually, which implies the droplet shape has the tendency to contract. In the backward scan, the light intensity increases when the voltage decreases from 80 V_{rms} to 0. These two curves overlap reasonably well, i.e., the hysteresis is small at high voltage. The hysteresis is mainly due to the interfacial tension of the oil droplet and the dielectric layer. Such a result shows that the droplet can recover to its initial state when the voltage is removed.

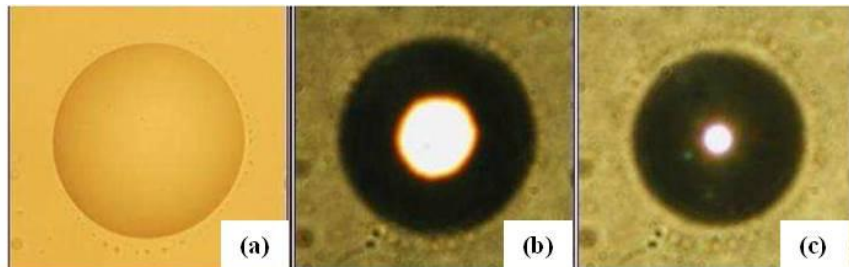


Figure 3.14: Images observed through an optical microscope by focusing on (a) droplet surface, (b) Defocus state at $V=0$, and (c) Focus state at $V=60 V_{\text{rms}}$

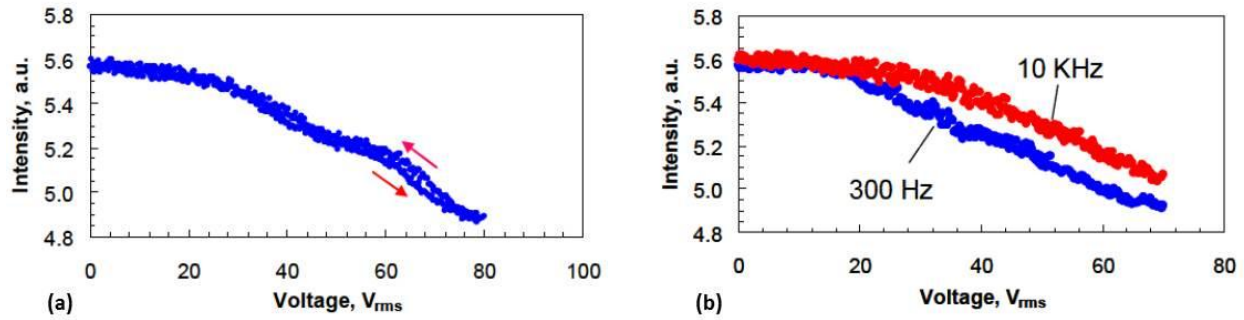


Figure 3.15: Voltage-dependent intensity change of (a) a 210- μm -aperture droplet at $f=300\text{Hz}$ at forward and backward scans, and (b) at $f=300\text{ Hz}$ and 10 kHz frequencies.

To study the frequency effect on the droplet shape change, we drove the droplets under different frequencies. The voltage-dependent intensity at 60 Hz, 300Hz, 500 Hz and 10 kHz were measured respectively. Figure 3.15(b) shows two curves of voltage-dependent intensity at 300 Hz and 10 kHz, respectively. In the low voltage region, two curves overlap quite well. As the voltage exceeds 20 V_{rms} , frequency begins to impact the intensity change. The 10 kHz voltage leads to a smaller intensity change than that of 300 Hz, i.e., a lower frequency voltage causes a larger shape change. This is mainly due to the response of induced dipole moment to the frequency as analyzed above. As the electric field frequency increases significantly, the induced dipole moment of each liquid particle gets weaker so that it cannot follow the frequency change. Therefore, F_{DEP} decreases resulting in a smaller droplet's shape change. As the operating frequency increases, the ability of the voltage to deform the shape of the droplet decays. Because the droplet cell behaves like a capacitor, the liquid will bear a large current at a high frequency. As a result, the droplet will be heated, the device performance will be deteriorated and the power consumption will be a concern. Ideally, the dielectric liquid droplet should be operated at a low frequency or DC voltage. For the device operating at 80 V_{rms} (300 Hz), the power consumption is estimated to be less than 0.5 mW.

Dynamic response is another important factor for the adaptive liquid lenses. To measure the response time, we used a digital oscilloscope to record the transient intensity change. Figure 3.16(a) shows the measured response time of the 210- μm -aperture droplet at different square-wave voltage bursts ($f=300$ Hz, 200-ms width). Both rise time (droplet reshapes from relaxed to contracted states) and decay time (the droplet reshapes from contracted to relaxed states) are measured, indicated by filled circles and open circles respectively. At $V=50$ V_{rms} , the rise time is ~ 20 ms. As the voltage increases, the rise time gradually decreases because of the increased dielectric force. However, the decay time is not sensitive to the applied voltage (or shape change). It fluctuates a little bit as the voltage changes, but on average the decay time is ~ 24 ms.

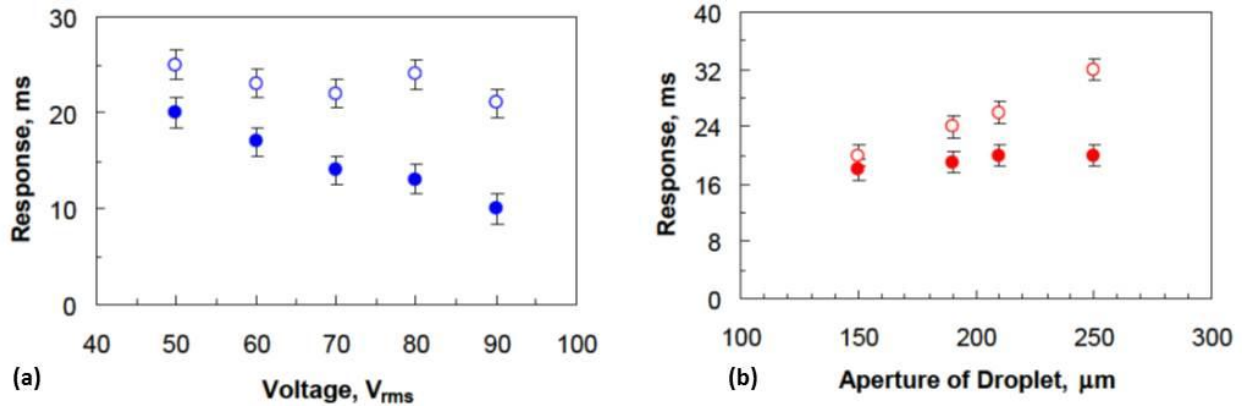


Figure 3.16: Measured response time of (a) a 210- μm -aperture droplet at different voltages (solid circles: rise time, open circles: decay time), and (b) different-sized droplets under a square burst driving.

We also measured the rise time and decay time of droplets with various sizes at a fixed voltage ($50V_{\text{rms}}$ -square-burst and 200-ms-width), as shown in Figure 3.16 (b). As the droplet aperture increases, the rise time does not change noticeably. However, the decay time increases gradually. For each droplet, the measured decay time has some fluctuations, as given by the error bar. A larger droplet needs a longer time to relax to its original shape. In general, the rise time is mainly dependent on the generated dielectric force, while the decay time is governed by several

factors, such as interfacial surface tensions, droplet size, and viscosity of the employed liquids. Theoretical calculation of decay time is rather difficult because its interfacial tension is difficult to measure. To improve decay time, it is desirable to choose liquid with low viscosity and large surface tension. The droplet cell should work in a suitable temperature range so that both viscosity and interfacial surface tension of the liquids can be taken into consideration.

3.4 Summary

In this chapter, we have demonstrated a tunable dielectric liquid microlens with well-shaped electrode. The well-shaped electrode structure and the bi-convex shape of the liquid droplet both have the ability to generate an inhomogeneous electric field, which not only fixes the position of the microlens but also reduces the operating voltage as compared to a microlens with common planar electrodes. A microlens with 1.8X optical zoom under $V=88 V_{\text{rms}}$ is achieved. The transmission and scattering of the lens can be improved by coating ITO on the well-shaped polymer base. The response time can be shortened using low-viscosity liquids. Such a liquid microlens shows potential applications in cell phone cameras, imaging processing, optical communication and beam steering. We also propose the possibility of fabricating microlens arrays with different aperture and density using a simple method.

We also have demonstrated a dielectric liquid microlens with switchable negative and positive optical power by introducing a bi-concave polymer base. Our approach enables focus tuning from negative to positive or vice versa in a single dielectric lens without any moving part. The focal length of our lens can be tuned from ~ -7.56 mm to infinity to ~ 3.22 mm when the voltage increases from 0 to $90 V_{\text{rms}}$. The response time is reasonably fast: ~ 13 ms in rising and

~18 ms in relaxing. The dimension of the bi-concave polymer base can be specially designed to get the desired lens' dynamic range. Such a liquid microlens will find potential applications in vision and imaging devices, especially in 2D-3D displays.

To better understand the fundamental electro-optic properties of the dielectric liquid lens, we have studied the electro-optic characteristics of different liquid droplets. From our experimental results, we find that the surface of a droplet can be reshaped by an external voltage with negligible hysteresis. Both amplitude and frequency of the voltage affect the droplet shape change. With the same amplitude of the applied voltage, a lower frequency can cause a larger shape change. The rise time is dependent on the applied voltage, but the decay time is jointly determined by the interfacial surface tensions, droplet size, and viscosity of the employed liquids. Our study will help to optimize the lens performances by considering the impact of operating voltage and the droplet size.

CHAPTER 4 DISPLAYS AND OPTICAL SWITCHES BASED ON DIELECTROPHORETIC EFFECT

4.1 Color Display Based on Dielectric-Effect Induced Light Channel

In a common dielectric liquid lens, the apex distance of the droplet is much smaller than the cell gap in order to prevent the dome of the droplet from touching the top substrate [26-28,32,36]. If it touches the top substrate in a voltage-on state, the lens performance will be severely degraded and the droplet will no longer return to its original shape [30]. When such a droplet is used for beam control, the control ability is rather limited and the required voltage is very high. In this chapter, we demonstrate a single-pixel transmissive color display based on dielectric effect-induced light channel. In a normal transmissive color liquid crystal display, e.g., TV, the displayed color is governed by the embedded color filters [19,100]. Each color filter transmits one designated color. The optical efficiency is only ~30%. In our approach, a colored droplet and a black surrounding liquid are adopted. In the voltage-off state, the incident beam is absorbed by the black surrounding liquid, resulting in a dark state. As the voltage increases, the droplet dome is uplifted by the dielectric force and touch the top substrate. A dielectric effect-induced light channel is open and the incident beam is transmitted. More importantly, the liquid droplet returns to its initial state upon removing the voltage, and the pixel becomes dark again. The operating voltage is relatively low and the dynamic response is reasonably fast.

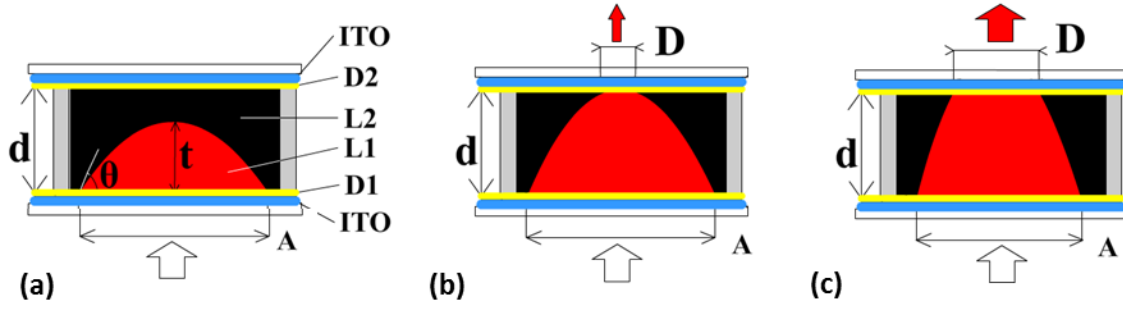


Figure 4.1: (a) Side-view structure of the cell at $V=0$ (b) Droplet dome touching the top substrate under a voltage, and (c) Enlarged touching area when the voltage is increased.

Figure 4.1(a) shows the side-view structure of the droplet cell, which is very similar to that of dielectric liquid lens. A small amount of liquid-1 (L1, colored liquid) is dispensed on the dielectric layer surface of the bottom substrate to form a droplet. The liquid droplet has a fairly large surface tension. The area that the droplet contacts on the bottom surface is defined as the droplet aperture (A). Liquid-2 (L2, black liquid) with a relatively small surface tension filled the surrounding space. In the voltage-off state, the droplet is in a relaxing state. Its apex distance (t) is smaller than the cell gap (d), thus the dome of the droplet does not touch the top substrate. The incident beam is blocked by the black surrounding liquid and a dark state is obtained, as Figure 4.1(a) shows. Such a structure is stable when the interfacial tension satisfies the following Eq.(4.1):

$$\gamma_{L1,L2} \cos \theta = \gamma_{L1,D1} - \gamma_{L2,D1} \quad (4.1)$$

where γ is the interfacial tension and subscripts L1, L2, and D1 represent liquid-1, liquid-2, and bottom dielectric layer, respectively, and θ is the contact angle of the droplet. When a voltage is applied to the cell, the droplet surface bears an inhomogeneous electric field. The dielectric force exerted on the droplet can be expressed as Eq.(4.2) [101]:

$$F_d = \frac{1}{2} \varepsilon_0 (\varepsilon_1 - \varepsilon_2) \nabla (E \cdot E) \quad (4.2)$$

where ε_0 , ε_1 , and ε_2 represent the permittivity of free space, liquid-1, and liquid-2, respectively, and E denotes the electric field on the curved droplet. If the applied voltage is high enough, the surface of the droplet can be reshaped adaptively in order to reach a new balanced state. If the condition $t \geq d$ is satisfied, the dome of the droplet will touch the top substrate surface, as shown in Figure 4.1(b). The contact area of the dome D will further enlarge with the increased voltage, thus more light will pass through, as Figure 4.1(c) shows. The shape of the droplet is fixed under a given voltage due to the balanced forces. However, this balance will be broken and the shape of the droplet will adjust itself adaptively when the voltage is removed. If the droplet (L1)'s surface tension is much larger than that of the top dielectric layer (D2) and surrounding liquid (L2), the dielectric layer will not be strong enough to maintain the shape of the droplet. The unbalanced surface tension will drive the droplet to its initial state, and the pixel will show dark (Figure 4.1 (a)) again.

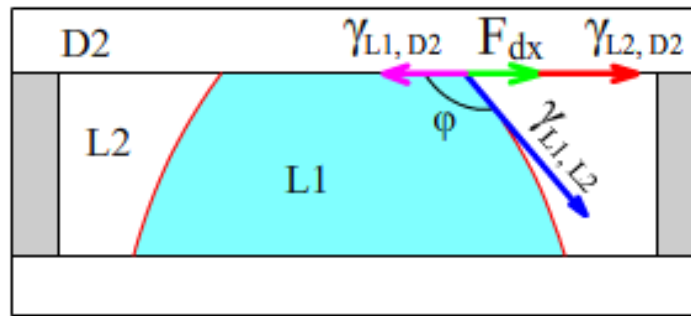


Figure 4.2: Force analysis (dielectric force and interfacial tensions) for the system balance.

The detailed explanation is shown in Figure 4.2. If ε_1 is larger than ε_2 , the generated dielectric force (F_d) orients in outward direction. Such a force has horizontal and vertical components, but only the horizontal component (F_{dx}) can deform the droplet. When the shape of

the droplet is stabilized, the dielectric force and the interfacial tensions satisfy the following relationship:

$$\gamma_{L1,D2} = \gamma_{L2,D2} - \gamma_{L1,L2} \cos \varphi + F_{dx} \quad (4.3)$$

where $\gamma_{L1, D2}$ and $\gamma_{L2, D2}$ denote the interfacial tension of L1/D2 and L2/D2, respectively, and φ is the contact angle of the droplet on the top substrate. If F_{dx} decreases, φ will increase accordingly to reach a new balance, as depicted in Figure 4.2. It means the contact area of the droplet has a tendency to shrink as the applied voltage decreases. From Eq. (4.3), if $\gamma_{L1, D2} \gg \gamma_{L2, D2}$, then removing the voltage ($F_{dx} = 0$) will cause the angle φ to be 180° , and the droplet will set apart from the top substrate and return to its original shape.

Table 4.1: Properties of liquid-1 (L1: Glycerol, Sigma-Aldrich), liquid-2 (L2: ZLI-2585, Merck)

Material	Dielectric constant	Surface tension (mN/m, @20 °C)	Density (g/cm ³)	Color
L1	47	64	1.26	Clear
L2	7	20	NA	Clear

To prove our concept, a droplet cell with the structure shown in Figure 4.1 (a) was fabricated. Liquid glycerol and dye-doped LC ZLI-2585 was chosen as the droplet material and surrounding liquid, respectively. Their properties are listed in Table 4.1. For white/black light switch, 1.5 wt% black dye was doped in a negative (dielectric anisotropy $\Delta\epsilon < 0$) LC mixture. The aperture of the droplet (A) is $\sim 340 \mu\text{m}$ and the cell gap was $\sim 200 \mu\text{m}$. In principle, such a cell can restore a droplet with $400 \mu\text{m}$ maximum aperture without touching the top substrate. But to keep a safe distance from the droplet dome to the top surface, a smaller droplet size is preferred. The dye-doped LC is immiscible with the glycerol, and the absorption of dyes is isotropic due to random LC orientation. The black dye clusters was not stirred thoroughly, so that some of them

could float in the LC bulk. We intentionally did this for two purposes: to clearly observe the motion of the LC fluid during droplet deforming, and to track the aperture change of the top terminal.

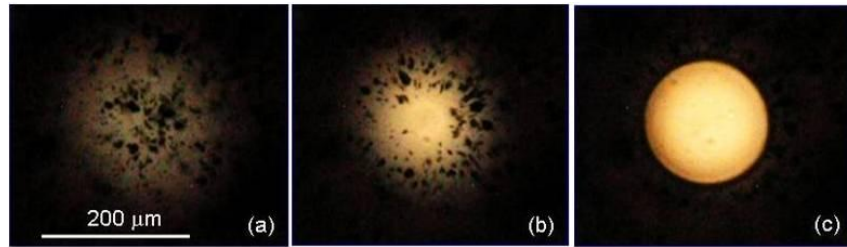


Figure 4.3: A droplet cell for black/white switch driven at (a) $V=0$, (b) $25 V_{\text{rms}}$, and (c) $40 V_{\text{rms}}$.

Figure 4.3(a) shows that at $V=0$, the droplet is covered by the dye-doped LC and the black dye clusters are randomly dispersed in the LC host. The dye clusters covering the top of droplet reveals that the droplet's dome does not touch the top substrate in the relaxing state. The dome area gives a high brightness and only few dye clusters are dispersed in that area, indicating the dome is relatively close to the top substrate. It appears darker in the droplet periphery due to the absorption of randomly dispersed dye molecules. As the voltage ($f \sim 300$ Hz) increases, the dye clusters over the dome center begin to move away. At $V=25 V_{\text{rms}}$, the dye clusters are pushed aside because the dome has just touched the top surface (Figure 4.3(b)). At $V=40 V_{\text{rms}}$, the contact area continues to grow and become flat (Figure 4.3(c)). Under such a circumstance, the incident light would pass through the liquid pipe with very little loss, except for the refraction of the off-axis light. Keep on increasing voltage does not alter the top aperture too noticeably. When the voltage is decreased to $\sim 30 V_{\text{rms}}$, the dye clusters begin to shift from periphery to dome. It means the dome of the droplet is separated from the top substrate. As the voltage is removed ($V=0$), the droplet returns to its original shape (Figure 4.3(a)) due to the large surface tension of glycerol. If the black liquid exhibits a high optical density, the reconfigurable droplet would act

as a high performance white light switch and the required operating voltage would be fairly low. It opens new applications for tunable iris, light shutter and white/black display.

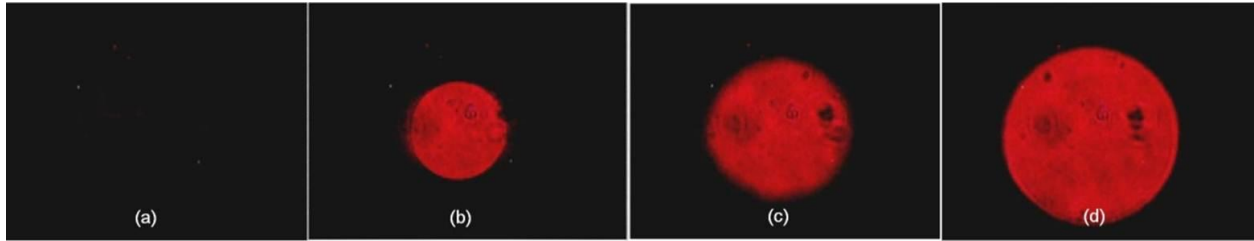


Figure 4.4: A droplet cell for black/red switch driven at (a) $V=0$, (b) $V= 35 V_{rms}$, (c) $V=42 V_{rms}$, (d) $V=50 V_{rms}$.

In addition to black/white switch, another black/red switch for color display is demonstrated. We mixed 4 wt% Rose Bengal with glycerol at room temperature and the mixture exhibited a brilliant red color. More importantly, Rose Bengal is immiscible with the black LC. The aperture of the red droplet is $\sim 130\mu\text{m}$, and the cell gap is $\sim 100 \mu\text{m}$. Figure 4.4 shows the black/red switching at various voltages. At $V=0$, the cell presented a very good dark state and the contour of the droplet was hardly resolved (Figure 4.4(a)). This is because the gap between the dome and top substrate is relatively large, and the gap is filled with the black LC. This layer of black LC highly absorbs the incident light, leading to a good dark state. As the voltage was increased to $\sim 35 V_{rms}$, a clear red circular area suddenly appeared, (Figure 4.4(b)). The red area represents the top terminal aperture D , as shown in Figure 4.1(b). The aperture kept growing when the voltage was gradually increased (Figure 4.4(c) and Figure 4.4(d)). Removing the voltage, the droplet returned to its original dark state (Figure 4.4(a)). Some tiny black particles were observed in the red spot, which may result from the undissolved dye clusters.

The electro-optical properties of the device are investigated. The measurement set-up is shown in Figure 4.5. The cell was placed vertically, followed by an imaging lens and a

photodiode detector; a He-Ne laser was collimated and expanded to probe the cell at normal incidence. The response time was measured under a gated square-wave of 45 V_{rms} pulse (500 Hz). The time-dependent transmitted light intensity was recorded by a digital oscilloscope. The rise time and decay time is measured as ~18 ms and ~32 ms, respectively. The contrast ratio is measured as 10:1 using a 5-mW laser beam.

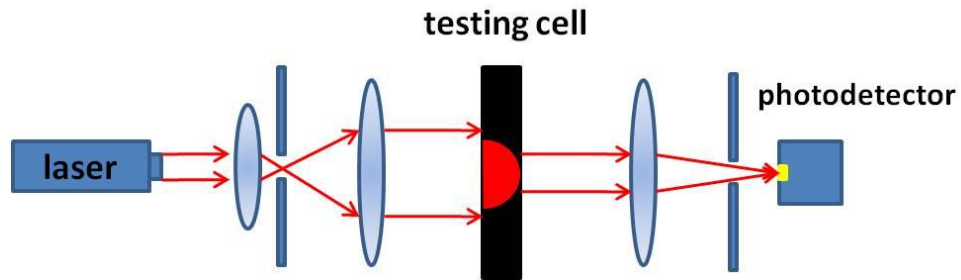


Figure 4.5: Measurement set-up for electro-optical properties.

Figure 4.6 shows another blue/white switch at various voltages. This time, we mixed 1.5%wt blue dye (M-137, Mitsui Toatsu Dyes) with the surrounding LC mixture while kept the glycerol droplet no-dye-doped. The aperture of the red droplet is ~150 μm, and the cell gap is ~100 μm. At V=0, the center area of the cell presents a blue color while the border area presents a black color (Figure 4.6(a)). The reason is that: from the center to the border, the gap between the dome of the droplet and the top substrate gradually increases, and the corresponding absorption increases accordingly. At V=25 V_{rms}, a weak white light spot with a fussy periphery starts to appear (Figure 4.6(b)). This is because the droplet's dome is uplifted toward the top substrate and the blue LC layer thickness is reduced. At V= 30 V_{rms}, the dome slightly touches the top substrate surface, and the blue LC is pushed aside. A white circular spot having a very shape periphery comes into sight, together with some residual blue color (Figure 4.6(c)). At V=44 V_{rms}, the touching area is further enlarged because the dome largely touches the top

substrate, and there is no obvious noise in the background (Figure 4.6(d)). After removing the voltage, the droplet returns to its initial state and the pixel becomes blue again (Figure 4.6(a)).

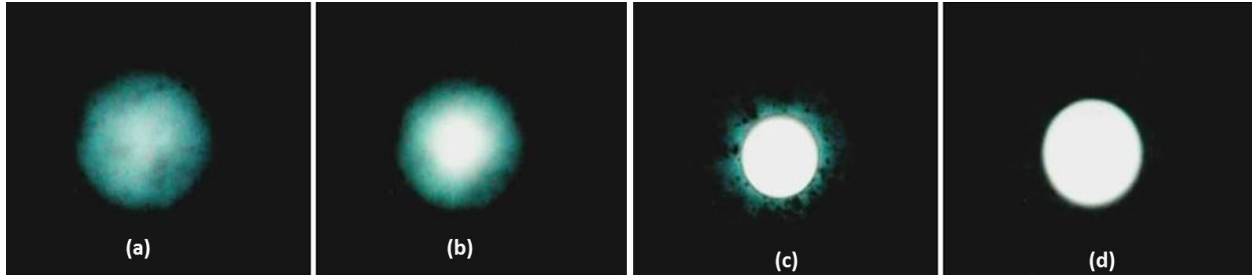


Figure 4.6: A droplet cell for blue/white switch driven at (a) $V=0$, (b) $V= 25 V_{rms}$, (c) $V=30 V_{rms}$, (d) $V=44 V_{rms}$.

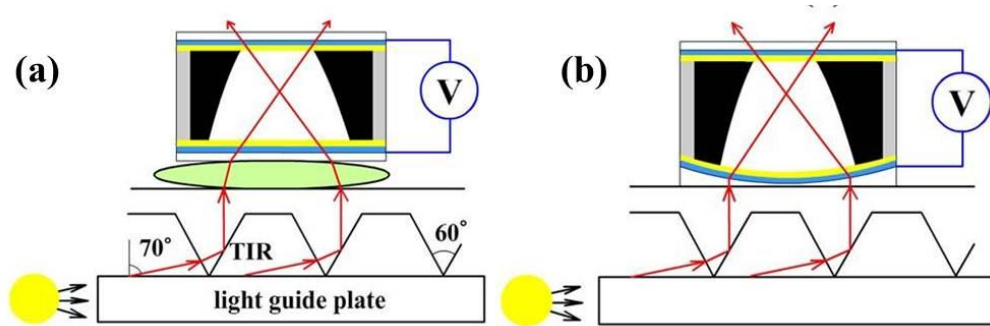


Figure 4.7: Two approaches for obtaining a wide-view and high transmittance display thru edge-lit backlight.

To improve contrast ratio, a black isotropic liquid (rather than dye-doped liquid crystal) with a high optical density is desirable. Increasing the distance between droplet dome and top surface would improve the contrast ratio; however, the required voltage will increase accordingly. All in all, the droplet cell structure needs to be optimized to get the best performance. In the practical application, we may use a turning film and a microlens array to redirect the backlight coming from the edge-lit system, widening the viewing angle and enhancing the light efficiency [102], as shown in Figure 4.7(a). To further simplify the system, a micro-lens embedded cell structure is introduced, as Figure 4.7(b) shows. To achieve a full color display, green and blue

color pixels need to be developed. We should find proper green and blue dopants (dissolvable with the glycerol but immiscible with the black liquid) or pure colored oils (immiscible with black liquid) for the devices. Pixel array, which are more attractive for practical applications, still needs to be further investigated.

4.2 Color Display and Variable Optical Attenuator Based on Voltage-Stretchable Liquid Crystal

Droplet

4.2.1 Color Display Based on Voltage-Stretchable Liquid Crystal Droplet

A transmissive color display based on DEP-induced light channel was demonstrated [37] in Chapter 4.1. At $V=0$, the incident light is absorbed by the black liquid, resulting in a dark state. As the voltage increases, the droplet dome touches the top substrate and becomes flat, a dielectric effect-induced light channel is open and the beam is transmitted. While the voltage is removed, the droplet recovers to its original spherical shape. This polarization-independent liquid display shows a reasonably fast response. However, the contrast ratio is only $\sim 10:1$. To achieve a wide viewing angle and high optical efficiency, an extra turning film and a microlens array are required in the integration with a conventional edge-lit backlight. Besides, it only works in transmissive mode.

In Chapter 4.2.1, we will discuss a single-pixel color display based on voltage-stretchable LC droplet. By choosing proper liquid materials, the dye-doped droplet shrinks with the smallest surface-to-volume ratio at $V=0$. As V increases, the droplet is stretched to spread like a film by DEP force. The gray scale is achieved by stretching the droplet to different extent. Upon

removing the voltage, the droplet returns to its initial state. Such a display does not need any polarizer and color filters. It shows wide viewing angle, good contrast ratio and large aperture ratio, as well as easy integration with the edge-lit backlight. Both transmissive and reflective modes can be configured. The relatively low operating voltage and reasonably fast transition speed make it promising for mobile displays.

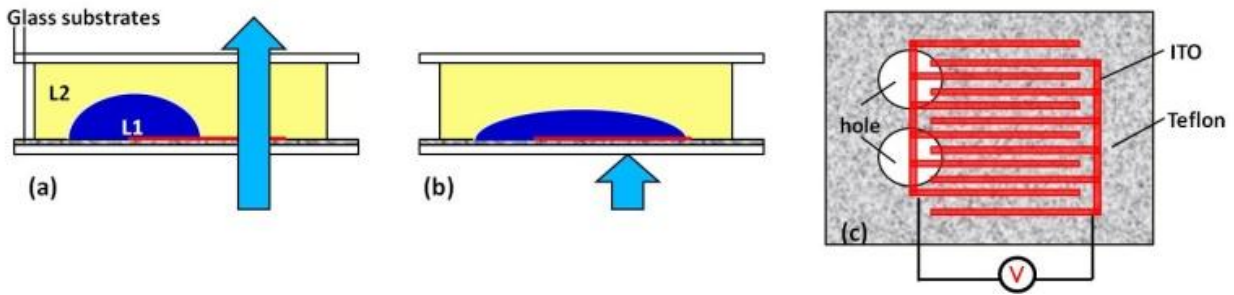


Figure 4.8: (a) Side-view of the cell structure at V-off, (b) black state at V-on, and (c) layout of the bottom substrate. The dimension of the hole and ITO stripes are not drawn by scale.

Figure 4.8(a) shows the side-view structure of our proposed device. The droplet (L1) and the surrounding liquid (L2) are sandwiched between two glass substrates. The detailed layout of the bottom substrate is shown in Figure 4.8(c). Its inner surface is coated with interdigitated ITO electrodes (marked as red in Figure 4.8), on the top of which is a thin polyimide layer (PI2556, HD Microsystems, surface tension $\gamma_P \sim 40$ mN/m, ~ 1 μm thickness, not shown in Figure 4.8) and a hole-patterned Teflon layer (400S1-100-1, DuPont, $\gamma_T \sim 19$ mN/m, ~ 1 μm thickness, marked as gray in Figure 4.8). These two layers not only provide a suitable contact angle for the droplet [103,104], but also prevent the carrier injection into the cell. Therefore, our device is free from the concern of charge effect. The hole partially contacts with the electrodes, pinning down the position of the droplet. For most liquids with low surface tensions, their dielectric constants are usually very small ($\epsilon \sim 5$). While for the liquids with a large dielectric constant (such as water

$\varepsilon \sim 80$ and glycerol $\varepsilon \sim 47$), their surface tensions are usually very high (over 60 mN/m) at room temperature. To largely stretch the droplet under a low operating voltage, L1 should have a relatively low surface tension (γ) and a large dielectric constant [35]. Here we chose a Merck LC mixture ZLI-4389 as L1 and silicone oil (from Sigma-Aldrich) as L2. These two liquids are immiscible with each other and match well in density. Their properties are listed in Table 4.2. The cell gap was controlled by spacers, and the periphery was sealed by glue.

Table 4.2: Properties of liquid-1 (L1: ZLI-4389, Merck), liquid-2 (L2: Silicone Oil, Sigma-Aldrich)

Material	Dielectric constant	Refractive index	Density (g/cm ³)	Surface tension (mN/m, @20 °C)
L1	$\varepsilon_{//}=56, \Delta\varepsilon=45.6$	$\langle n \rangle \sim 1.58$	0.98	38
L2	2.9	1.4	0.97	21

At $V=0$, the LC droplet shrinks with the smallest surface-to-volume ratio, and only occupies a small area, as Figure 4.8(a) shows. When a voltage is applied to the bottom electrodes, a nonuniform lateral electric field is generated across the ITO stripes. The dielectric force, which is generated via interaction between electric field and the surface polarization induced on the dielectric liquid-liquid interface, is exerted on the liquid interface to deform the interface profile [105]. According to Kelvin's theory, it can be expressed as Eq.(4.2) [101] Since the LC molecules on the droplet border are reoriented by the fringing field, the dielectric constant of the LC on the border is close to $\varepsilon_{//}=56$, which is much larger than that of the silicone oil. Therefore, the droplet border bears the strongest dielectric force along the ITO stripe direction. When the voltage is high enough, in order to reach a new balance among the interfacial tension, friction force from the hole surface and the generated dielectric force, the LC droplet will be stretched outward along the stripes, partially blocking the incident light. If the droplet is further stretched

to totally block the incident light, a black state is achieved, as shown in Figure 4.8(b). Removing the voltage, the droplet will quickly return to its original state because of interfacial tension.

To prove concept, we fabricated a droplet cell with the structure shown in Figure 4.8(a). The LC droplet was doped with 1.2 wt% black dye (S-428, Mitsui Fine Chemicals). The droplet aperture (the diameter of the droplet's touching area on the bottom substrate) is $\approx 800\mu\text{m}$ and the cell gap was $\approx 420\mu\text{m}$. The droplet initially does not appear circular because the hole patterned on the Teflon layer is not in perfect circular shape.

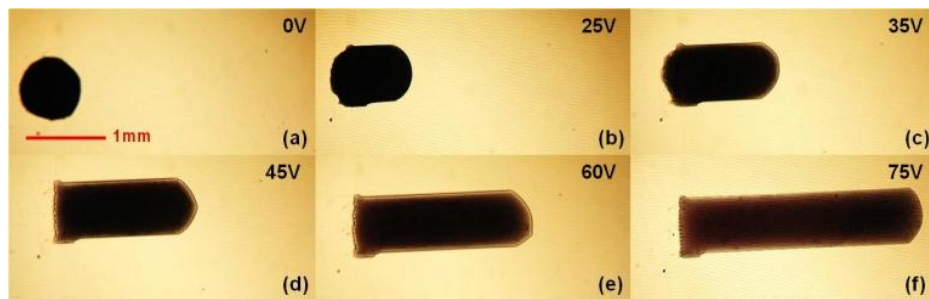


Figure 4.9: Droplet deformation (black pixel switch) at various voltages.

Figure 4.9 shows the droplet deformations as well as the pixel switch at various voltages. At $V=0$, the droplet shrinks to a small area. As the voltage is gradually increased to $25 V_{\text{rms}}$, the droplet begins to stretch along the stripe electrodes. At $V=35 V_{\text{rms}}$, the deformation becomes more noticeable, and goes further with the increased voltage. Compared to the original black area at $V=0$, the black dispersion is stretched by $\approx 3X$ at $V=60 V_{\text{rms}}$, and $\approx 4.5X$ at $V=75V_{\text{rms}}$, respectively. In a practical display, we have to design the pixel and initial droplet size to achieve a suitable aperture ratio. For example, if the final dark state is that shown in Figure 4.9(e), then the aperture ratio is 67%. The aperture ratio can be further enlarged by increasing the voltage to further stretch the droplet. However, this will reduce the residual droplet volume in the hole. Then if we suddenly turn off the high operating voltage on an extremely stretched droplet, the

friction between the droplet and the surrounding liquid begins to play a key role in the recovering process. As a result, the residual droplet may be lifted off from the hole and no longer returns to its original state.

In our experiments, we find that at $V < 35 V_{\text{rms}}$, the rest part of the LC droplet (no embedded electrodes beneath) stays still, while at $V > 35 V_{\text{rms}}$, it begins to move along with the stretched part (embedded electrodes beneath) in the hole area, as Figure 4.9(c) shows. The detailed explanation about the droplet movement is given as follows. When a small LC droplet is dispensed in the patterned hole, it exhibits a nearly spherical shape and a large contact angle on the bottom substrate. Under an operating voltage, the forces exerted on a small group of LC molecules near droplet border are shown in Figure 4.10. The molecules, which are close to the left edge of the liquid-liquid interface, experience the gravity (G) and supporting force (S), viscosity friction (V) and the surface tension (T) [105]. For the molecules close to the right edge of the liquid-liquid interface, besides the four forces mentioned above, they also experience the dielectric force (D), which is perpendicular to the interface between L1 and L2, orienting in outward direction. But only D_{RX} (the horizontal component of the dielectric force on the molecules near the right edge) will deform the droplet. T_{RX} (T_{LX}) is the horizontal component of the interfacial tension on the molecules near the right (left) edge; V_R (V_L) is the viscosity friction on the molecules near the right(left) edge; θ_R, θ_L is the contact angle of the right(left) edge on the bottom substrate. When $D_{RX} > T_{RX} + V_R$, the molecules near the right edge begin to move along the ITO stripe direction, expanding the droplet surface and decreasing its contact angle (θ_R, θ_L) on the bottom substrate. As a result, T_{LX} will increase accordingly. When it is large enough to overcome the viscosity friction ($T_{LX} > V_L$), the rest part of the droplet will start to move forward.

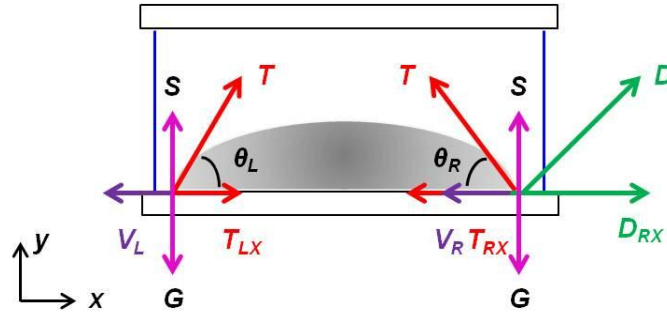


Figure 4.10: Dielectric force, interfacial tension and viscosity friction analysis.

The switching time was measured by monitoring the time-dependent transmitted light intensity in a dark room. The expanding (recovering) time is defined as the time needed from the initial (stretched) shape to a stretched (initial) shape. Usually, a droplet stretched to a longer distance leads to a longer expanding and recovering time. Here we measured the switching time when the droplet was stretched to $\sim 3X$ at $60 V_{\text{rms}}$. Since the droplet aperture ($\approx 800 \mu\text{m}$) is small, it cannot block the beam (in x-direction) even when it is extremely stretched. Therefore, we add a special black mask on the top substrate of the cell, in which only the area where the droplet travels through is transparent, as shown in Figure 4.11(a) and Figure 4.11(b).

At $V=0$, a collimated and expanded He-Ne beam passes through with the highest transmittance $\approx 74.6\%$. At $60 V_{\text{rms}}$ (500 Hz) burst, the stretched droplet covers the whole transparent area, and the transmittance reaches the minimum $\approx 0.88\%$. The contrast ratio is $\approx 83:1$. The expanding and recovering time were measured as 260 ms and 500 ms, respectively, as shown in Figure 4.11(c). The corresponding travel speeds are estimated to be $\sim 6.1 \text{ mm/s}$ and $\sim 3.2 \text{ mm/s}$, respectively. Such results are comparable to electrofluidic displays ($\sim 2.65 \text{ mm/s}$) [106]. The short delay in the transmitted light intensity (the curve in the pink circle) may result from the size mismatch between the black mask and the stretched droplet. The length of the stretched

droplet may be slightly longer than that of the transmitted area of the black mask (l). The cycle driving with two periods shows that the LC droplet returns to its original state quite well.

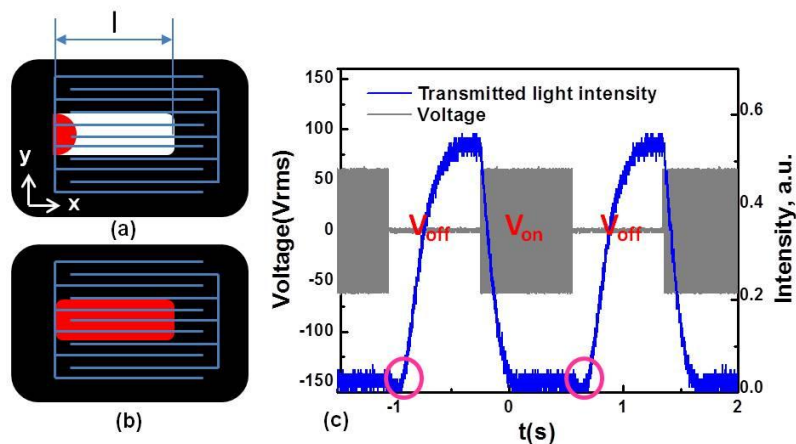


Figure 4.11: Measurement of the switching time.

Due to the facility limitation in our lab, the smallest droplet (or the smallest hole pattern on the Teflon layer) we can fabricate is $\approx 500\mu\text{m}$. Since a typical sub-pixel size of LCD is $\sim 240\mu\text{m} \times 80\mu\text{m}$, an $80\text{-}\mu\text{m}$ -aperture LC droplet would cover the whole sub-pixel when it is stretched to 3X. Under the same travel speeds, the expanding and recovering time would be reduced to $\sim 26\text{ ms}$ and $\sim 50\text{ ms}$. To work in a reflective mode, a mirror was added as the reflector to the bottom substrate and the reflectance was measured to be $\sim 60\%$ (without AR coating).

We also demonstrated a red and blue pixel switch for color displays. In a conventional transmissive color LCD, the color is displayed by the embedded color filters [107]. To achieve color filter free, we adopted dye-doped LC droplets [100,108]. They are doped with 1.5 wt% blue dye (M-137, Mitsui Toatsu Dyes) and 1.2 wt% red dye (Oklahoma dyes C10) respectively. Their aperture is $\approx 500\text{ }\mu\text{m}$, and the cell gap is $\approx 400\text{ }\mu\text{m}$. At $V=0$, the two droplets have the smallest surface-to-volume ratio (Figure 4.12(a)). They show a dark color due to the strong

absorption from the thick LC layer. As the voltage increases, they are gradually stretched, and the dispersion at 35 V_{rms} and 50 V_{rms} are shown in Figure 4.12(b) and Figure 4.12(c), respectively. The color becomes brighter when the thickness of the LC layer is gradually reduced by stretching.

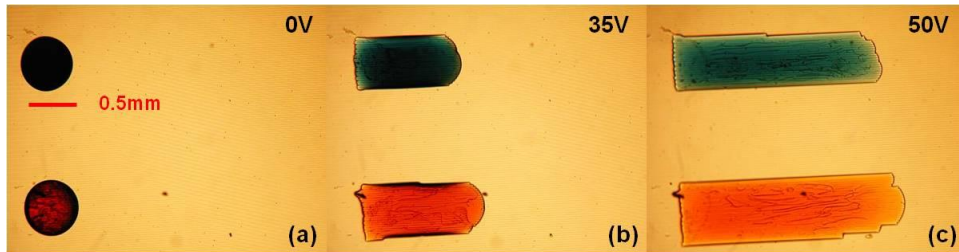


Figure 4.12: Droplet deformation (blue and red pixels) at various voltages.

Due to the molecular structure difference in doped dyes, the blue and red droplets have slightly different stretches at the same applied voltage. Even for one droplet, it is not uniformly stretched along the stripe direction. Because some dyes are not very well dissolved in the LC, some residual dye clusters form bumpers on the bottom substrate. Besides, a uniform Teflon coating is critically needed in order to achieve a uniform droplet stretching. Compared to the abovementioned black droplet, these two colored droplets with smaller apertures need a lower voltage to achieve similar aperture ratio. The operating voltage for an 80- μm -aperture LC droplet will be even lower.

We also demonstrated a 1×6 colored droplet array. The droplet aperture is $\approx 500\mu\text{m}$, and the cell gap is $\approx 400\mu\text{m}$. A top view of the cell at $V=0$ is shown in Figure 4.13(a), and the switching at 50 V_{rms} is shown in Figure 4.13(b). In practical application, a large-scale droplet array is required. These droplets should be separated by a patterned grid (such as black matrices)

to avoid the crosstalk. How to fabricate a uniform hole-array on a thin Teflon layer as well as dispensing uniform droplets into the holes is still a challenge.

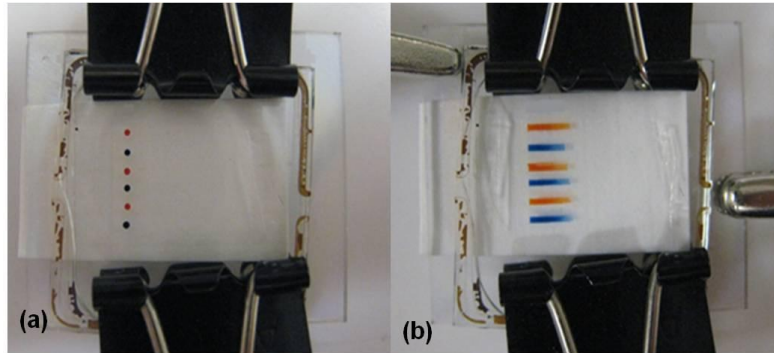


Figure 4.13: 1×6 droplet array switching

From the above experimental results, the selected ZLI-4389 material plays a key role in our device. Such a LC material exhibits a high dielectric constant and medium surface tension. Therefore, the droplet can be largely stretched by a relative low voltage. Otherwise, the droplet deformation will be very limited even under a very high voltage [28,32,33,109,110]. In our device, the electric field penetration depth is quite small (less than $10 \mu\text{m}$ at the highest voltage), and most LC in its bulk is randomly orientated. In this case, the device is polarization insensitive. To further decrease the operating voltage, interdigitated ITO electrodes with a smaller electrode gap can be considered. To further enlarge the aperture ratio, a zigzag striped electrode can be adopted, thus the droplet will be stretched in both elongated and sidewise directions [35]. The contrast ratio depends on the thickness of the area covered by LC and the dye concentration. A higher dye concentration will lead to a larger absorption even though the stretched LC layer is thin. The response time is governed by the liquid interfacial tension, flow viscosity, as well as travel distance. Surrounding liquid with low viscosity helps to improve the travel speed.

4.2.2 Variable Optical Attenuator Based on Dielectrically Stretched Liquid Crystal Droplet

Variable optical attenuator (VOA) has been widely used in fiber-optic communication, photonic signal processing, sensing as well as testing instruments. Various approaches have been proposed in the past years. MEMS VOAs [111,112] have a microsecond response time, but the microshutters (or the reflective micromirrors) bring up the reliability issue and it is difficult to integrate with other planar optical elements. Microfluidic VOAs alter the refractive index of the fluid within microchannels to control the beam reflection or refraction [113,114]. They are attractive for easy in-plane integration and biochemical sensing, but the inconvenient driving scheme and fabrication procedures (one step or multistep photolithography and soft lithography) limit their applications. VOAs based on LCs [115-122], DEP effect [33,34,79] and electrowetting [17,22,41] have no moving parts. Nematic liquid crystal VOAs have the advantages of low cost, low optical loss, low power consumption, and grayscale capability, but the response time is relatively slow [115-117] and most of them are polarization dependent. Polymer-network liquid crystal (PNLC)-based VOAs exhibit a fast response time at room temperature, but they show strong light scattering and need a relatively high operating voltage [118,119]. On the other hand, sheared PNLC has lower driving voltage and negligible light scattering, but the mechanical shearing process adds fabrication complexity [120]. Polymer-dispersed liquid crystal, in principle, is polarization independent, but to keep a large dynamic range and a small polarization dependent loss (PDL) simultaneously is a challenging task [121,122]. Most DEP [33,34,79] and electrowetting [17,22,41] VOAs only work in the visible spectral region. For fiber communications, an electrowetting lens-based broadband VOA has been reported [41]. This device adopts an electronically controlled optical wedge to vary the tilt

angle of the output beam which in turn changes the coupling efficiency. It shows broadband operation at C-Band, ~40 dB dynamic range, 0.3 dB PDL and <100 ms switching time, but the insertion loss is ~4.3 dB.

In this chapter, we will demonstrate a VOA based on dielectrically stretched LC droplet for C-Band operation. It utilizes a stretchable LC droplet to deflect the incident beam. In the voltage-off state ($V=0$), the beam passes through the VOA without any deflection. As the voltage increases, the LC droplet surface is gradually stretched by the dielectric force, which deflects the incident beam leading to the attenuated transmission. The demonstrated VOA shows broadband operation over the C-Band (1530-1560 nm), and ~32 dB dynamic range, ~0.7 dB insertion loss, ~0.3 dB PDL and ~20 ms switching time at $\lambda=1550$ nm. The peak operating voltage is $\sim 40V_{\text{rms}}$.

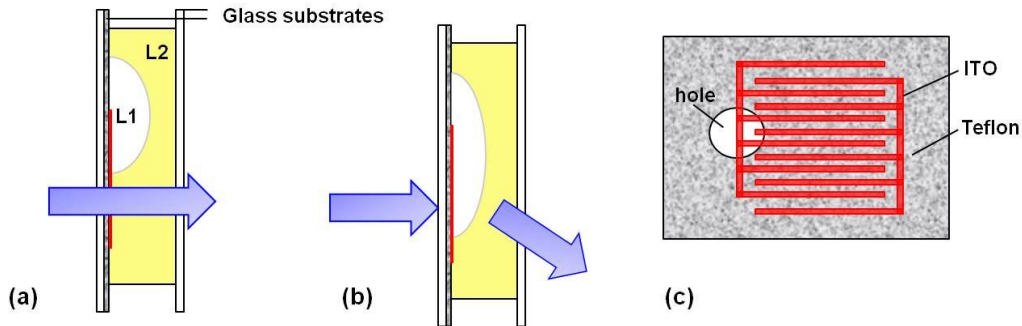


Figure 4.14: (a) Side-view structure of the VOA at $V=0$, (b) $V>0$, and (c) the layout of the interdigitated ITO electrode and Teflon layer on the bottom substrate (The size of the hole and the width of electrode strips are not drawn by scale.)

Figure 4.14(a) shows the side-view structure of the proposed device. It is very similar to that shown in Figure 4.8 and same liquids are employed. The only difference is that the surrounding liquid is transparent without any dye clusters. The aperture (the diameter of the touching area on the bottom substrate) and apex distance of the droplet is $\sim 450 \mu\text{m}$ and $\sim 200 \mu\text{m}$,

respectively. The cell gap is $\sim 270 \mu\text{m}$. The width and gap of the interdigitated ITO electrodes are both $10 \mu\text{m}$.

The incident beam from a single mode fiber (SMF) is intentionally adjusted to pass near the droplet's border, where a maximum change in the droplet's surface occurs, as Figure 4.14(a) shows. At $V=0$, the droplet shrinks in the hole with the smallest surface-to-volume ratio. The incident beam stays aligned with the output SMF for a maximum coupling and the smallest attenuation. When a voltage is applied to the bottom electrodes, as we have explained in Chapter 4.2.1, the LC droplet will be stretched outward along the electrodes by the dielectric force. As a result, the incident beam will be deflected when it hits the stretched droplet's surface, leading to a decreased coupling with the connecting SMF, as Figure 4.14(b) shows. Upon removing the voltage, the droplet will quickly return to its original state because of the interfacial tension.

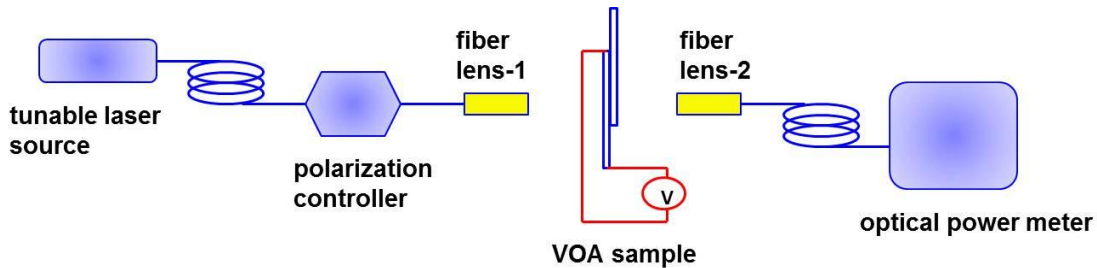


Figure 4.15: Experimental set-up for characterizing the VOA sample.

Figure 4.15 shows the experimental set-up for characterizing the VOA sample. The free-space beam from a tunable laser light source (ANDO AQ4321D, $\lambda = 1.52\text{-}1.62 \mu\text{m}$) propagates through the input SMF. Its polarization state is manually adjusted by a fiber polarization controller (FPC560, Thorlabs). After being collimated by the fiber lens-1, the beam propagates to the fiber lens-2 and the connected output SMF. The output beam is monitored by an optical power meter (ANDO AQ8201-21). The fiber lenses are gradient index (GRIN) type devices

enabling a near zero free-space-to-SMF coupling loss with the self imaging configuration [123]. The distance of the two GRIN lenses was fixed at ~ 4 cm. The VOA sample was vertically placed between them. The incident beam from lens-1 passed the edge of the liquid droplet.

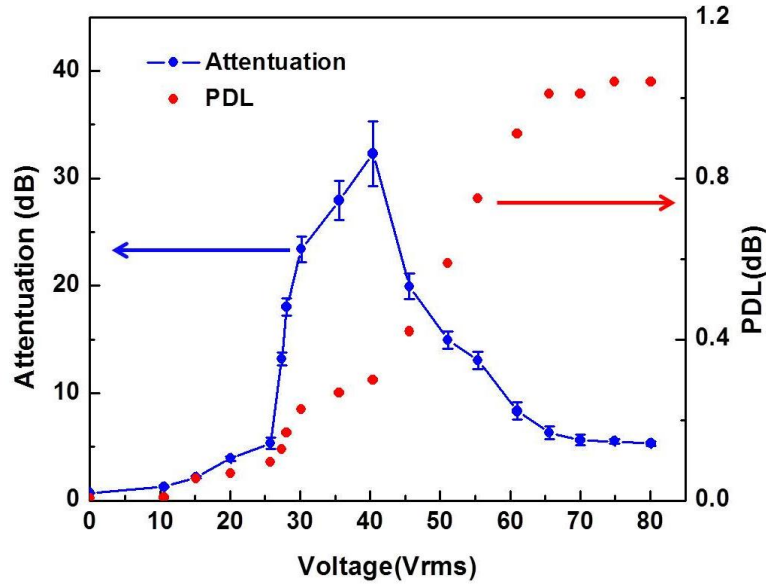


Figure 4.16: Measured attenuation and PDL vs. operating voltages ($\lambda=1550\text{nm}$).

Figure 4.16 shows the measured voltage-dependent attenuation and PDL of the VOA sample at 1550 nm. At $V=0$, the beam propagated through the cell with a ~ 0.7 dB insertion loss and ~ 0 dB PDL. As the voltage increases, the attention first increases and reaches a maximum value of ~ 33 dB at $V=40.4$ V_{rms} . Thus, the dynamic range is ~ 32 dB. As the voltage keeps increasing, the attenuation gradually decreases to ~ 5.32 dB at $V=80$ V_{rms} . The reason for the observed phenomena is explained as follows. At $V=0$, the incident beam stays aligned with the output SMF for the smallest attenuation (Figure 4.17(a)). When the voltage is high enough, the LC droplet begins to stretch along the electrodes by the dielectric force. As a result, it gradually covers the incident beam. Instead of propagating through a pure silicone oil (L2) layer, the beam goes through the LC droplet and silicone oil sequentially. Due to the refractive index mismatch

between these two liquids, the liquid-liquid interface deflects the incident beam away from the output SMF (Figure 4.17(b)-(c)). Thus, the attenuation increases accordingly, and it reaches a maximum when the output beam is totally decoupled from the output SMF (Figure 4.17(d)). However, further increasing the voltage will reduce the beam deflection and lower the attenuation, because extremely stretching the droplet will lead to a flatter liquid-liquid interface in the beam path (Figure 4.17(e)-(f)). From the above discussion, we can see that the most effective working window for the proposed VOA is that shown from Figure 4.17(a) to Figure 4.17(d).

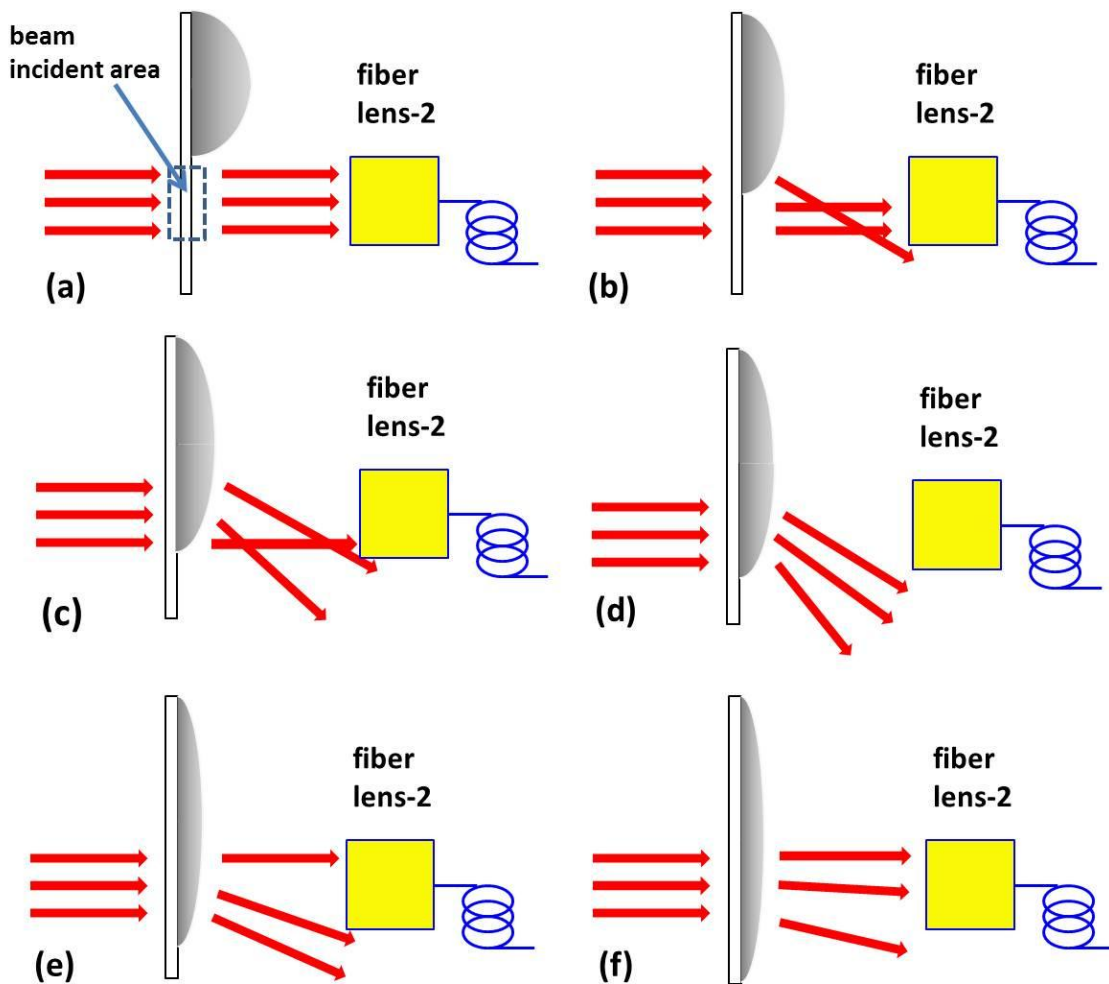


Figure 4.17 . Droplet surface stretching and beam deflection with increased voltage.

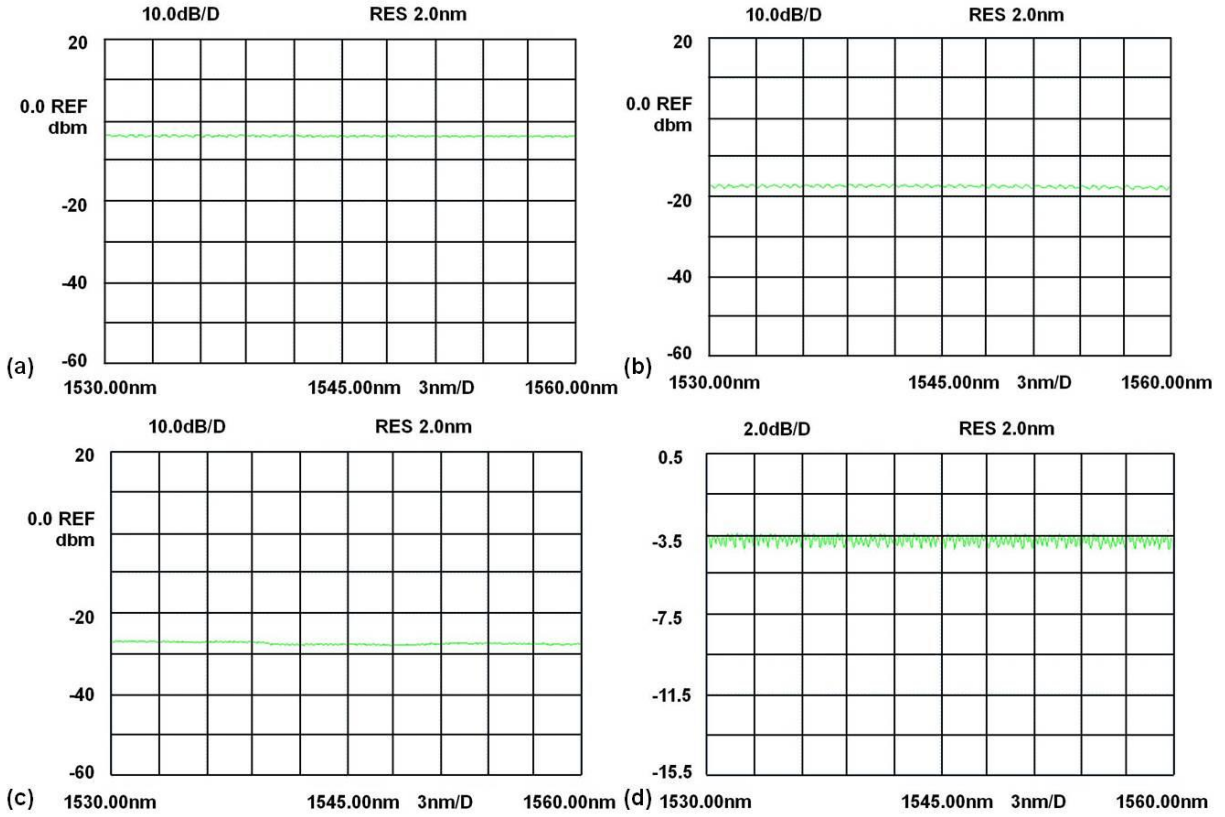


Figure 4.18: Measured VOA broadband operation at (a) $V=25V_{rms}$ ($\sim 5\text{dB}$ attenuation setting), (b) $V=30V_{rms}$ ($\sim 20\text{dB}$ attenuation setting) and (c) $V=35V_{rms}$ ($\sim 30\text{dB}$ attenuation setting) for C-Band operations with OSA resolution of 10 dB/Div, and (d) measured high resolution VOA broadband response at $V=20V_{rms}$ ($\sim 3\text{dB}$ attenuation setting) with OSA resolution of 2 dB/Div.

As a comparison, the PDL keeps increasing with the operating voltage consistently. It is $\sim 0.3\text{ dB}$ at $V=40.4 V_{rms}$ and $\sim 1\text{ dB}$ at $V=80 V_{rms}$. PDL is induced by the birefringence effect of the LC material [124], and the acceptable PDL for VOAs should be less than 0.5 dB within the 0-10 dB range. As the voltage increases, more LC molecules are reoriented along the electric field so that the PDL increases correspondingly. In the proposed VOA, the LC droplet is quite large (aperture $\sim 450\ \mu\text{m}$, apex distance $\sim 200\ \mu\text{m}$). Thus, even at $40V_{rms}$ only a very thin LC layer (very close to the bottom substrate) is affected by the electric fields, while the bulk LC

molecules are still randomly oriented. Therefore, our device keeps a small PDL at the effective working window.

Figure 4.18 (a)-(c) shows the broadband VOA operation with an attenuation setting of 5 dB, 20 dB and 30 dB for the telecommunication C-Band (1530 - 1560 nm) respectively. The OSA (Optical Spectrum Analyzer) resolution is 10 dB/Div. The attenuation at a given voltage is quite inert to the operating wavelength. Figure 5(d) shows the broadband VOA operation for the attenuation settings of ~3 dB with a higher OSA resolution (2 dB/Div). The maximum in-band attenuation variation is measured to be ± 0.124 dB. The small oscillations of each curve may come from the interference of the two substrate surfaces.

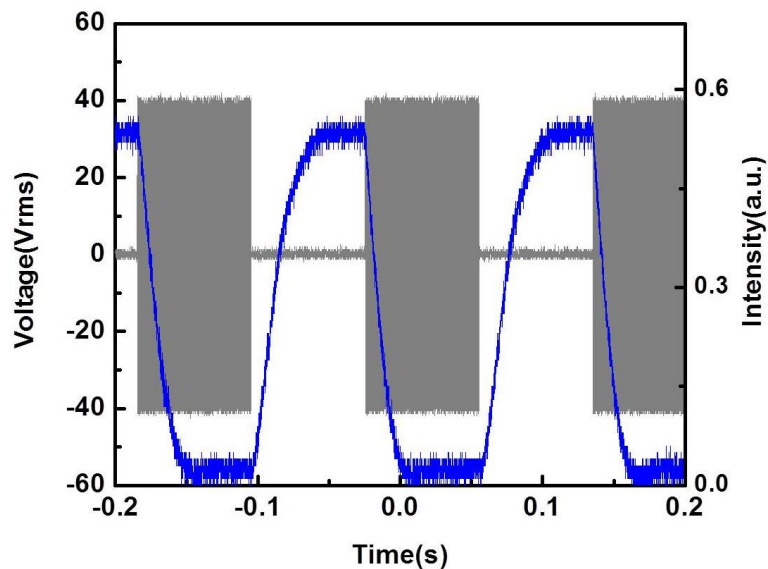


Figure 4.19: Measured switching time at $V=40V_{rms}$ ($\lambda=1550nm$).

Response time is another important issue for a VOA. Due to the facility limitation, instead of using the experimental set-up shown in Figure 4.15, we adopted a 1550nm laser diode (LAS DFB-1550, LaserMax), photo-receiver (Model 2031, New Focus) and oscilloscope (TDS 3032B, Tektronix) in our measurement. The response time was measured by monitoring the

time-dependent transmitted light intensity. At 40 V_{rms} (500Hz) square voltage bursts, the fall (droplet stretching) and rise (droplet recovering) times were measured to be ~19.2 ms and 26.2 ms, respectively, as shown in Figure 4.19.

The dynamic range can be enlarged by adopting two liquids with a larger refractive index difference. The insertion loss can be reduced by using AR coating and high quality Teflon layer on the glass substrates. The PDL can be further reduced by increasing the droplet size (especially the apex distance of the droplet), but this will lead to a larger insertion loss since the cell gap is increased. The switching time is affected by the liquid interfacial tension and flow viscosity, and it can be improved by using a surrounding liquid with lower viscosity.

4.3 Optical Switch Based on Variable Aperture

An intensity modulator based on a stretchable LC droplet has been demonstrated in Chapter 4.2 [35,38]. To obtain a large aperture change, the stretched droplet should travel a long distance so that a large area can be covered. Accordingly, when the droplet is relaxed, it will travel the same distance to return to its original shape. Largely stretching the surface of a droplet will cause two problems: high operating voltage due to the large stretching, and slow response due to the long distance travel.

In Chapter 4.3, we will discuss an optical switch based on variable aperture. Figure 4.20 shows the device structure and the surface stretching of a ring-shaped liquid droplet at various voltages. The cross-sectional structure of the pixel is shown in Figure 4.20(a). It consists of a bottom glass substrate, interdigitated ITO electrodes, a polymer hole, a ring-shaped liquid droplet, and a top glass substrate. Both substrates are coated with Teflon ($\gamma \sim 18$ mN/m), Figure

4.20(b) shows the top-view structure of the pixel, which is confined by a polymer hole. A liquid forms a ring shape on the inside wall of the polymer hole due to the super hydrophobic Teflon layer coated on the top and bottom substrates. At $V=0$, the pixel has the maximum aperture. When a voltage is applied to the electrode, the surface of the liquid is stretched towards the center of the opening by the dielectric force [35,38], causing the aperture of the pixel to decrease, as shown in Figure 4.20(c) and Figure 4.20(d). Upon removing the voltage, the stretched liquid returns to its initial state. Instead of stretching along one direction, the ring-shaped liquid stretching along radial direction exhibits a relatively fast response time (~ 10 ms) and high aperture ratio ($\sim 80\%$). Moreover, the proposed device has following advantages: simple structure, easy fabrication, and good mechanical stability. For a large area optical switch or display, we can simply build a two-dimensional pixel array.

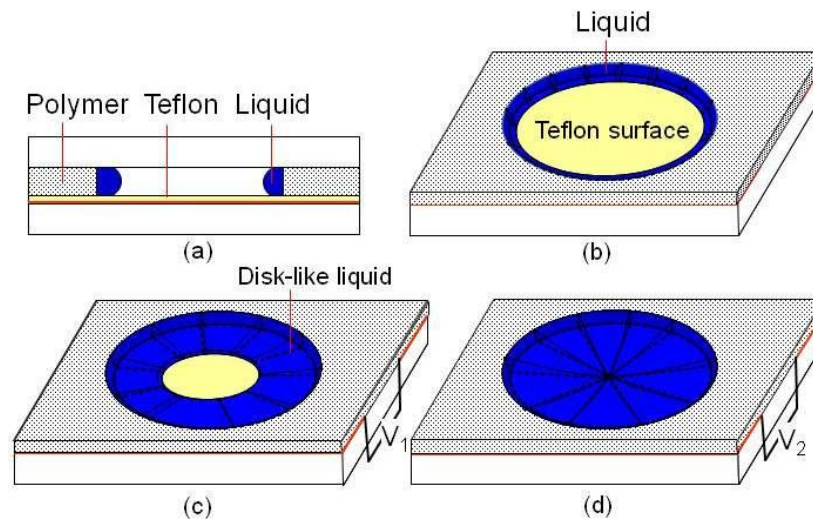


Figure 4.20: Device structure and the surface stretching of a ring-shaped liquid droplet at various voltages.

To demonstrate the proposed optical switch, we prepared a liquid cell according to the fabrication procedures depicted in Figure 4.21. Firstly, a UV curable monomer, such NOA65 ($\gamma \sim 40 \text{ mN/m}$), was spread on a thin glass substrate using a steel blade (Figure 4.21(a)). Secondly,

the film was exposed to UV light through a photomask (Figure 4.21(b)). Thirdly, the uncured monomer was completely rinsed off with ethanol and a solid hole-patterned polymer film was obtained (Figure 4.21(c)). Then the film was peeled off and tightly stacked to another glass substrate, which was already coated ITO electrode and a thin Teflon layer (Figure 4.21(d)). To generate fringing fields, interdigitated ITO electrodes with 10- μm width and 10- μm gap was adopted. Then the holes were filled with a suitable liquid, which was mixed with a solvent (such as dichloromethane) (Figure 4.21(e)). The solvent serves for two purposes: it decreases the surface tension of the liquid and controls the amount of the liquid in the hole. After evaporation, a tiny amount of liquid was retained in each hole. Due to the uniform attraction of the polymer wall surface and the super hydrophobic Teflon layer on the substrates, it forms a ringed shape (Figure 4.21(f)). To prevent any liquid leakage, the top surface of the polymer hole array was tightly sealed by another Teflon-coated glass substrate (not shown here).

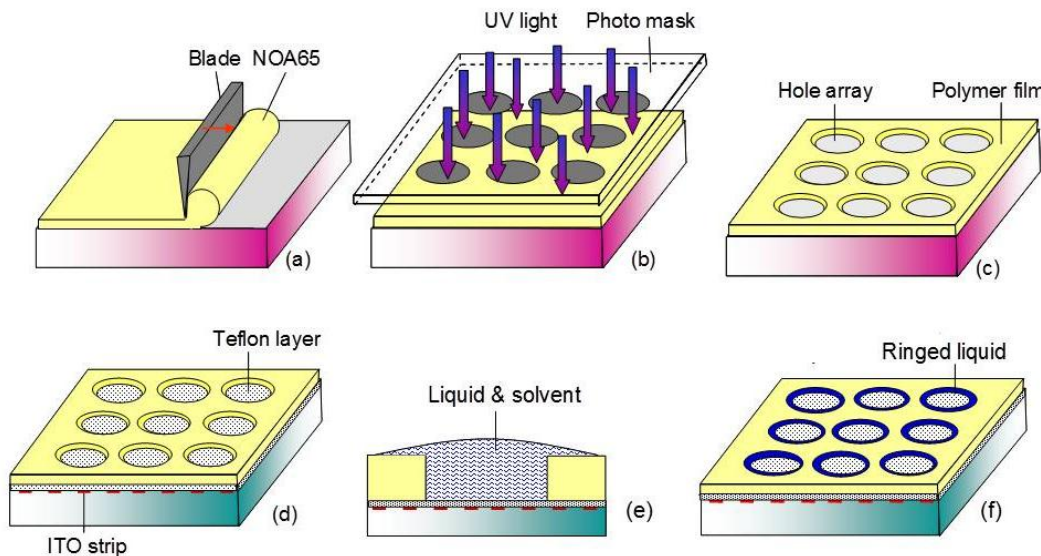


Figure 4.21: Fabrication procedure of an optical switch with bracelet-like liquid on the polymer wall surface of each pixel hole

Based on the abovementioned procedures, a hole-array polymer film was prepared. Each hole exhibits an octagon shape and its aperture is ~ 0.23 mm. The thickness of the polymer film is ~ 0.2 mm. Nematic LC Merck ZLI-4389 was chosen as the liquid because of its large dielectric constant ($\epsilon_r=56$, $\Delta\epsilon=45.6$) and medium surface tension ($\gamma\sim 38$ mN/m). To easily prove the aperture change, the LC was mixed with 1.5 wt% red dye (C10 Oklahoma dyes). Dichloromethane was used as the LC solvent, and the LC concentration was ~ 15 wt% before evaporation.

Figure 4.22 depicts the aperture change under various voltages. At $V=0$, the central area of the pixel is clear and a dark ring is formed around the aperture edge (Figure 4.22(a)). It is mainly caused by the absorption of the dye and deviation of the curved liquid surface. When a voltage is applied to on the bottom substrate, nonuniform fringing fields are generated across the ITO stripes, and the ringed LC experiences a dielectric force. The force stretches the LC molecules along the ITO stripe direction. Due to the adhesive force between LC and polymer wall as well as the cohesive force between adjacent LC molecules, the surface of the LC begins to spread. At $V=45V_{rms}$, the LC ring expands as Figure 4.22(b) shows. As the voltage keeps increasing to $54V_{rms}$, the LC spreads further toward the center of the pixel (Figure 4.22(c)). The reduced aperture is not quite circular because the dielectric force exerted on the LC ring is asymmetrical. The force along the ITO stripe is larger than that along the perpendicular direction. At $60 V_{rms}$, the opening area shrinks largely (Figure 4.22(d)) and at $65V_{rms}$ it is almost closed (Figure 4.22(e)). Finally at $70 V_{rms}$, the whole aperture is covered by the LC (Figure 4.22(f)). Due to the large expansion of the LC ring, the dark area at the aperture border is significantly decreased in comparison to that observed in Figure 4.22(a). After removing the voltage, the

stretched LC surface returns to its original shape (Figure 4.22(a)) because the bottom Teflon surface cannot hold the LC layer in the hole area.

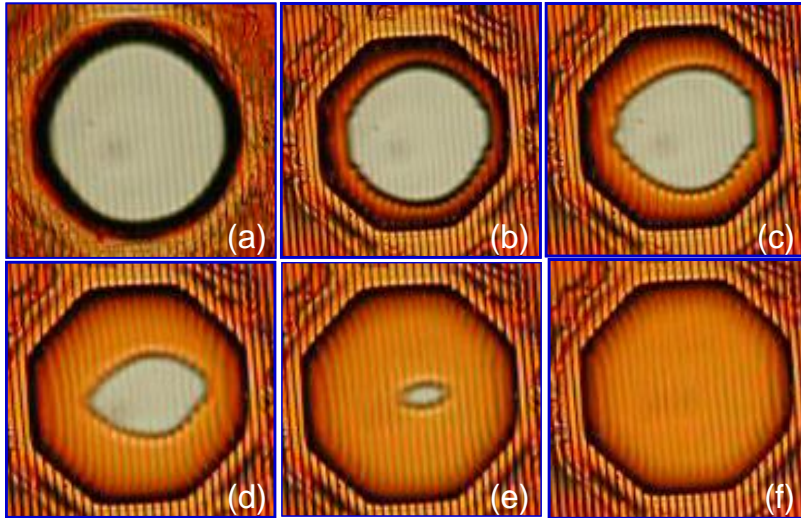


Figure 4.22: The aperture of a pixel changed with different voltages.

For two-dimensional optical switches and displays, a pixel array is desirable. The density of the pixel is dependent on the pattern of the employed photomask. The polymer matrix is mixed with ~1 wt% black dye (S-428 Mitsui) in order to obtain a dark background. To demonstrate a color light switch, we filled the holes with a red dye-doped LC. Figure 4.23(a) (upper left) shows 3×3 pixels at $V=0$. For each pixel, the transmittance reaches the highest at $V=0$. As the voltage increases to $80V_{rms}$, each aperture is closed and a reddish color is observed, as Figure 4.23(a) (upper right) shows. Due to the defects of some ITO stripes, light leakage (short white bars) in some pixels is observed, which indicates the LC surface in those areas is disconnected. Once the voltage is removed, these stretched liquids with defect can quickly and safely recover to their original states. While the pixel (in the top left corner) was totally covered by the LC cannot return to its original state quickly. It has to wait for some time until the LC surface breaks up by itself. As a result, its response speed is slow.

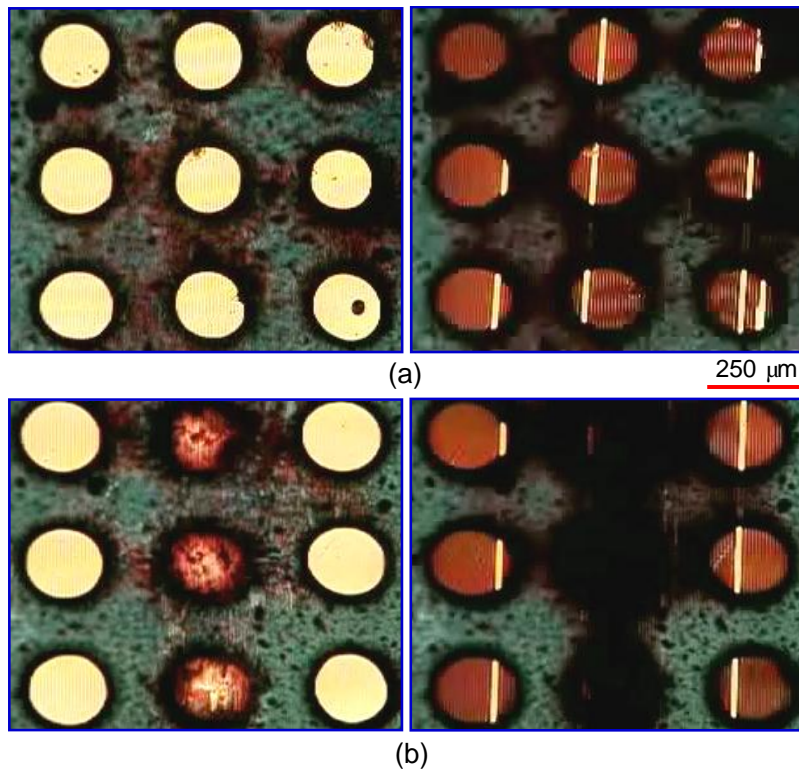


Figure 4.23: Hole array at (a) $V=0$ (left sub-figure) and $V=80 V_{rms}$ with or without surface defects (right sub-figure), and (b) $V=0$ (left sub-figure) and $V=80 V_{rms}$ with normally filled or excessively filled LC (right sub-figure, the holes in middle column are excessively filled).

To form a LC ring, the amount of LC filled in each hole should be properly controlled. Figure 4.23(b) shows another 3×3 pixel array filled with different filling amounts of LC: the pixels in the left and right columns with normal filling and that in the middle column with excessive filling. At $V=0$, the pixels in the left and right columns show the highest transmittance. While for the pixels in the middle column, their apertures are totally covered by the LC, which indicates these holes are filled with too much LC. At $V=80V_{rms}$, pixels in the left and right columns are covered by the expanded LC surface except some defect segments. While pixels in the middle column become even darker. Although the LC can still be reoriented by the voltage, they do not switch light. On the contrary, if the LC filling is insufficient, then a higher voltage is

required to make it expand and cover the hole aperture. Moreover, the formed LC layer in the aperture will be too thin to effectively switch the light.

From Figure 4.22(a), the amount of LC in the hole can be roughly estimated. Here the aperture is $\sim 230 \mu\text{m}$ and the width of LC ring is $\sim 22 \mu\text{m}$. If the thickness of aperture is equal to that of the LC ring, then the LC occupies $\sim 20\%$ of the hole space. That means the maximal aperture ratio is $\sim 80\%$. Increasing the LC volume in the hole will decrease the aperture ratio. Thus, the tradeoff between aperture ratio and operation voltage needs to be taken into account when optimizing the device performance.

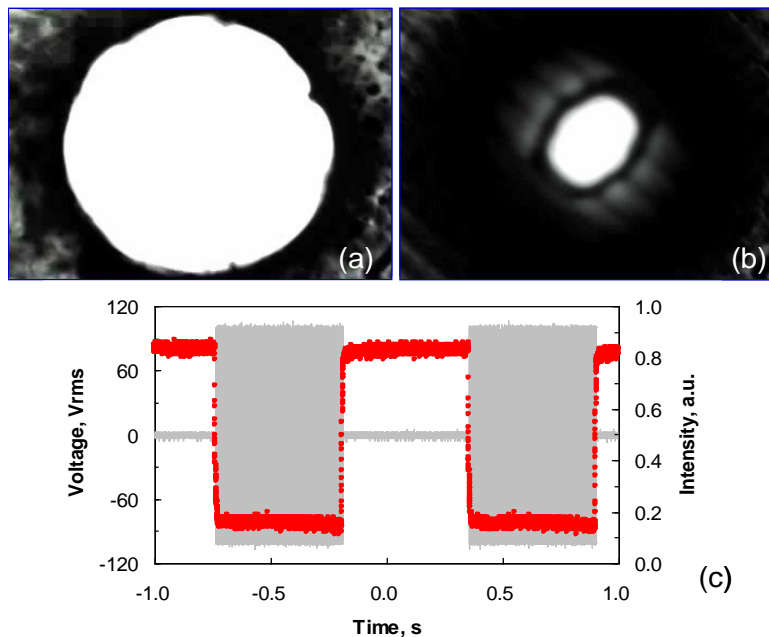


Figure 4.24: Aperture change of a pixel filled with black LC. (a) $V=0$, (b) $V=80 V_{\text{rms}}$, and (c) time dependent transmitted light intensity.

To switch white light, we filled some pixels with black dye-doped LC (~ 1.5 wt% black dye). Figure 4.24(a) and Figure 4.24(b) show the aperture change of one pixel at $V=0$ and $V=80 V_{\text{rms}}$, respectively. At $V=0$, the aperture has a maximum opening and the transmittance is the

highest. At $V=80 V_{\text{rms}}$, the aperture is narrowed down dramatically and transmittance is reduced. The dynamic response of the pixel is shown in Figure 4.24(c). Two cycles (red lines) show the time-dependent transmitted light intensity. The stretching and recovering times are measured to be ~ 10 ms and ~ 10 ms, respectively.

Although only LC is employed in the pixels, their electro-optic properties are stable even when the cell is placed in vertical position. One reason is that the LC cannot wet the top and bottom glass substrates due to the low surface tension of Teflon layer on the substrate, thus it only adheres tightly to the inside wall of the chamber. Furthermore, because of the small LC amount in each chamber, the gravity effect is negligible when the surface tension plays the major role. Given the polymer film is ~ 0.2 mm thick, the thickness of the stretched LC layer is estimated to be $\sim 40 \mu\text{m}$ at $V=80V_{\text{rms}}$. Since the electric field penetration depth is quite small, most LC molecules and black dyes in such a thick layer are hardly reoriented by the fringing field and still randomly orientated. Therefore, the proposed optical switch is polarization insensitive.

4.4 Optical Switch at 1550nm Based on Position-shifting Liquid Droplet

Fluidic optical switch is an attractive device for light shutter, variable optical attenuator, adaptive iris, and display. Various optical switches, such as polymer-dispersed liquid crystal (PDLC) [121,125-127], microfluidic [128,129], electrowetting [17,19,22,41,100], and dielectrophoretic effect [30,33-35,78] have been developed. However, most of these approaches are aimed for visible light and very few are suitable for IR applications [130].

PDLC, which controls the incident light by scattering, has been proposed for IR light switch [121]. PDLC has some advantages, such as polarization independence, simple structure, and easy fabrication. But because of the forward scattering, its optical attenuation is very sensitive to the distance between the device and the detector. Microfluidic devices have also been demonstrated to modulate IR light. Liquid flows into microchannels under a pressure and IR light is switched by manipulating the liquid's position. However, such a device requires a mechanical driving system [128] or a complicated fabrication procedure [129] or both. Electrowetting devices steer the IR light either by the total internal reflection from a mercury slug [17] or by the deflection from a tunable liquid-liquid interface [41] With rapid development in optical communications, IR light switch has become a key component for regulating the optical power in an optical system. Therefore, it is highly desired to develop a high performance IR light switch.

In this chapter, we demonstrate an IR light switch with a glycerol droplet. In comparison to conventional liquids, glycerol has two unique merits: high absorption at 1.55 μm and large dielectric constant. The former enables the glycerol droplet to evade or block the incident IR beam effectively, while the latter helps to lower the operation voltage. By using a 4.5-mm diameter glycerol droplet, we have demonstrated an IR light switch with $\sim 95:1$ contrast ratio and ~ 200 ms response time.

Figure 4.25(a) shows the cross-sectional structure of the liquid cell at $V=0$. Two immiscible liquids are sandwiched between glass substrates. One liquid (L1) forms a droplet and the other liquid (L2) fills the surrounding. The two liquids are density matched, thus the gravity effect during the droplet shifting is negligible when the cell is placed in vertically direction. Moreover, L2 helps to enhance the mechanical stability of the device, in case of shaking or

vibrating. To actuate the droplet, the inner surface of the bottom glass substrate is coated with interdigitated electrodes (marked in red), followed by a thin dielectric layer (PI2556, from HD Microsystems, surface tension $\gamma_P \sim 40$ dynes/cm, marked in green) and a thin Teflon layer (marked in shades) sequentially. A hole, partially contacting with the edge of the striped electrodes, is patterned on the Teflon layer, pinning down the droplet position at the relaxed state. Both the PI layer and Teflon layer help to prevent the carrier injection from the electrodes, because of their high dielectric breakdown voltage and low leakage density. Due to the low surface tension of Teflon, the droplet exhibits a minimal surface-to-volume ratio on the Teflon surface.

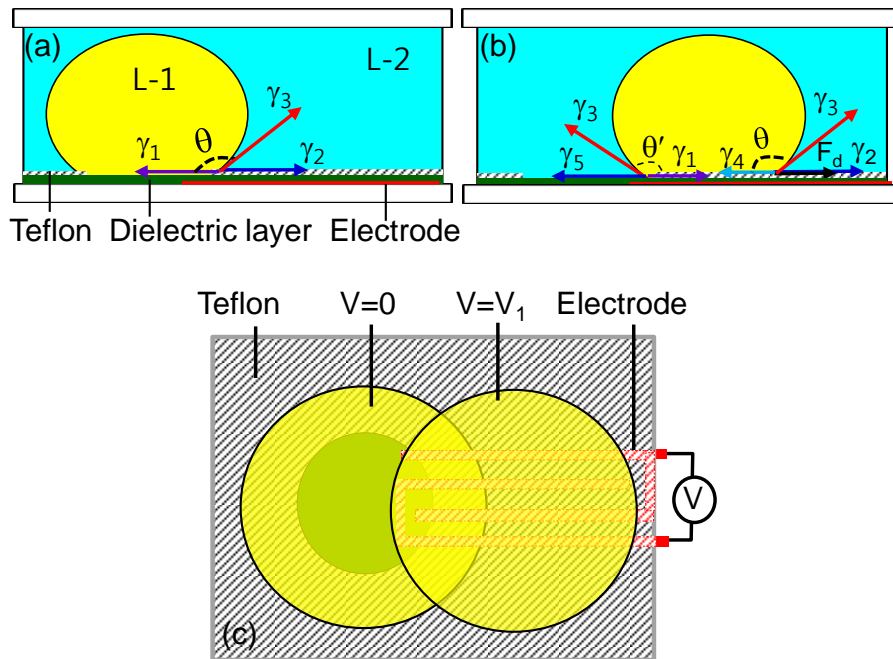


Figure 4.25: Schematic structure of the cell and its operation mechanism. (a) The droplet pinned down on the hole surface at $V=0$, (b) the droplet moved to the right side at $V=V_1$, and (c) the top view showing the position of the droplet at $V=0$ and $V=V_1$. The droplet size and electrode dimensions are not drawn by scale

For a stable droplet without any external force, the interfacial tensions should satisfy following relation [101]:

$$\gamma_1 + \gamma_3 \cos \theta = \gamma_2 \quad (4.4)$$

where γ_1 , γ_2 , and γ_3 denote the interfacial tension of L1/dielectric layer, L2/Teflon, and L1/L2, respectively, and θ is the contact angle of L1 on the Teflon surface. When a voltage is applied, the droplet experiences a dielectric force (also called Maxwell's stress) expressed by Eq.(4.2) [39,101]. The system balance shown in Eq. (4.4) is broken because of the dielectric force. If $\epsilon_{L-1} > \epsilon_{L-2}$, then the droplet is shifted rightwards to the region with high electric field intensity, as shown in Figure 4.25(b). When the whole droplet is pulled to the region with embedded electrodes, it will stop shifting because the left side and right side of the droplet bears the same strength of the dielectric forces but in opposite directions. If the voltage is further increased, the droplet may be stretched along the striped electrodes in both directions, instead of being shifted only rightwards.

The motion of the droplet can be well explained based on the balance between the dielectric force and interfacial tensions. If the droplet reaches a stable state as shown in Figure 4.25(b), then along the ITO stripe direction, the system satisfies the following Eq. (4.5):

$$\gamma_1 + \gamma_2 + \cos \theta' \gamma_3 + F_d = \gamma_4 + \cos \theta \gamma_3 + \gamma_5 \quad (4.5)$$

where γ_4 and γ_5 denote the interfacial tension of L1/Teflon and L2/dielectric layer, respectively; F_d is the horizontal component of dielectric force and θ' is the contact angle of L1 on the PI surface. From Eq. (4.5), as F_d increases, γ_4 and θ will change accordingly before the whole droplet totally shifts to the region with embedded electrodes. If the surface tension of the droplet is very large, the change of θ is rather limited. Instead, γ_4 will be the main varying factor because

the droplet will go through a surface change from the dielectric layer surface to Teflon when it shifts rightwards. If $\theta \approx \theta'$, then Eq. (4.5) is simplified to Eq. (4.6)

$$\gamma_4 + \gamma_5 = \gamma_1 + \gamma_2 + F_d \quad (4.6)$$

When the voltage is removed ($F_d = 0$), the force balance in Eq. (4.6) is broken again. Since $\gamma_4 + \gamma_5 > \gamma_1 + \gamma_2$, the droplet will be pulled back to its original position by interfacial tensions. To further illustrate the device structure, Figure 4.25(c) depicts the top view of the device. Compared with the position at $V=0$, the shifted droplet at $V=V_1$ covers a new area in addition to the overlapped region. The alternation between the original state ($V=0$) and the shifted state ($V=V_1$) can be used for light switch.

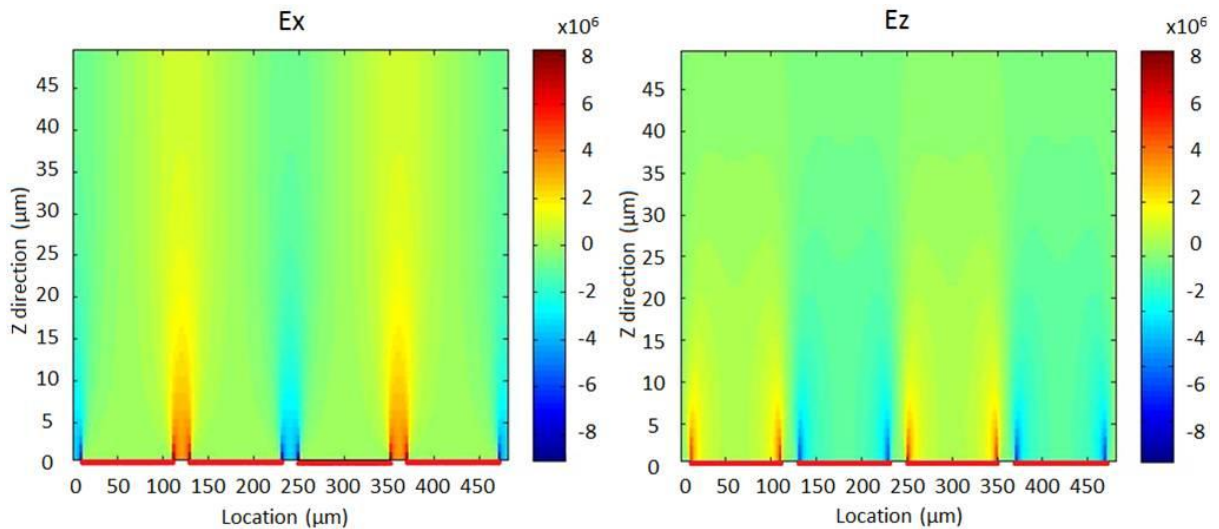


Figure 4.26: Simulated electric field distribution: (a) along x-axis and (b) along z-axis. The ITO electrode width is 100 μm , electrode gap is 20 μm , and the distance along z-axis to the electrode surface is 50 μm .

The device structure is not drawn by scale.

To generate fringing fields, we adopt ITO electrodes as Figure 4.25(c) shows. The electric field distribution is simulated (Techwiz software) using Cartesian coordinate system. The x -axis is perpendicular to the stripe and z -axis is perpendicular to the glass surface. The ITO

electrode width is 100 μm and electrode gap is 20 μm . The cell gap is 50 μm . Figure 4.26 shows the simulated electric field intensity distribution at $V=100\text{ V}_{\text{rms}}$. The electric field can be decomposed into two components: across the stripe E_x (left) and along the cell gap direction E_z (right). There is no electric field along the stripes (y -axis). The electric field is the strongest at the electrode edges but decreases quickly as the distance departs from the edge. Therefore, the droplet border bears the strongest dielectric force along the ITO stripes.

Table 4.3: Properties of liquid-1 (L1: Glycerol, Sigma-Aldrich) and liquid-2 (L2: SantoLight™ Optical Fluids SL-5267, Santovac® Fluids).

Material	Dielectric constant	Refractive index	Density (g/cm^3)	Color
L1	47	1.47	1.26	Clear
L2	5	1.67	1.25	Clear

In our experiments, two immiscible liquids Glycerol and SantoLight™ Optical Fluids SL-5267 are chosen as L1 and L2, respectively. Their properties are listed in Table 4.3. Since their densities match well, the gravity effect on shifting the droplet is minimized if the cell is vertically placed. Figure 4.27 shows the measured transmission spectra of the two liquids ($\sim 4\text{ mm}$ thickness). At $\lambda=1.55\text{ }\mu\text{m}$, L1 is opaque while L2 is transparent.

To prove concept, we prepared a liquid cell as depicted in Figure 4.25(a). A glass plate with interdigitated ITO stripes was adopted as the bottom substrate. The electrode width and gap are 100 μm and 20 μm ; the same as those we used in simulation. The ITO surface was firstly spin-coated with a PI layer ($\sim 1\text{ }\mu\text{m}$ thickness) and post baked at 270 $^\circ\text{C}$, followed by a Teflon layer ($\sim 1\text{ }\mu\text{m}$ thickness). We chose Teflon AF solution grade 400S1-100-1 (from DuPont) because of its excellent hydrophobic and dielectric properties [104]. After post-baking at 330 $^\circ\text{C}$

for 30 minutes, the Teflon layer was patterned with a 3.5-mm-diameter hole. The hole partially contacts with the electrode tips (Figure 4.25(c)). The area covered by Teflon exhibits a very low tension ($\gamma \sim 18$ mN/m) at room temperature. While the surface tension of the PI surface (hole area) is relatively high (~ 40 mN/m). After that, a small amount of glycerol was dispensed into the hole. Once the droplet border met the Teflon surface, it formed a spherical shape with a minimal surface-to-volume ratio. Then SL-5267 filled the surrounding of the droplet. The diameter of the droplet aperture (the touching area on the bottom glass plate) was controlled to be ~ 4.5 mm. Another glass plate was used as top substrate to cover the two liquids. The cell gap was controlled to be ~ 5 mm using glass spacers, and the periphery of the cell was hermetically sealed by adhesive glue. Such a distance is safe to prevent the dome of the droplet from touching the top glass plate.

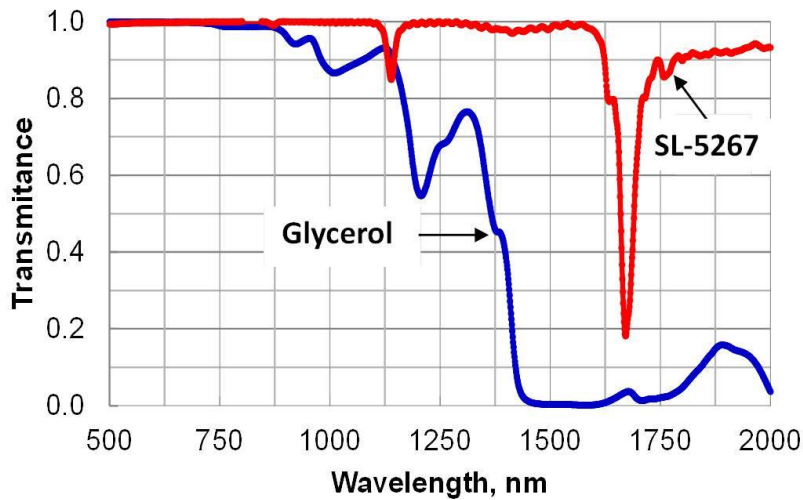


Figure 4.27: Measured transmission spectra of Glycerol and optical fluids (SL-5267) from 500 nm to 2000 nm. The thickness of each liquid is ~ 4 mm

To study the electro-optical properties of the droplet, we observed the cell using an optical microscope. Because the droplet size is fairly large, the microscope cannot focus well on

the entire droplet. At $V=0$, when focusing on the dome area of the droplet we observed a large bright spot (dome) surrounded by a black border (Figure 4.28(a)). As the voltage is gradually increased to $35 V_{\text{rms}}$, the bright spot begins to shift along the ITO stripes, implying that the whole droplet shifts along ITO stripes. At $45 V_{\text{rms}}$, the shifting of the droplet becomes more noticeable (Figure 4.28(b)). When the voltage is increased to $60 V_{\text{rms}}$, the droplet shifts dramatically (Figure 4.28 (c)). Upon removing the voltage, the droplet returns to its original state.

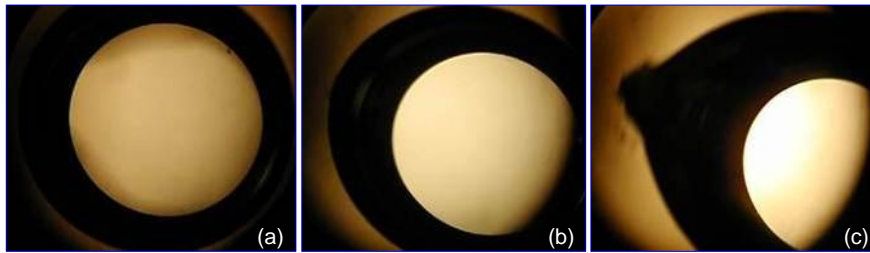


Figure 4.28: The position change of glycerol droplet at different voltages: (a) $V=0$, (b) $V=45 V_{\text{rms}}$, and (c) $V=60 V_{\text{rms}}$. The diameter of the droplet is ~ 4.5 mm.

According to the simulation results shown in Figure 4.26, at $V=100V_{\text{rms}}$ the peak electric field reaches as high as $8V_{\text{rms}}/\mu\text{m}$ at the ITO edges. Nevertheless, such strong field only distributes in the PI layer, whereas the field exerted on the glycerol droplet is relatively weak. The glycerol has a purity of $>99.5\%$ and the ionic impurity moving into the surrounding oil can be neglected. Besides, both PI layer and Teflon layer help to prevent the carrier injection into the cell. The breakdown field strength of a typical Teflon layer is $\sim 600\text{-}1730$ kV/cm, and that of a typical PI layer is $\sim 1.3\text{-}3.3$ MV/cm [131] [132,133]. Last but not least, AC rather than DC voltage operation also helps to suppress the charge effect. Therefore, even driven at $100 V_{\text{rms}}$ our device reproduces the droplet movement very well, as shown in the video.

Next, we evaluated the droplet's performance as an IR light switch at $1.55\mu\text{m}$. Figure 4.29(a) depicts a simple set-up for characterizing the electro-optical properties. The cell was

placed in vertical position. A laser beam (LAS DFB-1550-6, $\lambda=1.55 \mu\text{m}$, Laser Max) was normally incident upon the ITO electrode area and close to the border of the droplet at $V=0$. The diameter of the laser beam was controlled to be $\sim 4 \text{ mm}$ by an iris diaphragm, slightly smaller than that of the glycerol droplet. The transmitted light intensity was detected by a photodiode. At $V=0$ (the left sub-figure), the laser beam passed through the region filled with SL-5267, and the transmitted intensity was the highest. At $V=V_1$ (the right), the droplet shifted upward and blocked the laser beam. Figure 4.29(b) shows the transmitted light intensity at various voltages. At $V=35 \text{ V}_{\text{rms}}$, the light intensity starts to decrease, implying that the droplet begins to block the laser beam. At $V=100 \text{ V}_{\text{rms}}$, the light intensity is significantly decreased because the droplet almost blocks the incident laser beam. The measured contrast ratio exceeds $\sim 95:1$. The contrast ratio would be improved dramatically if the droplet could fully block the incident beam.

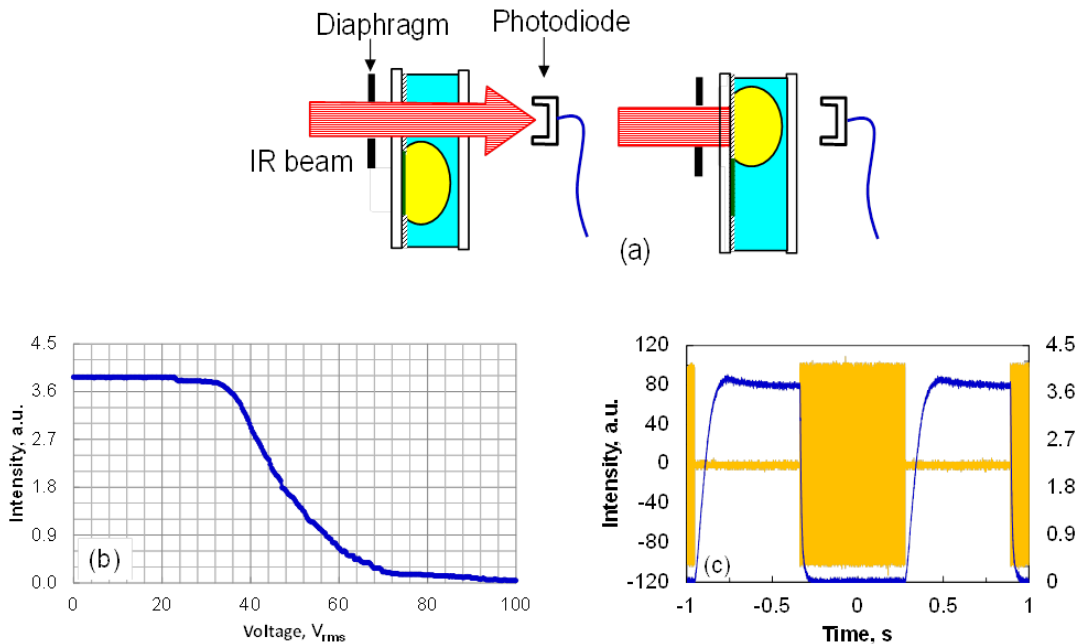


Figure 4.29: Electro-optical characteristics of the IR switch at $\lambda=1.55 \mu\text{m}$. (a) A simple set-up, (b) intensity change vs. voltage, and (c) intensity change vs. time.

Response time is an important parameter for an optical switch. To measure response time, we applied a square voltage pulse with 100 V_{rms} amplitude to the cell and recorded the time-dependent light transmission by a digital oscilloscope. Results are shown in Figure 4.29(c). The cycle driving with two periods shows that the dynamic switching of the droplet repeats very well. It takes ~80 ms for the droplet to largely block the laser beam and ~200 ms to return to its original place. Although the glycerol droplet switches the 1.55- μm laser beam by absorption, the heating effect is negligible because the laser power is weak (~4.5 mW). Moreover, the generated heat would be dissipated by the surrounding oil and the glass. Therefore, thermal effect is not a concern in our device. The power consumption of the device is less than ~1 mW under 1.5 kHz, while that of a typical electrowetting device is ~1W. This implies that our dielectric device exhibits much smaller current and fewer ions compared to electrowetting devices, further indicating that our device works well without the concern of charge effect.

From Figure 4.25(a), the droplet's aperture can be easily scaled up for different applications. Since the generated fringing field is independent of the cell gap, the operating voltage is insensitive to the droplet size. Although the employed ITO electrode gap is relatively wide (20 μm), the droplet still shifts very well. To lower the operating voltage while keeping the desired electric field distribution, we could decrease the electrode gap to 5-10 μm as used in display devices.

In our device, the two liquids have almost the same density and the droplet is firmly anchored to the hole surface at $V=0$. As a result, even if the cell is placed in vertical direction, the droplet shape will not be deformed by the gravity effect. In the actuated state, the droplet experiences both dielectric force and interfacial tensions which assures good mechanical stability against shocks and vibrations. Although our device works very well at 1.55 μm , this device

concept can be extended to mid-wavelength IR [134] and long-wavelength IR [135] by choosing proper liquids in the desired spectral region. Different from a liquid lens [25,28,39], our device no longer depends on the refractive index difference, droplet profile, and shape distortion. Therefore, its electro-optical performances, such as response time, can be easily improved by only considering a few criteria, e.g., viscosity and interfacial tensions. Compared to other fluidic devices, our IR switch can also work in reflective mode if the inner surface of the top glass substrate is coated with a reflector. Therefore, wide spread application of this device concept in various optical communication systems is foreseeable.

4.5 Summary

In this chapter, we have demonstrated a single-pixel display (black/white, red/black, white/blue) based on dielectric effect-induced light channel. Its operating voltage is relatively low and the dynamic response is reasonably fast. Such a new display does not need any polarizer and color filter. Thus, its optical efficiency is high. For the cell with a 130- μm -aperture droplet and 100- μm gap, its contrast ratio is $\sim 10:1$. At $V=45 V_{\text{rms}}$ square-wave bursts, the rise time and decay time is measured as ~ 18 ms and ~ 32 ms, respectively. Contrast ratio can be further improved if a high optical density isotropic liquid is employed. To achieve a wide viewing angle and high optical efficiency, an extra turning film and a microlens array are required in the integration with a conventional edge-lit backlight.

To overcome the problems of a single-pixel display based dielectric effect-induced light channel, we have demonstrated a color (black, red, blue) display based on voltage-stretchable LC droplet. For the cell with an 800- μm -aperture droplet and 420- μm -gap, it has a $\sim 67\%$ aperture

ratio and ~83:1 contrast ratio at $60 V_{\text{rms}}$ (500 Hz). The corresponding travel speeds are estimated to be ~6.1 mm/s and ~3.2 mm/s, respectively. A simple 1×6 color pixel array was also demonstrated. Increasing dye concentration would improve contrast ratio but the transmittance is sacrificed. The operating voltage can be lowered by using interdigitated ITO electrodes with a smaller striped gap. And aperture ratio can be enlarged by a zigzag striped electrode. Surrounding liquid with low viscosity helps to improve the travel speed. To achieve a full color display, we need to adopt green dopant that is dissolvable in the LC droplet but immiscible with the surrounding liquid. Furthermore, using the same structure and the materials without dye clusters, we have demonstrated a variable optical attenuator based on dielectrically stretched LC droplet is demonstrated. The stretched surface of the LC droplet forces the incident beam to deflect and decouple with the output SMF. Such a VOA provides competitive features like simple fabrication, broadband operation over C-Band, low insertion loss (~0.7 dB), large dynamic range (~32 dB), small PDL (~0.3 dB), and low power consumption (~mW). The relatively low operating voltage (~40V_{rms}) and reasonably fast switching time (~20ms) make it promising for various applications.

In an optical switch based on voltage-stretchable LC droplet, largely stretching the surface of a droplet will cause two problems: high operating voltage due to the large stretching, and slow response due to the long distance travel. So we have demonstrated an optical switch based on variable aperture and light transmittance is controlled by changing the aperture size of the pixel. The pixel is confined by a hole-patterned polymer wall and a dielectric liquid (LC) forms a ring shape around the wall surface. At $V=0$, the pixel has the largest aperture. When the voltage is high enough, instead of being stretched in one direction, the LC is stretched radially toward the center of the pixel by the dielectric force, leading to a decrease in the aperture size.

The filled LC occupies ~20% of its chamber space. To ensure the stretched liquid can safely return to its original state with fast response time, the stretched surface should not totally cover its aperture. In our demo, the response time of the pixel is ~10 ms and the aperture ratio is over 80%. For optical switch and display applications, a pixel array is required. The device based on our proposed cell structure has the key features of polarization insensitive, fast response, simple fabrication, and good mechanical stability.

With rapid development in optical communications, IR light switch has become a key component for regulating the optical power in an optical system. We have demonstrated a simple IR light switch with a glycerol droplet actuated by a fringing field. For a 4.5-mm-diameter droplet, the measured contrast ratio is over 95:1 in transmissive mode and recovering time is ~200 ms at 100 V_{rms}. The glycerol droplet is surrounded by density-matching oil, therefore the gravity effect is minimized and the device is mechanically stable against shocks and vibrations. Reflective mode can also be configured by coating a reflective material on the inner surface of the top glass substrate. Our device has advantages in scalable switching area, good optical performance, and good mechanical stability. Potential applications for optical fiber switch, IR shutter, attenuators and filters are foreseeable.

CHAPTER 5 SUMMARY

In this dissertation, we demonstrate optical fluid-based photonic and display devices, and then investigate their working principles as well as electro-optic properties.

In Chapter 2, we demonstrate a membrane-encapsulated liquid lens actuated by a photo-sensitive polymer. This approach paves a way to achieve non-mechanical driving, easy integration with other optical components and compactness. A mechanical-wetting lens is also developed for IR applications. The concept can be extended to middle and long IR if proper liquids are employed.

Dielectric liquid lenses are attractive for their high optical performances and voltage switchable focal lengths. In Chapter 3, we demonstrate a dielectric liquid microlens with well-shaped electrode to fix the microlens position and lower the operating voltage. To widen the dynamic range, we demonstrate an approach to enable focus tuning from negative to positive or vice versa in a single dielectric lens without any moving part. The possibility of fabricating microlens arrays with different aperture and density using a simple method is also proposed. Besides describing device structure and proving concept through experiments, we also study the fundamental electro-optic characteristics of dielectric liquid droplets. Our results will help optimize the lens performances by considering the impact of operating voltage, frequency and droplet size.

Besides dielectric liquid lenses, we also demonstrate several optical switches based on DEP effect in Chapter 4. Examples include optical switch based on voltage-stretchable LC droplet, variable aperture or position-shifting droplet. They work in the visible range or near IR range. Polarizer-free and color filter-free displays based on DEP effect are also discussed.

Simple fabrication, low power consumption, polarization independence, relatively low operating voltage as well as reasonable fast switching time make them promising for various applications.

This work will make an important impact to advancing the state-of-the-art in optical fluid-based photonic and display devices.

APPENDIX: LIST OF PUBLICATIONS

1. H. Ren, **S. Xu**, and S. T. Wu, "Liquid crystal pump," (submitted to Lab Chip, August, 2012).
2. H. Ren, **S. Xu**, Y. Liu, and S. T. Wu, "Liquid-based infrared optical switch," Appl. Phys. Lett. 101, 041104 (2012).
3. **S. Xu**, H. Ren, J. Sun and S. T. Wu, "Polarization independent variable optical attenuator based on dielectrically stretched liquid crystal droplet," Opt. Express **20**, 17059-17064 (2012).
4. H. Ren, **S. Xu**, and S. T. Wu, "Optical switch based on variable aperture," Opt. Lett. 37, 1421-1423 (2012).
5. **S. Xu**, H. Ren, Y. Liu, and S. T. Wu, "Color displays based on voltage-stretchable liquid crystal droplet," J. Display Technol. 8, 336-340 (2012)
6. H. Ren, **S. Xu**, and S. T. Wu, "Voltage-expandable liquid crystal surface," Lab Chip 11, 3426-3430 (2011).
7. Y. Liu, H. Ren, **S. Xu**, Y. Chen, L. Rao, T. Ishinabe, and S. T. Wu, "Adaptive focus integral image system design based on fast-response liquid crystal microlens," J. Display Technol. 7, 674-678 (2011)
8. H. C. Cheng, **S. Xu**, Y. Liu, S. Levi, and S. T. Wu, "Adaptive mechanical-wetting lens actuated by ferrofluids," Opt. Commun. 284, 2118-2121 (2011).
9. H. Ren, **S. Xu**, Y. Liu, and S. T. Wu, "Electro-optical properties of dielectric liquid microlens," Opt. Commun. 284, 2122-2125 (2011).
10. **S. Xu**, H. Ren, Y. Liu, and S. T. Wu, "Dielectric liquid microlens with switchable negative and positive optical power," IEEE J. MEMS 20, 297-301 (2011).
11. H. Ren, **S. Xu**, D. Ren, and S. T. Wu, "Novel optical switch with a reconfigurable dielectric liquid droplet," Opt. Express 19, 1985-1990 (2011).
12. **S. Xu**, Y. Liu, H. Ren, and S. T. Wu, "A novel adaptive mechanical-wetting lens for visible and near infrared imaging," Opt. Express 18, 12430-12435 (2010).
13. H. Ren, **S. Xu**, and S. T. Wu, "Effect of gravity on the shape of liquid droplets," Optics Commun. 283, 3255-3258 (2010).
14. H. Ren, **S. Xu**, and S. T. Wu, "Deformable liquid droplets for optical beam control," Opt. Express 18, 11904-11910 (2010).
15. **S. Xu**, H. Ren, Y. J. Lin, M. G. Jim Moharam, S.T. Wu, and N. Tabiryan, "Adaptive liquid lens actuated by photo-polymer," Opt. Express 17, 17590-17595 (Sept. 28, 2009)

16. **S. Xu**, Y. J. Lin, and S. T. Wu, "Dielectric liquid microlens with well-shaped electrode", *Opt. Express* 17, 10499-10505(2009).
17. H. Ren, **S. Xu**, Y. J. Lin, and S. T. Wu, "Adaptive-focus lenses", *Optics and Photonics News* (October, 2008); pp. 42-47.
18. H. Ren, H. Xianyu, **S. Xu**, and S. T. Wu, "Adaptive dielectric liquid lens", *Opt. Express* 16, 14954-14960 (2008).

LIST OF REFERENCES

1. N. Sugiura and S. Morita, "Variable-Focus Liquid-Filled Optical Lens," *Appl. Opt.* **32**(22), 4181-4186 (1993).
2. K.-H. Jeong, G. Liu, N. Chronis and L. Lee, "Tunable Microdoublet Lens Array," *Opt. Express* **12**(11), 2494-2500 (2004).
3. D.-Y. Zhang, V. Lien, Y. Berdichevsky, J. Choi and Y.-H. Lo, "Fluidic Adaptive Lens with High Focal Length Tunability," *Appl. Phys. Lett.* **82**(19), 3171-3172 (2003).
4. H. Ren and S.-T. Wu, "Variable-Focus Liquid Lens," *Opt. Express* **15**(10), 5931-5936 (2007).
5. D.-Y. Zhang, N. Justis and Y.-H. Lo, "Integrated Fluidic Adaptive Zoom Lens," *Opt. Lett.* **29**(24), 2855-2857 (2004).
6. D.-Y. Zhang, N. Justis and Y.-H. Lo, "Fluidic Adaptive Lens of Transformable Lens Type," *Appl. Phys. Lett.* **84**(21), 4194-4196 (2004).
7. Z. De-Ying, N. Justis and L. Yu-Hwa, "Integrated Fluidic Lenses and Optic Systems," *IEEE J. Sel. Top. Quantum Electron.* **11**(1), 97-106 (2005).
8. S. Xu, Y. Liu, H. Ren and S.-T. Wu, "A Novel Adaptive Mechanical-Wetting Lens for Visible and near Infrared Imaging," *Opt. Express* **18**(12), 12430-12435 (2010).
9. Y. Hongbin, Z. Guangya, C.F. Siong and L. Feiwen, "Optofluidic Variable Aperture," *Opt. Lett.* **33**(6), 548-550 (2008).
10. H. Yu, G. Zhou, S. Chau Fook and F. Lee, "A Variable Optical Attenuator Based on Optofluidic Technology," *J. Micromech. Microeng.* **18**(11), 115016 (2008).
11. C.A. Lopez, C.-C. Lee and A.H. Hirs, "Electrochemically Activated Adaptive Liquid Lens," *Appl. Phys. Lett.* **87**(13), 134102-134103 (2005).
12. L. Miccio, A. Finizio, S. Grilli, V. Vespini, M. Paturzo, S. De Nicola and P. Ferraro, "Tunable Liquid Microlens Arrays in Electrode-Less Configuration and Their Accurate Characterization by Interference Microscopy," *Opt. Express* **17**(4), 2487-2499 (2009).
13. S. Grilli, L. Miccio, V. Vespini, A. Finizio, S. De Nicola and P. Ferraro, "Liquid Micro-Lens Array Activated by Selective Electrowetting on Lithium Niobate Substrates," *Opt. Express* **16**(11), 8084-8093 (2008).
14. L. Dong, A.K. Agarwal, D.J. Beebe and H. Jiang, "Adaptive Liquid Microlenses Activated by Stimuli-Responsive Hydrogels," *Nature* **442**(7102), 551-554 (2006).

15. X. Zeng and H. Jiang, "Tunable Liquid Microlens Actuated by Infrared Light-Responsive Hydrogel," *Appl. Phys. Lett.* **93**(15), 151101-151103 (2008).
16. D. Zhu, C. Li, X. Zeng and H. Jiang, "Tunable-Focus Microlens Arrays on Curved Surfaces," *Appl. Phys. Lett.* **96**(8), 081111-081113 (2010).
17. J.L. Jackel, S. Hackwood and G. Beni, "Electrowetting Optical Switch," *Appl. Phys. Lett.* **40**(1), 4-5 (1982).
18. M. Vallet, B. Berge and L. Vovelle, "Electrowetting of Water and Aqueous Solutions on Poly(Ethylene Terephthalate) Insulating Films," *Polym.* **37**(12), 2465-2470 (1996).
19. R.A. Hayes and B.J. Feenstra, "Video-Speed Electronic Paper Based on Electrowetting," *Nature* **425**(6956), 383-385 (2003).
20. M. Frieder and B. Jean-Christophe, "Electrowetting: From Basics to Applications," *J. Phys. Condens. Matter* **17**(28), R705 (2005).
21. N.R. Smith, D.C. Abeysinghe, J.W. Haus and J. Heikenfeld, "Agile Wide-Angle Beam Steering with Electrowetting Microprisms," *Opt. Express* **14**(14), 6557-6563 (2006).
22. C.U. Murade, J.M. Oh, D. van den Ende and F. Mugele, "Electrowetting Driven Optical Switch and Tunable Aperture," *Opt. Express* **19**(16), 15525-15531 (2011).
23. L. Li, C. Liu, H.-R. Peng and Q.-H. Wang, "Optical Switch Based on Electrowetting Liquid Lens," *J. Appl. Phys.* **111**(10), 103103-103104 (2012).
24. HeikenfeldJ, ZhouK, KreitE, RajB, YangS, SunB, MilarcikA, ClappL and SchwartzR, "Electrofluidic Displays Using Young-Laplace Transposition of Brilliant Pigment Dispersions," *Nat. Photon.* **3**(5), 292-296 (2009).
25. C.-C. Cheng, C.A. Chang and J.A. Yeh, "Variable Focus Dielectric Liquid Droplet Lens," *Opt. Express* **14**(9), 4101-4106 (2006).
26. C.-C. Cheng and J.A. Yeh, "Dielectrically Actuated Liquid Lens," *Opt. Express* **15**(12), 7140-7145 (2007).
27. H. Ren and S.-T. Wu, "Tunable-Focus Liquid Microlens Array Using Dielectrophoretic Effect," *Opt. Express* **16**(4), 2646-2652 (2008).
28. H. Ren, H. Xianyu, S. Xu and S.-T. Wu, "Adaptive Dielectric Liquid Lens," *Opt. Express* **16**(19), 14954-14960 (2008).
29. Y.-J. Lin, K.-M. Chen and S.-T. Wu, "Broadband and Polarization-Independent Beam Steering Using Dielectrophoresis-Tilted Prism," *Opt. Express* **17**(10), 8651-8656 (2009).

30. H. Ren, S.H. Lee and S.T. Wu, "Reconfigurable Liquid Crystal Droplets Using a Dielectric Force," *Appl. Phys. Lett.* **95**(24), 241108-241103 (2009).
31. C.G. Tsai, C. Chi-Nan, C. Li-Shun, C. Chih-Cheng, Y. Jing-Tang and J.A. Yeh, "Planar Liquid Confinement for Optical Centering of Dielectric Liquid Lenses," *IEEE Photonics Technol. Lett.* **21**(19), 1396-1398 (2009).
32. S. Xu, Y.-J. Lin and S.-T. Wu, "Dielectric Liquid Microlens with Well-Shaped Electrode," *Opt. Express* **17**(13), 10499-10505 (2009).
33. C.G. Tsai and J.A. Yeh, "Circular Dielectric Liquid Iris," *Opt. Lett.* **35**(14), 2484-2486 (2010).
34. H. Ren, S. Xu, D. Ren and S.-T. Wu, "Novel Optical Switch with a Reconfigurable Dielectric Liquid Droplet," *Opt. Express* **19**(3), 1985-1990 (2011).
35. H. Ren, S. Xu and S.-T. Wu, "Voltage-Expandable Liquid Crystal Surface," *Lab Chip.* **11**(20), 3426-3430 (2011).
36. X. Su, R. Hongwen, L. Yifan and W. Shin-Tson, "Dielectric Liquid Microlens with Switchable Negative and Positive Optical Power," *J. Microelectromech. Syst.* **20**(1), 297-301 (2011).
37. S. Xu, H. Ren, Y. Liu and S.-T. Wu, "71.2: Color Displays Using Reconfigurable Liquid Droplets," *SID Symposium Digest of Technical Papers* **42**(1), 1046-1048 (2011).
38. S. Xu, H. Ren, Y. Liu and S.T. Wu, "Color Displays Based on Voltage-Stretchable Liquid Crystal Droplet," *J. Disp. Technol.* **8**(6), 336-340 (2012).
39. S. Kuiper and B.H.W. Hendriks, "Variable-Focus Liquid Lens for Miniature Cameras," *Appl. Phys. Lett.* **85**(7), 1128-1130 (2004).
40. S. Murali, K.P. Thompson and J.P. Rolland, "Three-Dimensional Adaptive Microscopy Using Embedded Liquid Lens," *Opt. Lett.* **34**(2), 145-147 (2009).
41. S.A. Reza and N.A. Riza, "A Liquid Lens-Based Broadband Variable Fiber Optical Attenuator," *Opt. Commun.* **282**(7), 1298-1303 (2009).
42. F.S. Tsai, D. Johnson, C.S. Francis, S.H. Cho, W. Qiao, A. Arianpour, Y. Mintz, S. Horgan, M. Talamini and Y.-H. Lo, "Fluidic Lens Laparoscopic Zoom Camera for Minimally Invasive Surgery," *J. Biomed. Opt.* **15**(3), 030504-030503 (2010).
43. Q. Wen, F.S. Tsai, C. Sung Hwan, Y. Huimin and L. Yu-Hwa, "Fluidic Intraocular Lens with a Large Accommodation Range," *IEEE Photonics Technol. Lett.* **21**(5), 304-306 (2009).
44. W. Qiao, D. Johnson, F.S. Tsai, S.H. Cho and Y.-H. Lo, "Bio-Inspired Accommodating Fluidic Intraocular Lens," *Opt. Lett.* **34**(20), 3214-3216 (2009).

45. C. Bricot, M. Hareng and E. Spitz, U.S. patent, **1977**; Vol. 4,037,929.
46. S. Sato, "Liquid-Crystal Lens-Cells with Variable Focal Length," *Jpn. J. Appl. Phys.* **18**(9), 1679-1684 (1979).
47. A. Naumov, G. Love, M.Y. Loktev and F. Vladimirov, "Control Optimization of Spherical Modal Liquid Crystal Lenses," *Opt. Express* **4**(9), 344-352 (1999).
48. T. Nose and S. Sato, "A Liquid Crystal Microlens Obtained with a Non-Uniform Electric Field," *Liq. Cryst.* **5**(5), 1425-1433 (1989).
49. H. Ren, Y.-H. Fan and S.-T. Wu, "Tunable Fresnel Lens Using Nanoscale Polymer-Dispersed Liquid Crystals," *Appl. Phys. Lett.* **83**(8), 1515-1517 (2003).
50. H. Ren, Y.-H. Fan, S. Gauza and S.-T. Wu, "Tunable-Focus Flat Liquid Crystal Spherical Lens," *Appl. Phys. Lett.* **84**(23), 4789-4791 (2004).
51. H. Ren, D. Fox, P.A. Anderson, B. Wu and S.-T. Wu, "Tunable-Focus Liquid Lens Controlled Using a Servo Motor," *Opt. Express* **14**(18), 8031-8036 (2006).
52. H. Ren and S.-T. Wu, "Adaptive Liquid Crystal Lens with Large Focal Length Tunability," *Opt. Express* **14**(23), 11292-11298 (2006).
53. H. Ren, D.W. Fox, B. Wu and S.-T. Wu, "Liquid Crystal Lens with Large Focal Length Tunability and Low Operating Voltage," *Opt. Express* **15**(18), 11328-11335 (2007).
54. H. Oku and M. Ishikawa, "High-Speed Liquid Lens with 2 Ms Response and 80.3 Nm Root-Mean-Square Wavefront Error," *Appl. Phys. Lett.* **94**(22), 221108-221103 (2009).
55. H.-M. Son, M.Y. Kim and Y.-J. Lee, "Tunable-Focus Liquid Lens System Controlled by Antagonistic Winding-Type Sma Actuator," *Opt. Express* **17**(16), 14339-14350 (2009).
56. S. Xu, H. Ren, Y.-J. Lin, M.G.J. Moharam, S.-T. Wu and N. Tabiryan, "Adaptive Liquid Lens Actuated by Photo-Polymer," *Opt. Express* **17**(20), 17590-17595 (2009).
57. S.S. Sudheer, D. Liang and J. Hongrui, "A Microfluidic Chemical/Biological Sensing System Based on Membrane Dissolution and Optical Absorption," *Meas. Sci. Technol.* **18**(1), 201 (2007).
58. S. Gauza, H. Wang, C.-H. Wen, S.-T. Wu, A.J. Seed and R. Dabrowski, "High Birefringence Isothiocyanato Tolane Liquid Crystals," *Jpn. J. Appl. Phys.* **42**(Part 1, No. 6A), 3463-3466 (2003).
59. S. Gauza, C.-H. Wen, S.-T. Wu, N. Janarthanan and C.-S. Hsu, "Super High Birefringence Isothiocyanato Biphenyl-Bistolane Liquid Crystals," *Jpn. J. Appl. Phys.* **43**(11A), 7634-7638 (2004).

60. M. Yamada, N. Nada, M. Saitoh and K. Watanabe, "First-Order Quasi-Phase Matched Linbo[Sub 3] Waveguide Periodically Poled by Applying an External Field for Efficient Blue Second-Harmonic Generation," *Appl. Phys. Lett.* **62**(5), 435-436 (1993).
61. S. Grilli, M. Paturzo, L. Miccio and P. Ferraro, "In Situ Investigation of Periodic Poling in Congruent Linbo 3 by Quantitative Interference Microscopy," *Meas. Sci. Technol.* **19**(7), 074008 (2008).
62. B. Rosenblum, P. Braunlich and J.P. Carrico, "Thermally Stimulated Field Emission from Pyroelectric Linbo[Sub 3]," *Appl. Phys. Lett.* **25**(1), 17-19 (1974).
63. C.H. Bulmer, W.K. Burns and S.C. Hiser, "Pyroelectric Effects in Linbo[Sub 3] Channel-Waveguide Devices," *Appl. Phys. Lett.* **48**(16), 1036-1038 (1986).
64. G. Lippmann, "Relation Entre Les Phénomènes Électriques Et Capillaires," *Ann. Chim. Phys.* **5**, 494-549 (1875).
65. A. Froumkine, "Couche Double. Electrocapillarité Surtension," *Actualités Scientifiques* **373**, 5-36 (1936).
66. H.J.J. Verheijen and M.W.J. Prins, "Reversible Electrowetting and Trapping of Charge: Model and Experiments," *Langmuir* **15**(20), 6616-6620 (1999).
67. E. Seyrat and R.A. Hayes, "Amorphous Fluoropolymers as Insulators for Reversible Low-Voltage Electrowetting," *J. Appl. Phys.* **90**(3), 1383-1386 (2001).
68. H.A. Pohl, "*Dielectrophoresis*", (Cambridge University Press, Cambridge, 1978).
69. T.B. Jones, "*Electromechanics of Particles*", (Cambridge University Press, Cambridge, 1995).
70. H.A. Haus and J.R. Melcher, "*Electromagnetic Fields and Energy*", Chap. 11, Prentice-Hall, Englewood Cliffs, NJ, 1989).
71. A.P. Weber, M. Seipenbusch and G. Kasper, "Size Effects in the Catalytic Activity of Unsupported Metallic Nanoparticles," *J. Nanopart. Res.* **5**(3), 293-298 (2003).
72. J. Regtmeier, T.T. Duong, R. Eichhorn, D. Anselmetti and A. Ros, "Dielectrophoretic Manipulation of DNA: Separation and Polarizability," *Anal. Chem.* **79**(10), 3925-3932 (2007).
73. P.A. Smith, C.D. Nordquist, T.N. Jackson, T.S. Mayer, B.R. Martin, J. Mbindyo and T.E. Mallouk, "Electric-Field Assisted Assembly and Alignment of Metallic Nanowires," *Appl. Phys. Lett.* **77**(9), 1399-1401 (2000).

74. C.K.M. Fung, V.T.S. Wong, R.H.M. Chan and W.J. Li, "Dielectrophoretic Batch Fabrication of Bundled Carbon Nanotube Thermal Sensors," *IEEE Transactions on Nanotechnology* **3**(3), 395-403 (2004).
75. J. Zeng and T. Korsmeyer, "Principles of Droplet Electrohydrodynamics for Lab-on-a-Chip," *Lab Chip*. **4**(4), 265-277 (2004).
76. D.J. Laser and J.G. Santiago, "A Review of Micropumps," *J. Micromech. Microeng.* **14**(6), R35 (2004).
77. R. Hagedorn, G. Fuhr, T. Müller, T. Schnelle, U. Schnakenberg and B. Wagner, "Design of Asynchronous Dielectric Micromotors," *J. Electrostat.* **33**(2), 159-185 (1994).
78. H. Ren and S.-T. Wu, "Optical Switch Using a Deformable Liquid Droplet," *Opt. Lett.* **35**(22), 3826-3828 (2010).
79. H. Ren, S. Xu and S.-T. Wu, "Deformable Liquid Droplets for Optical Beam Control," *Opt. Express* **18**(11), 11904-11910 (2010).
80. S.W. Lee and S.S. Lee, "Focal Tunable Liquid Lens Integrated with an Electromagnetic Actuator," *Appl. Phys. Lett.* **90**(12), 121129-121123 (2007).
81. F. Schneider, C. Müller and U. Wallrabe, "A Low Cost Adaptive Silicone Membrane Lens," *J. Opt. A: Pure Appl. Opt.* **10**(4), 044002 (2008).
82. E. Masayoshi, "Micro/Nano Electro Mechanical Systems for Practical Applications," *J. Phys. Conf. Ser.* **187**(1), 012001 (2009).
83. C.-S. Liu and P.D. Lin, "Miniaturized Auto-Focusing Vcm Actuator with Zero Holding Current," *Opt. Express* **17**(12), 9754-9763 (2009).
84. C.-S. Liu and P.D. Lin, "A Miniaturized Low-Power Vcm Actuator for Auto-Focusing Applications," *Opt. Express* **16**(4), 2533-2540 (2008).
85. D.J. Beebe, J.S. Moore, J.M. Bauer, Q. Yu, R.H. Liu, C. Devadoss and B.-H. Jo, "Functional Hydrogel Structures for Autonomous Flow Control inside Microfluidic Channels," *Nature* **404**(6778), 588-590 (2000).
86. H. Finkelmann, E. Nishikawa, G.G. Pereira and M. Warner, "A New Opto-Mechanical Effect in Solids," *Phy. Rev. Lett.* **87**(1), 015501 (2001).
87. Y. Yu, M. Nakano and T. Ikeda, "Photomechanics: Directed Bending of a Polymer Film by Light," *Nature* **425**(6954), 145-145 (2003).
88. S.V. Serak, N.V. Tabiryan, T.J. White and T.J. Bunning, "Azobenzene Liquid Crystal Polymer-Based Membrane and Cantilever Optical Systems," *Opt. Express* **17**(18), 15736-15746 (2009).

89. N. Tabiryan, S. Serak, X.-M. Dai and T. Bunning, "Polymer Film with Optically Controlled Form and Actuation," *Opt. Express* **13**(19), 7442-7448 (2005).
90. M. Schadt and W. Helfrich, "Voltage-Dependent Optical Activity of a Twisted Nematic Liquid Crystal," *Appl. Phys. Lett.* **18**(4), 127-128 (1971).
91. M. Liu and Q. Chen, "Characterization Study of Bonded and Unbonded Polydimethylsiloxane Aimed for Bio-Micro-Electromechanical Systems-Related Applications," *J. Micro/Nanolithogr. MEMS MOEMS* **6**(2), 023008-023006 (2007).
92. S.-T. Wu and D.-K. Yang, "*Reflective Liquid Crystal Displays*", (Wiley, New York, 2011).
93. T.-K. Shih, C.-F. Chen, J.-R. Ho and F.-T. Chuang, "Fabrication of Pdms (Polydimethylsiloxane) Microlens and Diffuser Using Replica Molding," *Microelectron. Eng.* **83**(11-12), 2499-2503 (2006).
94. S.-T. Wu, "Absorption Measurements of Liquid Crystals in the Ultraviolet, Visible, and Infrared," *J. Appl. Phys.* **84**(8), 4462-4465 (1998).
95. C.G. Schroer, M. Kuhlmann, U.T. Hunger, T.F. Gunzler, O. Kurapova, S. Feste, F. Frehse, B. Lengeler, M. Drakopoulos, A. Somogyi *et al.*, "Nanofocusing Parabolic Refractive X-Ray Lenses," *Appl. Phys. Lett.* **82**(9), 1485-1487 (2003).
96. H.-C. Cheng, S. Xu, Y. Liu, S. Levi and S.-T. Wu, "Adaptive Mechanical-Wetting Lens Actuated by Ferrofluids," *Opt. Commun.* **284**(8), 2118-2121 (2011).
97. B. Javidi, J.-S. Jang, A. Stern and S. Kishk, Three Dimensional Image Sensing, Visualization and Processing Using Integral Imaging, *Frontiers in Optics* **2004**, pFTuO2.
98. G.C. Knollman, J.L.S. Bellin, J. Weaver and J.J. Hartog, "Variable-Focus Liquid-Filled Hydroacoustic Lens," *J. Acoust. Soc. Am.* **49**(1A), 91-91 (1971).
99. P. Ruffieux, T. Scharf, H.P. Herzig, R. Völkel and K.J. Weible, "On the Chromatic Aberration of Microlenses," *Opt. Express* **14**(11), 4687-4694 (2006).
100. Y.-H. Lin, J.-K. Li, T.-Y. Chu and H.-K. Hsu, "A Bistable Polarizer-Free Electro-Optical Switch Using a Droplet Manipulation on a Liquid Crystal and Polymer Composite Film," *Opt. Express* **18**(10), 10104-10111 (2010).
101. P. Penfield and H.A. Haus, "*Electrodynamics of Moving Media*", (Cambridge, MIT, 1967).
102. E. Higuchi and Y. Koike, U.S. Patent **2001**.
103. C. Karuwan, K. Sukthang, A. Wisitsoraat, D. Phokharatkul, V. Patthanasettakul, W. Wechsato and A. Tuantranont, "Electrochemical Detection on Electrowetting-on-Dielectric Digital Microfluidic Chip," *Talanta* **84**(5), 1384-1389 (2011).

104. G.G. Hougham, P.E. Cassidy, K. Johns and T. Davidson, "*Fluoropolymers 2: Properties*", (Plenum Press, New York, 1999).
105. Y. Chih-Cheng, C.W.G. Tsai and J.A. Yeh, "Dynamic Behavior of Liquid Microlenses Actuated Using Dielectric Force," *J. Microelectromech. Syst.* **20**(5), 1143-1149 (2011).
106. S. Yang, K. Zhou, E. Kreit and J. Heikenfeld, "High Reflectivity Electrofluidic Pixels with Zero-Power Grayscale Operation," *Appl. Phys. Lett.* **97**(14), 143501-143503 (2010).
107. R.W. Sabnis, "Color Filter Technology for Liquid Crystal Displays," *Displays* **20**(3), 119-129 (1999).
108. Y.-H. Lin, J.-M. Yang, Y.-R. Lin, S.-C. Jeng and C.-C. Liao, "A Polarizer-Free Flexible and Reflective Electrooptical Switch Using Dye-Doped Liquid Crystal Gels," *Opt. Express* **16**(3), 1777-1785 (2008).
109. S. Agastin, M.R. King and T.B. Jones, "Rapid Enrichment of Biomolecules Using Simultaneous Liquid and Particulate Dielectrophoresis," *Lab Chip.* **9**(16), 2319-2325 (2009).
110. T.B. Jones, M. Gunji, M. Washizu and M.J. Feldman, "Dielectrophoretic Liquid Actuation and Nanodroplet Formation," *J. Appl. Phys.* **89**(2), 1441-1448 (2001).
111. H. Schenk, P. Dür, D. Kunze, H. Lakner and H. Kück, "A Resonantly Excited 2d-Micro-Scanning-Mirror with Large Deflection," *Sens. Actuators A* **89**(1-2), 104-111 (2001).
112. S.H. Hung, H.-T. Hsieh and G.-D.J. Su, "An Electro-Magnetic Micromachined Actuator Monolithically Integrated with a Vertical Shutter for Variable Optical Attenuation," *J. Micromech. Microeng.* **18**(7), 075003 (2008).
113. L. Zhu, Y. Huang and A. Yariv, "Integrated Microfluidic Variable Optical Attenuator," *Opt. Express* **13**(24), 9916-9921 (2005).
114. M.I. Lapsley, S.-C.S. Lin, X. Mao and T.J. Huang, "An in-Plane, Variable Optical Attenuator Using a Fluid-Based Tunable Reflective Interface," *Appl. Phys. Lett.* **95**(8), 083507-083503 (2009).
115. R.A. Soref and D.H. McMahon, "Total Switching of Unpolarized Fiber Light with a Four-Port Electro-Optic Liquid-Crystal Device," *Opt. Lett.* **5**(4), 147-149 (1980).
116. E.G. Hanson, "Polarization-Independent Liquid-Crystal Optical Attenuator for Fiber-Optics Applications," *Appl. Opt.* **21**(7), 1342-1344 (1982).
117. N.A. Riza and S.A. Khan, "Liquid-Crystal-Deflector Based Variable Fiber-Optic Attenuator," *Appl. Opt.* **43**(17), 3449-3455 (2004).

118. F. Du, Y.-q. Lu, H. Ren, S. Gauza and S.-T. Wu, "Polymer-Stabilized Cholesteric Liquid Crystal for Polarization-Independent Variable Optical Attenuator," *Jpn. J. Appl. Phys.* **43**(10), 7083-7086 (2004).
119. Y.-q. Lu, F. Du, Y.-H. Lin and S.-T. Wu, "Variable Optical Attenuator Based on Polymer Stabilized Twisted Nematic Liquid Crystal," *Opt. Express* **12**(7), 1221-1227 (2004).
120. Y.-H. Wu, Y.-H. Lin, Y.-Q. Lu, H. Ren, Y.-H. Fan, J. Wu and S.-T. Wu, "Submillisecond Response Variable Optical Attenuator Based on Sheared Polymer Network Liquid Crystal," *Opt. Express* **12**(25), 6382-6389 (2004).
121. K. Takizawa, K. Kodama and K. Kishi, "Polarization-Independent Optical Fiber Modulator by Use of Polymer-Dispersed Liquid Crystals," *Appl. Opt.* **37**(15), 3181-3189 (1998).
122. K.M. Chen, H. Ren and S.T. Wu, "Pdlc-Based Voa with a Small Polarization Dependent Loss," *Opt. Commun.* **282**(22), 4374-4377 (2009).
123. M. van Buren and N.A. Riza, "Foundations for Low-Loss Fiber Gradient-Index Lens Pair Coupling with the Self-Imaging Mechanism," *Appl. Opt.* **42**(3), 550-565 (2003).
124. S.-T. Wu and D.-K. Yang, "*Fundamentals of Liquid Crystal Devices*", (Wiley, 2006).
125. P.S. Drzaic, "Polymer Dispersed Nematic Liquid Crystal for Large Area Displays and Light Valves," *J. Appl. Phys.* **60**(6), 2142-2148 (1986).
126. D.K. Yang, L.C. Chien and J.W. Doane, "Cholesteric Liquid Crystal/Polymer Dispersion for Haze-Free Light Shutters," *Appl. Phys. Lett.* **60**(25), 3102-3104 (1992).
127. H. Ren, H. Xianyu and S.-T. Wu, "Liquid Crystal Droplet Array for Non-Contact Electro-Optic Inspections," *J. Phys. D: Appl. Phys.* **43**(36), 365103 (2010).
128. K. Campbell, A. Groisman, U. Levy, L. Pang, S. Mookherjea, D. Psaltis and Y. Fainman, "A Microfluidic 2 X 2 Optical Switch," *Appl. Phys. Lett.* **85**(25), 6119-6121 (2004).
129. Y. Zuta, I. Goykhman, B. Desiatov and U. Levy, "On-Chip Switching of a Silicon Nitride Micro-Ring Resonator Based on Digital Microfluidics Platform," *Opt. Express* **18**(24), 24762-24769 (2010).
130. S.T. Wu, "Infrared Properties of Nematic Liquid-Crystals - an Overview," *Opt. Eng.* **26**(2), 120-128 (1987).
131. S. Diahm, S. Zelmat, M.L. Locatelli, S. Dinculescu, M. Decup and T. Lebey, "Dielectric Breakdown of Polyimide Films: Area, Thickness and Temperature Dependence," *IEEE Transactions on Dielectrics and Electrical Insulation* **17**(1), 18-27 (2010).

132. R. Jensen, J. Cummings and H. Vora, "Copper/Polyimide Materials System for High Performance Packaging," *IEEE Transactions on Components, Hybrids, and Manufacturing Technology* **7**(4), 384-393 (1984).
133. H. Deligöz, T. Yalcinyuva, S. Özgümüş and S. Yildirim, "Electrical Properties of Conventional Polyimide Films: Effects of Chemical Structure and Water Uptake," *J. Appl. Polym. Sci.* **100**(1), 810-818 (2006).
134. Y. Chen, H. Xianyu, J. Sun, P. Kula, R. Dabrowski, S. Tripathi, R.J. Twieg and S.-T. Wu, "Low Absorption Liquid Crystals for Mid-Wave Infrared Applications," *Opt. Express* **19**(11), 10843-10848 (2011).
135. S.-T. Wu, J.D. Margerum, H.B. Meng, C.S. Hsu and L.R. Dalton, "Potential Liquid Crystal Mixtures for Co[Sub 2] Laser Application," *Appl. Phys. Lett.* **64**(10), 1204-1206 (1994).